

Thesis presented to the Faculty of the Department of Graduate Studies of the Technological Institute of Aeronautics, in partial fulfillment of the requirements for the Degree of Doctor in Science in the Program of Aeronautics and Mechanical Engineering, Area of Aerospace Systems and Mechatronics.

Priscilla Andressa de Sousa Silva

**THE ALGORITHMIC WEAK STABILITY BOUNDARY IN
EARTH-TO-MOON MISSION DESIGN: DYNAMICAL
ASPECTS AND APPLICABILITY**

Thesis approved in its final version by the signatories below



Prof. Dr. Maisa de Oliveira Terra
Advisor

Prof. Dr. Celso Massaki Hirata
Head of the Faculty of the Department of Graduate Studies

Campo Montenegro
São José dos Campos, SP – Brazil
2011

Cataloging-in-Publication Data
Documentation and Information Division

de Sousa Silva, Priscilla Andressa

The Algorithmic Weak Stability Boundary in Earth-to-Moon Mission Design: Dynamical Aspects and Applicability / Priscilla Andressa de Sousa Silva.

São José dos Campos, 2011.

183f.

Thesis of Doctor in Science – Program of Aeronautics and Mechanical Engineering. Area of Aerospace Systems and Mechatronics – Technological Institute of Aeronautics, 2011.

Advisor: Prof. Dr. Maisa de Oliveira Terra

1. Astronautics 2. Weak Stability Boundaries. 3. Hamiltonian Dynamics. I. Technological Institute of Aeronautics. II. Title

BIBLIOGRAPHIC REFERENCE

de Sousa Silva, Priscilla A. **The Algorithmic Weak Stability Boundary in Earth-to-Moon Mission Design: Dynamical Aspects and Applicability.** 2011. 183f. Thesis of Doctor in Science – Technological Institute of Aeronautics, São José dos Campos.

CESSION OF RIGHTS

AUTHOR NAME: Priscilla Andressa de Sousa Silva

PUBLICATION TITLE: The Algorithmic Weak Stability Boundary in Earth-to-Moon Mission Design: Dynamical Aspects and Applicability

PUBLICATION KIND/YEAR: Thesis / 2011

It is granted to Technological Institute of Aeronautics permission to reproduce copies of this thesis to only loan or sell copies for academic and scientific purposes. The author reserves other publication rights and no part of this thesis can be reproduced without the authorization of the author.

Priscilla Andressa de Sousa Silva
Av. São João 279, Ap. 11
CEP 12.242-840, São José dos Campos – SP

**THE ALGORITHMIC WEAK STABILITY BOUNDARY IN
EARTH-TO-MOON MISSION DESIGN: DYNAMICAL
ASPECTS AND APPLICABILITY**

Priscilla Andressa de Sousa Silva

Thesis Committee Composition:

Prof. Dr. Sandro da Silva Fernandes	Chairperson	– ITA
Prof. Dr. Maisa de Oliveira Terra	Advisor	– ITA
Prof. Dr. Sylvio Ferraz Mello		– IAG - USP
Prof. Dr. Rodolpho Vilhena Moraes		– UNIFESP - São José dos Campos
Prof. Dr. Erico Luiz Rempel		– ITA

ITA

*To God,
who deserves all the glory.*

*To Papi and Mami,
my safe harbor.*

*A Deus,
merecedor de toda glória.*

*A Papi e Mami,
meu porto seguro.*

Acknowledgements

Agradecimentos

A Deus, que dá o folego de vida e tudo sustenta, que fortalece o cansado e acolhe aqueles que o buscam, por fazer tudo perfeito ao seu tempo.

A Papi e Mami, Severino e Eliene, pelo amor incondicional, apoio constante e exemplo de vida. Eu não teria chegado até aqui sem seus cuidados, seus ensinamentos, sua força e suas orações.

A Talita (ou Ta, ou Little), irmã e amiga, pela presença constante. A Nena, pelo carinho e dedicação.

A vovô Gilvan (*in memorian*) e vovó Nicinha, por me mostrarem o valor de uma vida simples e honrada.

À Prof. Maisa, minha orientadora, pela amizade, pela convivência enriquecedora, por investir na minha formação, e por seu empenho sem medida. Que Deus permita que trabalhemos juntas por muito tempo.

Ao Prof. Sandro Fernandes, ao Dr. Cleverson Marinho, à Profa. Teresinha Stuchi, ao Prof. Rodolpho Vilhena e ao Prof. Bertachini Prado, pelas discussões valiosas e contribuições efetivas para o desenvolvimento desta tese.

Ao Prof. Erico Rempel e ao Prof. Abraham Chian, por contribuirem com a minha formação acadêmica.

Aos professores e funcionários do ITA, em especial do Departamento de Matemática por propiciarem um ambiente de trabalho agradável e produtivo.

Aos colegas da Pós-graduação pelo companheirismo ao longo destes quatro anos, especialmente aos que dividiram sala comigo, Sheila, Chico, Rodrigo, Pablo e Moura e às meninas da Química, Renata e Luciana.

Às minhas grandes amigas, sempre presentes apesar da distância física, por compartilharem comigo as alegrias e tristezas desta vida, Priscilla Doida, Natalia, Gilvânia, Nalvinha e Nalvinha. Que os anos fortaleçam cada vez mais o sentimento de amizade que me une a cada uma de vocês.

A Juliana e Michelle, pela alegria de descobrir novas amigas.

Aos irmãos e irmãs em Cristo, pelas orações contínuas. Vocês também são participantes das minhas vitórias.

*We have to feel the universe at once as an ogre's
castle, to be stormed, and yet as our own cottage,
to which we can return at evening.*

*Precisamos sentir o universo ao mesmo tempo
como o castelo de um ogro, que deve ser tomado
de assalto, e, no entanto, como a nossa própria
casinha, para a qual voltamos ao anoitecer.*

G. K. CHESTERTON

Abstract

This thesis consists of an extensive study of the Weak Stability Boundary (WSB) concept in low-energy Earth-to-Moon mission design within the mathematical structure provided by the Planar Circular Restricted Three-Body Problem (PCR3BP). By employing the *patched three-body approach* to approximate the Sun-Earth-Moon-spacecraft system, we examine and characterize the construction of Earth-to-Moon transfer orbits. Then, we focus on the final portion of the transfer trajectories, investigating the WSB algorithmic definition proposed by E. Belbruno. We perform a dynamical characterization of the WSB associated sets generated in the lunar sphere of influence by two implementations of this algorithmic definition, namely, considering the Moon as a punctual mass and as a body with finite radius. In addition, the associated sets are analysed according to relevant criteria established on three-body problem elements in order to clarify their possible applicability in external and internal transfers and to verify the consistency of the algorithmic construction procedure. Finally, we extract the boundary of stability and investigate the structure of the boundary set by characterizing specific stable-unstable transitions. This study identifies various vulnerable aspects of the algorithmic definition concerning the adequate detection of stability regions for ballistic lunar capture, and indicates required corrections to the algorithmic construction.

Resumo

Esta tese consiste em um estudo extensivo do conceito de Fronteira de Estabilidade Fraca (WSB, do inglês *Weak Stability Boundary*) em projetos de missões espaciais Terra-Lua de baixa energia no contexto do formalismo matemático definido pelo Problema Restrito de Três Corpos Circular Planar. Empregando a abordagem *patched three-body* (dois problemas de três corpos conjugados) para aproximar o sistema Sol-Terra-Lua-espaçonave, examinamos e caracterizamos a construção de órbitas de transferência Terra-Lua. Então, focamos na porção final das trajetórias de transferência, investigando a definição algorítmica da WSB proposta por E. Belbruno. Realizamos uma caracterização dinâmica dos conjuntos associados à WSB algorítmica gerados na esfera de influência lunar por duas implementações dessa definição, uma delas considerando a Lua como uma massa puntual e a outra levando em conta o seu raio físico finito. Além disso, com o objetivo de compreender a possível aplicabilidade dos conjuntos associados em transferências internas e externas e verificar a consistência do procedimento construtivo, esses conjuntos foram analisados através de critérios relevantes estabelecidos com base em elementos do problema de três corpos. Finalmente, a fronteira de estabilidade foi extraída e a estrutura desse conjunto foi investigada através da caracterização de transições estáveis-instáveis específicas. Este estudo identifica vários aspectos vulneráveis da definição algorítmica referentes à detecção adequada de regiões de estabilidade associadas à captura balística pela Lua e indica correções requeridas pela construção algorítmica.

List of Figures

2.1	Sidereal and synodic coordinate frames.	24
2.2	Equilibrium points of the PCR3BP.	30
2.3	C_k , $k = 1,2,3,4,5$, as a function of μ	35
2.4	Four possible Hill Region cases	36
2.5	Lyapunov orbits and their stable and unstable manifolds.	42
2.6	\mathcal{R} region around a collinear equilibrium point.	47
3.1	Schematic representation of the stability classification.	55
4.1	EM portion of a complete transfer orbit.	64
4.2	Poincaré cuts of the manifolds W_{\odot}^u and W_{\oplus}^s	66
4.3	Sensitive dependence on initial conditions around the Earth.	68
4.4	Projection onto the X - Y plane of a complete transfer orbit.	69
4.5	Initial conditions inside the inner branch of W_{\oplus}^u	70
4.6	Σ_c Poincaré cuts of trajectories inside W_{\oplus}^s for several initial phases.	71
4.7	θ^* dependence of the phase and of the flight time.	71
4.8	Lyapunov orbits in the SE-system and the Poincaré cuts of their unstable manifolds in Σ_c	75
4.9	Classification of initial conditions in $A_{I,II,III}^+$	77
4.10	Classification of initial conditions in $A_{IV,V}^+$	78

4.11	X - Y projection of trajectories generated by initial conditions in B_2^+ for C_I .	79
4.12	X - Y projection of trajectories generated by initial conditions in B_2^+ for C_{II} .	80
4.13	X - Y projection of trajectories generated by initial conditions in B_2^+ for C_{III} .	80
4.14	X - Y projection of trajectories generated by initial conditions in B_2^+ for C_{IV} .	81
4.15	X - Y projection of trajectories generated by initial conditions in B_2^+ for C_V .	81
4.16	Flight time of trajectories generated by initial conditions in B_2^+ for C_N .	82
4.17	Classification of initial conditions in A_*^+ .	84
4.18	Flight time of trajectories generated by initial conditions in B_2^+ for C_* .	84
5.1	Projection onto the x - y plane of the sets generated by the WSB algorithmic definition with positive initial velocity.	90
5.2	Projection onto the x - y plane of the sets generated by the WSB algorithmic definition with negative initial velocity.	91
5.3	Classification of $IC^+(e)$ and $IC^-(e)$ according to the Jacobi constant.	94
5.4	Spatial distribution of the \mathcal{C}^k sets, $k = 1,2,3,4,5$, for $IC^+(e)$ and $IC^-(e)$.	96
5.5	Grid dependence of the classification according to the Jacobi constant.	98
5.6	Variation of the \mathcal{C}^k , $k = 1,2,3,4,5$, percentage of initial conditions $IC^+(0.9)$ vs. $\log(\Delta r)$.	99
5.7	Variation of the \mathcal{C}^k , $k = 1,2,3,4,5$, percentage of initial conditions $IC^-(0.9)$ vs. $\log(\Delta r)$.	100
5.8	Variation of the \mathcal{C}^k , $k = 1,2,3,4,5$, percentage of $IC^+(0.9)$ points vs. the number of initial conditions.	101
5.9	Variation of the \mathcal{C}^k , $k = 1,2,3,4,5$, percentage of $IC^-(0.9)$ points vs. the number of initial conditions.	102
5.10	Criteria for direct inner transfers and for external transfers.	105

5.11 Retrograde analysis of $IC^+(0.6)$ and $IC^+(0.9)$ for application in direct inner transfers.	107
5.12 Retrograde analysis of $IC^-(0.6)$ and $IC^-(0.9)$ for application in direct inner transfers.	108
5.13 Poincaré section $\dot{x} = 0$, $\dot{y} > 0$ for $C = 3.06734276$	110
5.14 Detail of the B_2 region around the Earth at the Poincaré section $\dot{x} = 0$, $\dot{y} > 0$ for $C = 3.06734276$	111
5.15 Retrograde analysis of $IC^+(0.6)$ for application in external transfers.	113
5.16 Retrograde analysis of $IC^+(0.9)$ for application in external transfers.	114
5.17 Retrograde analysis of $IC^-(0.6)$ for application in external transfers.	115
5.18 Retrograde analysis of $IC^-(0.9)$ for application in external transfers.	116
5.19 Retrograde analysis of $S^+(0.6)$ and $S^+(0.9)$ for application in direct inner transfers.	122
5.20 Retrograde analysis of $S^-(0.6)$ and $S^-(0.9)$ for application in direct inner transfers.	123
5.21 Retrograde analysis of $S^+(0.6)$ for application in external transfers.	126
5.22 Retrograde analysis of $S^+(0.9)$ for application in external transfers.	127
5.23 Retrograde analysis of $S^-(0.6)$ for application in external transfers.	128
5.24 Retrograde analysis of $S^-(0.9)$ for application in external transfers.	129
5.25 Classification of stable initial conditions with positive and negative initial velocities according to the permanence within the Moon's sphere of influence during a full cycle.	131
5.26 Classification of stable initial conditions according to the position of the final state after a full cycle around the Moon with respect to the lunar SOI.	133

5.27	Projection onto the x - y plane of trajectories generated by stable initial conditions with positive initial velocity.	136
5.28	Projection onto the x - y plane of trajectories generated by stable initial conditions with negative initial velocity.	139
6.1	Boundaries of stability obtained through implementation A for $e = 0.9$. . .	147
6.2	Grid resolution issue in stable-unstable transitions.	149
6.3	Transition due to collision.	153
6.4	Transition due to the separatrix behavior of the invariant manifolds of a Lyapunov orbit.	155
6.5	S-G2 transition due to tangency.	157
6.6	S-E transition due to tangency.	158
6.7	Stable-primary interchange transitions due to constructive artifacts. . . .	160
6.8	S-E transition due to the measurement of the Kepler energy outside the lunar SOI	162
6.9	S-E transition due to the measurement of the Kepler energy inside the lunar SOI	163

List of Tables

4.1	Percentage of initial conditions in B_2^+ relative to the total number of initial conditions in each A_N^+ , corresponding to C_N , with $N = I, II, III, IV, V, \dots$	76
5.1	Percentage of initial conditions in each \mathcal{C}^k , $k = 1, 2, 3, 4, 5$, relative to the total number of initial conditions in each $IC^\pm(e)$ set.	97
5.2	Retrograde analysis of the complete sets of initial conditions for application in direct inner transfers.	109
5.3	Specific information of the trajectories generated by candidate stable initial conditions for application in direct inner transfers.	112
5.4	Retrograde analysis for application in external transfers.	117
5.5	Time performance of trajectories generated by initial conditions in $IC^\pm(e)$ for application in external transfers.	118
5.6	Number of stable initial conditions with positive and negative initial velocities for implementations A and B.	119
5.7	Retrograde analysis of stable initial conditions obtained through implementation A for application in direct inner transfers.	120
5.8	Retrograde analysis of stable initial conditions obtained through implementation A for application in external transfers.	121
5.9	Time performance of stable trajectories for application in external transfers.	124

5.10 Information of some trajectories generated by stable initial conditions with positive initial velocity	137
5.11 Information of some trajectories generated by stable initial conditions with negative initial velocity.	140
6.1 Stability configuration of initial conditions with positive initial velocity and $e = 0.9$ on the radial segment with $\theta = 0.64\pi$ rad for four different radial steps.	150

Summary

List of Figures	ix
List of Tables	xiii
Summary	xv
1 Introduction	18
2 Theoretical Framework	22
2.1 Equations of Motion	22
2.2 Points of Equilibrium	29
2.3 Regions of Motion	34
2.4 Lyapunov Orbits	35
2.5 Geometry of the Solutions Near the Collinear Equilibria	41
3 Weak Stability Boundaries	49
3.1 Capture in the PCR3BP	50
3.2 Approaches to Obtain Weakly Stable Regions	52
3.3 Comments on the Presented Definitions	57
4 Patched Three-Body Approach	60
4.1 Mechanism of Construction	62

4.1.1	Patching Procedure	66
4.2	Investigation of the Patching Procedure	68
4.2.1	Earth-Moon Portion	68
4.2.2	Sun-Earth Portion	72
4.2.3	Characterization of Trajectories in the Sun-Earth Portion	73
4.3	Discussion	85
5	WSB Associated Sets in the Lunar SOI	86
5.1	Implementations of the Algorithmic Definition	88
5.2	Classification of the Initial Conditions Sets According to the Jacobi Constant	93
5.2.1	Grid Dependence of the Classification According to the Jacobi Constant	97
5.3	Dynamical Investigation of Initial Condition Sets in the Lunar SOI	103
5.3.1	Retrograde Analyses for Direct Inner Transfers	106
5.3.2	Retrograde Analyses for External Transfers	112
5.4	Investigation of the Stable Set in the Lunar SOI	118
5.4.1	Retrograde Analyses of the Stable Set	119
5.4.2	Prograde Analyses of the Stable Set	125
5.4.3	Stable Set Obtained Through Implementation B	134
5.4.4	Diversity of Behavior in the Stable Set	135
5.5	Discussion	141
6	Stable-Unstable Transitions of the WSB	144
6.1	Extraction of the WSB	145
6.1.1	Collision Along the Stability Boundary	146
6.1.2	Refined Extraction	147

6.2	Transitions Due to Dynamical Effects	151
6.2.1	Collision and Close Approach to the Moon	151
6.2.2	Invariant Manifolds	152
6.3	Transitions Due to Constructive Effects of the Algorithm	156
6.3.1	Geometrical Criteria	156
6.3.2	Measurements of the Kepler Energy	161
6.4	Discussion	164
7	Conclusion	166
Bibliography		169
Appendix A - Constants		173
Appendix B - The Sphere of Influence		175
Appendix C - Regularization Theory		180
Appendix D - Lyapunov-Moser Theorem		182

1 Introduction

Traditional techniques employed to design space missions usually rely on two-body dynamics. Even complex missions involving three or more bodies and the flyby through distinct planets or satellites, like NASA's missions Voyager¹ and Galileo², can be projected using a Keplerian decomposition of the Solar System, such that the spacecraft's trajectory is approximated by a succession of two-body solutions. Nevertheless, there are situations at which the energy cost of the traditional approach becomes prohibitive. NASA's mission Genesis³, for example, was designed with trajectories that could not be approximated by Keplerian conics. In such cases, the N-body dynamics needs to be employed to obtain alternative solutions that reduce total fuel consumption.

However, the nonlinear three or four-body dynamics may be very intricate, in contrast to the simple conic solutions of the integrable two-body dynamics, where the evaluation of the Keplerian energy is enough to define if the trajectory is bounded (elliptic), unbounded (hyperbolic) or a boundary (parabolic) trajectory. Although the three-body gravitational problem has been studied for over 200 years by Euler, Lagrange, Poincaré, and many others, playing a central role both in Celestial Mechanics and in Chaos Theory, many aspects of its rich nonlinear dynamics still represent relevant challenges. Thus, to the development of modern space mission projects, it is important to characterize the trans-

¹<http://voyager.jpl.nasa.gov>

²<http://solarsystem.nasa.gov/galileo>

³<http://genesismission.jpl.nasa.gov>

port processes in the phase space and understand the role of the dynamical structures involved. In particular, the definition of regions of local effective stability is an important issue in order to exploit the dynamical characteristics of many-body systems.

Specifically, for a class of low-energy Earth-to-Moon transfers, the Weak Stability Boundary (WSB) concept, heuristically proposed by E. Belbruno [1], constitutes an initiative to establish stability boundaries related to temporary capture by the Moon, to reduce the energy cost required to stabilize the spacecraft's orbit at Moon's arrival. In these transfers, the gravitational effects of the Earth, the Moon, and the Sun are considered when modeling the motion of the spacecraft. The WSB concept aims to produce transfer trajectories in which the spacecraft approaches the Moon in a state defined as lunar ballistically captured, reducing the propellant mass needed to stabilize its motion into the final selenocentric orbit.

In the last years, the study of mission projects based on WSB strategy was motivated by the successful rescue of the Japanese Hiten mission to the Moon [2, 3]. Originally, the method of construction of Hiten-like transfer trajectories was associated to the WSB or fuzzy boundary region which is located approximately 1.5 million km away from the Earth in the Sun-Earth direction and is described as a "*region in the phase space where the perturbative effects of the Earth-Moon-Sun acting on the spacecraft tend to balance*" [3]. Alternatively, such transfer trajectories can be obtained considering the *patched three-body approach* presented by W. Koon *et al.* [4, 5]. This model approximates the four-body system (Sun-Earth-Moon-spacecraft) as two coupled three-body systems: Sun-Earth-sc and Earth-Moon-sc. The construction of transfer orbits is based on the transport channels provided by the invariant manifolds associated to unstable periodic orbits of these two subsystems.

At least three distinct definitions share the WSB terminology: (i) the aforementioned qualitative region defined in the phase space where gravitational forces cancel each other [1, 3, 6], (ii) an algorithmic definition based on the dynamical evolution of a specific set of initial conditions which are classified according to certain stability criteria [3, 7, 8], and (iii) an analytical approximation constructed as the intersection of three subsets of the phase space [7, 9].

The algorithmic WSB definition has been numerically built and specific applications have been considered by some authors [8, 10, 11]. This definition was not mathematically deduced, but heuristically proposed mixing elements inherent in a two-body dynamics with the time evolution of sets of initial conditions under a restricted three-body dynamics. These sets, which are defined around the Moon for fixed osculating ellipse eccentricity with both positive and negative initial velocities, are classified according to a proposed stability criterion in order to obtain the stability boundary.

However, the current literature on the subject lacks an extensive investigation of the sets that result from the classification procedure and the nature of stable-unstable transitions produced by the proposed definition is still not deeply comprehended.

Thus, the goals of this work are: (i) to examine and characterize the construction of Earth-to-Moon trajectories, isolating the relevant dynamical ingredients for feasible transfer orbits in the Earth-Moon and Sun-Earth portions of the complete mission, (ii) to characterize the algorithmic WSB associated sets of initial conditions and investigate the applicability of the generated trajectories in light of ballistic capture transfers, (iii) to elucidate the dynamical characteristics of the stability boundary through the detection of the mechanisms which are responsible for the transitions, separating dynamical elements from constructive artifacts, and (iv) to verify the consistency of the constructive procedure

concerning the achievement of temporary capture trajectories.

Organization of the text: This text is organized as follows. In Chapter 2, we describe the Planar Circular Restricted Three-Body Problem (PCR3BP), the mathematical model that provides the dynamical framework in which the WSB has been defined. In Chapter 3, we present a brief discussion of capture in the PCR3BP and describe three different approaches to obtain weakly stable regions, stating the WSB algorithmic definition and its analytical approximation. In Chapter 4, we investigate the role of the dynamical structures of the PCR3BP in the determination of lunar capture orbits and identify the relevant dynamical ingredients to construct Earth-to-Moon trajectories in the *patched three-body approach*. In Chapter 5, we present a number of original characterization procedures in order to analyse the WSB algorithmic definition extensively and verify its practical applicability. In Chapter 6, we extract the WSB and investigate its dynamical characteristics, detecting the mechanisms which are responsible for the stable-unstable transitions and verifying the consistency of the constructive procedure concerning the achievement of temporary capture trajectories. Finally, the last chapter is dedicated to the concluding remarks.

2 Theoretical Framework

The Planar Circular Restricted Three-Body Problem (PCR3BP) provides the dynamical framework in which the WSB has been defined. In this Chapter, we describe the mathematical model and review some relevant features of this dynamical system. For a more detailed approach we refer the reader to Refs. [12] and [13].

Organization of the Chapter: In Sections 2.1, 2.2, and 2.3 the equations of motion, the points of equilibrium, and the regions of motion are presented. Section 2.4 deals with the periodic orbits around the collinear equilibria and Section 2.5 deals with the solutions near the collinear equilibria.

2.1 Equations of Motion

The Restricted Three-Body Problem (R3BP) describes the motion of a particle P_3 of negligible mass m_3 , moving under the gravitational influence of two bodies P_1 and P_2 , called the primaries, of masses m_1 and m_2 , respectively. The motion of P_1 and P_2 is not perturbed by P_3 , being a solution of a Kepler Problem, with the two bodies moving under mutual gravitational influence.

In the planar circular version of the R3BP, the PCR3BP, P_1 and P_2 describe circular coplanar orbits around the barycenter of this two-body system and the motion of the third body is restricted to the orbital plane of the primaries. This model is suited to describe the

Earth-Moon-spacecraft system (*Earth* $\Leftrightarrow P_1$, *Moon* $\Leftrightarrow P_2$, *spacecraft* $\Leftrightarrow P_3$), given that the mean eccentricity of the Moon's orbit around the Earth is 0.0549 and its inclination with respect to the orbit of the planet is $5^\circ 09'$. Moreover, since the eccentricity of the Earth's orbit around the Sun is 0.0167, the Sun-Earth-spacecraft system can also be described by means of the PCR3BP [14].

Consider the inertial reference frame (X, Y) , also called sidereal coordinate system, with origin at the barycenter of the P_1 - P_2 two-body system. In this coordinate system, the positions of the masses m_1 and m_2 , given by (X_1, Y_1) and (X_2, Y_2) , respectively, are time dependent and can be obtained by inspecting Figure 2.1:

$$\begin{aligned} X_1 &= b \cos nt', & X_2 &= -a \cos nt', \\ Y_1 &= b \sin nt', & Y_2 &= -a \sin nt', \end{aligned} \tag{2.1}$$

where $b = \sqrt{X_1^2 + Y_1^2}$ and $a = \sqrt{X_2^2 + Y_2^2}$ are, respectively, the distances of P_1 and P_2 to the origin, n is the angular velocity of the primaries, also called mean motion, and t' is used to denote the time variable, thus reserving t to the non-dimensional time variable that will be introduced later on.

The distributions of the masses of P_1 and P_2 are such that they can be taken as punctual masses.

For the two-body system P_1 - P_2 , applying Newton's law of universal gravitation, the modulus of the force \mathbf{F}_g exerted on P_1 by P_2 (and on P_2 by P_1) is given by

$$|\mathbf{F}_g| = \frac{G m_1 m_2}{l^2}, \tag{2.2}$$

where $l = a + b$ is the distance between the primaries and G is the universal gravitational

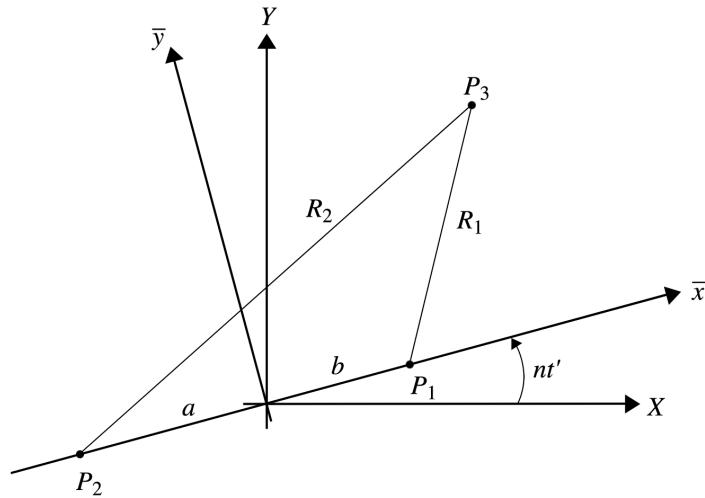


FIGURE 2.1 – The \bar{x} - \bar{y} synodic coordinate frame rotates with respect to the X - Y inertial reference frame.

constant.

Given that the gravitational force acting on each primary must balance the centrifugal force, we can write

$$G \frac{m_1 m_2}{l^2} = m_2 a n^2 = m_1 b n^2. \quad (2.3)$$

Then, from Equation (2.3), we find

$$G m_1 = a n^2 l^2, \quad G m_2 = b n^2 l^2, \quad \text{and} \quad G(m_1 + m_2) = n^2 l^3, \quad (2.4)$$

where the last equation is the third law of Kepler.

The equations of motion of P_3 in the inertial coordinate system are

$$\frac{d^2 X}{dt'^2} = -\frac{\partial U}{\partial X} \quad \text{and} \quad \frac{d^2 Y}{dt'^2} = -\frac{\partial U}{\partial Y}, \quad (2.5)$$

where $U(X, Y, t')$ is the potential, which depends explicitly on the time because of the

motion of the primaries and is given by

$$U(X, Y, t') = -G \left(\frac{m_1}{R_1} + \frac{m_2}{R_2} \right), \quad (2.6)$$

with R_1 and R_2 , which are the distances from P_3 to P_1 and to P_2 , respectively, given by

$$R_1 = \sqrt{(X - X_1)^2 + (Y - Y_1)^2} \quad \text{and} \quad R_2 = \sqrt{(X - X_2)^2 + (Y - Y_2)^2}. \quad (2.7)$$

The total energy of P_3 per unit mass is

$$h_3 = \frac{1}{2} \left[\left(\frac{dX}{dt'} \right)^2 + \left(\frac{dY}{dt'} \right)^2 \right] + U(X, Y, t'), \quad (2.8)$$

and the energy of the P_1 - P_2 system is

$$H_{12} = \frac{1}{2} n^2 (m_1 b^2 + m_2 a^2) - G \frac{m_1 m_2}{l}. \quad (2.9)$$

So the total energy of the three-body system can be written as

$$H = h_3 + H_{12}, \quad (2.10)$$

which is not constant along an orbit since h_3 depends explicitly on the time because of the motion of the primaries with respect to the inertial reference frame.

A coordinate transformation can be introduced in order to obtain the equations of

motion in a coordinate system (\bar{x}, \bar{y}) in which P_1 and P_2 are fixed:

$$\begin{pmatrix} X \\ Y \end{pmatrix} = \mathbf{R} \begin{pmatrix} \bar{x} \\ \bar{y} \end{pmatrix}, \quad (2.11)$$

where \mathbf{R} is the matrix of the rotation transformation

$$\mathbf{R} = \begin{bmatrix} \cos nt' & -\sin nt' \\ \sin nt' & \cos nt' \end{bmatrix}. \quad (2.12)$$

Introducing the complex variables

$$Z = X + iY = ze^{int'}, \quad z = \bar{x} + i\bar{y}, \quad (2.13)$$

the new equations of motion can be written as

$$\begin{aligned} \frac{d^2\bar{x}}{dt'^2} - 2n\frac{d\bar{y}}{dt'} &= -\frac{\partial U^*}{\partial \bar{x}}, \\ \frac{d^2\bar{y}}{dt'^2} + 2n\frac{d\bar{x}}{dt'} &= -\frac{\partial U^*}{\partial \bar{y}}, \end{aligned} \quad (2.14)$$

where

$$U^*(\bar{x}, \bar{y}) = -\frac{n^2}{2}(\bar{x}^2 + \bar{y}^2) - G \left(\frac{m_1}{\bar{r}_1} + \frac{m_2}{\bar{r}_2} \right) \quad (2.15)$$

is the new potential, obtained directly from Equation (2.6) through the introduced coordinate transformation, with $\bar{r}_1 = \sqrt{(\bar{x} - b)^2 + \bar{y}^2}$ and $\bar{r}_2 = \sqrt{(\bar{x} + a)^2 + \bar{y}^2}$.

The new equations of motion, Equation (2.14), possess an integral of the motion. By multiplying the first equation by $d\bar{x}/dt'$, the second by $d\bar{y}/dt'$, adding both and integrating

with respect to the time t' , and using

$$dU^* = \frac{\partial U^*}{\partial \bar{x}} d\bar{x} + \frac{\partial U^*}{\partial \bar{y}} d\bar{y}, \quad (2.16)$$

we obtain

$$\frac{1}{2} \left[\left(\frac{d\bar{x}}{dt'} \right)^2 + \left(\frac{d\bar{y}}{dt'} \right)^2 \right] = - \int_{t'_0}^{t'} \left(\frac{\partial U^*}{\partial \bar{x}} d\bar{x} + \frac{\partial U^*}{\partial \bar{y}} d\bar{y} \right) = -U^* - \frac{C^*}{2}. \quad (2.17)$$

Thus, we have

$$J^* \left(\bar{x}, \bar{y}, \frac{d\bar{x}}{dt'}, \frac{d\bar{y}}{dt'} \right) = \frac{1}{2} \left[\left(\frac{d\bar{x}}{dt'} \right)^2 + \left(\frac{d\bar{y}}{dt'} \right)^2 \right] + U^* = -\frac{C^*}{2} \quad (2.18)$$

which is the only known integral of motion of the PCR3BP.

This dynamical model can be expressed in non-dimensional variables, in such a way that the distance between P_1 and P_2 , the sum of their masses and their angular velocity around the barycenter are normalized to one.

Using Kepler's third law, expressed in Equation (2.4), and introducing

$$\begin{aligned} x &= \bar{x}/l, & y &= \bar{y}/l, & t &= nt', \\ r_1 &= \bar{r}_1/l, & r_2 &= \bar{r}_2/l, & \mu_{1,2} &= m_{1,2}/(m_1 + m_2), \end{aligned} \quad (2.19)$$

the equations of motion, Equation (2.14), become

$$\begin{aligned} \ddot{x} - 2\dot{y} &= \Omega_x, \\ \ddot{y} + 2\dot{x} &= \Omega_y, \end{aligned} \quad (2.20)$$

where the dots denote differentiation with respect to the dimensionless time t and the

subscripts indicate partial derivatives with respect to x and y . The function Ω corresponds to

$$\Omega \equiv \bar{\Omega} + \frac{1}{2}\mu_1\mu_2, \quad (2.21)$$

with

$$\bar{\Omega} = -\frac{U^*}{l^2 n^2} = \frac{1}{2}(x^2 + y^2) + \frac{\mu_1}{r_1} + \frac{\mu_2}{r_2}, \quad (2.22)$$

where r_1 and r_2 are the distances from P_3 to P_1 and to P_2 , respectively, given by

$$r_1^2 = (x - 1 + \mu_1)^2 + y^2, \quad \text{and} \quad r_2^2 = (x + 1 - \mu_2)^2 + y^2. \quad (2.23)$$

The additive constant $\frac{1}{2}\mu_1\mu_2$ is included due to a convenience associated to the equilibrium points of the system, as it will be seen.

Since $\mu_1 + \mu_2 = 1$, we can set $\mu_2 = \mu$. Then, $\mu_1 = 1 - \mu$ and the problem depends only of the mass parameter μ , with $0 \leq \mu \leq 1$. When $\mu = 0$ and $\mu = 1$, the model corresponds to a unitary mass at the origin and when $\mu = \frac{1}{2}$, we have two equal masses located at $x = \pm\frac{1}{2}$. Throughout this text, P_1 is located at $(x_{P1}, y_{P1}) = (\mu, 0)$, to the right of the center of mass which is at the origin of the synodic coordinate system, and P_2 is located to the left of the origin at $(x_{P2}, y_{P2}) = (-1 + \mu, 0)$. When $0 \leq \mu < \frac{1}{2}$, P_1 and P_2 are located, respectively, at $0 \leq x < \frac{1}{2}$ and $-1 \leq x < -\frac{1}{2}$, and when $\frac{1}{2} < \mu \leq 1$ the larger primary is located at $\frac{1}{2} < x \leq 1$ and the smaller one is located at $-\frac{1}{2} < x \leq 0$.

Thus, we have

$$\Omega = \frac{1}{2}(x^2 + y^2) + \frac{1 - \mu}{r_1} + \frac{\mu}{r_2} + \frac{\mu(1 - \mu)}{2}, \quad (2.24)$$

and the Jacobi integral is

$$J(x, y, \dot{x}, \dot{y}) = 2\Omega(x, y) - (\dot{x}^2 + \dot{y}^2) = C. \quad (2.25)$$

The Jacobi constant C is usually associated to an energy integral through $C = -2E$.

The conservation associated to J defines a three-dimensional invariant manifold immersed in the four-dimensional phase space by

$$\mathcal{M}(\mu, C) = \{(x, y, \dot{x}, \dot{y}) \in \mathbb{R}^4 | J(x, y, \dot{x}, \dot{y}) = \text{constant}\}, \quad (2.26)$$

so that the motion in the phase space is restricted to the manifold $\mathcal{M}(\mu, C)$.

2.2 Points of Equilibrium

The dynamical model has five equilibrium points, also called libration or Lagrangian points, defined by

$$\frac{\partial J}{\partial x} = \Omega_x = 0, \quad \frac{\partial J}{\partial y} = \Omega_y = 0, \quad \frac{\partial J}{\partial \dot{x}} = 0 \Rightarrow \dot{x} = 0, \quad \frac{\partial J}{\partial \dot{y}} = 0 \Rightarrow \dot{y} = 0. \quad (2.27)$$

These equilibria are stationary solutions, so that P_3 does not move in the synodic reference frame. They correspond to states at which the forces acting on the third body in the rotating system are balanced, hence P_3 moves in a circular orbit with the same frequency as the primaries in the inertial reference frame.

Writing $\Omega_x = 0$ and $\Omega_y = 0$ explicitly we obtain

$$x - \frac{(1-\mu)(x-\mu)}{r_1^3} - \frac{\mu(x+1-\mu)}{r_2^3} = 0, \quad (2.28)$$

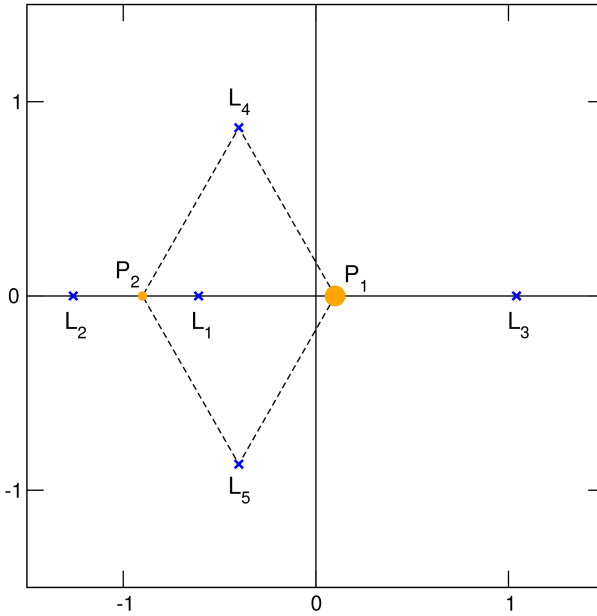


FIGURE 2.2 – Equilibrium points of the PCR3BP in the synodic reference frame for $\mu = 0.1$.

$$y \left(1 - \frac{1-\mu}{r_1^3} - \frac{\mu}{r_2^3} \right) = 0. \quad (2.29)$$

Solving the system of Equations (2.28,2.29), we obtain three *collinear solutions*, L_k , $k = 1,2,3$, located on the x -axis, and two *triangular solutions*, L_k , $k = 4,5$, located at the vertices of equilateral triangles formed with the positions of primaries, as shown in Figure 2.2.

Writing $r_1 = r_2 = 1$ in Equation (2.29) we obtain $x = \mu - \frac{1}{2}$ and $y = \pm \frac{\sqrt{3}}{2}$, which are the coordinates of the triangular solutions, also called equilateral points. The collinear equilibria have $y = 0$ and the values of the abscissas are found solving the fifth order algebraic equation (Equation (2.28)).

In order to study the motion near the five equilibrium points $L_k(a_k, b_k)$, with $k = 1, 2, 3, 4, 5$, and a_k and b_k the abscissa and the ordinate, respectively, corresponding to the position of each equilibrium point, we write

$$x = a_k + \xi \quad \text{and} \quad y = b_k + \eta, \quad (2.30)$$

where ξ and η are coordinates relative to L_k . From now on, we will drop the subindex k and refer to a generic equilibrium point $L(a, b)$, so that, for $L_{1,2,3}$, we have $(a, b) = (x_{1,2,3}, 0)$, and $(a, b) = (\mu - 1, \pm \frac{\sqrt{3}}{2})$ for $L_{4,5}$.

The function Ω can be expanded in power series around L , giving

$$\Omega = \Omega(a, b) + \Omega_x(a, b)\xi + \Omega_y(a, b)\eta + \frac{1}{2}\Omega_{xx}(a, b)\xi^2 + \Omega_{xy}(a, b)\xi\eta + \frac{1}{2}\Omega_{yy}(a, b)\eta^2 + \mathcal{O}(3) \quad (2.31)$$

and the equations of motion (Equation (2.20)) become

$$\begin{aligned} \ddot{\xi} - 2\dot{\eta} &= \Omega_{xx}(a, b)\xi + \Omega_{xy}(a, b)\eta + \mathcal{O}(2), \\ \ddot{\eta} + 2\dot{\xi} &= \Omega_{xy}(a, b)\xi + \Omega_{yy}(a, b)\eta + \mathcal{O}(2). \end{aligned} \quad (2.32)$$

If the higher-order terms $\mathcal{O}(2)$ are omitted, we obtain the linear variational equations.

By introducing

$$\begin{aligned} x_1 &= \xi, & \dot{x}_3 &= \dot{\xi}, \\ x_2 &= \eta, & \dot{x}_4 &= \dot{\eta}, \end{aligned} \quad (2.33)$$

the second-order system of Equation (2.32) can be written as a system of four first-order equations. Thus, in matrix form, the linear variational equations are

$$\dot{\mathbf{x}} = \mathbf{A}\mathbf{x}, \quad (2.34)$$

where $\mathbf{x}^T = (x_1, x_2, x_3, x_4)$ and the matrix \mathbf{A} is

$$\mathbf{A} = \begin{bmatrix} \mathbf{0} & \mathbf{I} \\ \mathbf{B} & \mathbf{C} \end{bmatrix}, \quad (2.35)$$

with

$$\mathbf{B} = \begin{bmatrix} \Omega_{xx}^0 & \Omega_{xy}^0 \\ \Omega_{xy}^0 & \Omega_{yy}^0 \end{bmatrix}, \quad \mathbf{C} = \begin{bmatrix} 0 & 2 \\ -2 & 0 \end{bmatrix}, \quad \mathbf{I} = \begin{bmatrix} 1 & 0 \\ 0 & 1 \end{bmatrix}, \quad (2.36)$$

where Ω_{xx}^0 , Ω_{yy}^0 and Ω_{xy}^0 are, respectively, Ω_{xx} , Ω_{yy} and Ω_{xy} computed at the equilibrium point L .

The eigenvalues of the equilibrium points are the roots of the characteristic polynomial

$$\mathcal{P}(\lambda) = \lambda^4 + (4 - \Omega_{xx}^0 - \Omega_{yy}^0)\lambda^2 + \Omega_{xx}^0\Omega_{yy}^0 - (\Omega_{xy}^0)^2. \quad (2.37)$$

For $L_{1,2,3}$ and $0 < \mu < \frac{1}{2}$, we have $\Omega_{xy} = 0$, $\Omega_{xx} > 0$, $\Omega_{yy} < 0$ and $\Omega_{xx}^0\Omega_{yy}^0 - (\Omega_{xy}^0)^2 < 0$.

Setting $\lambda^2 = \Lambda$, we rewrite the characteristic polynomial as

$$\mathcal{P}(\Lambda) = \Lambda^2 + 2\beta_1\Lambda - \beta_2^2 = 0, \quad (2.38)$$

where

$$\beta_1 = 2 - \frac{\Omega_{xx}^0 + \Omega_{yy}^0}{2}, \quad \text{and} \quad \beta_2^2 = -\Omega_{xx}^0\Omega_{yy}^0 > 0, \quad (2.39)$$

such that,

$$\Lambda_1 = -\beta_1 + \sqrt{\beta_1^2 + \beta_2^2} > 0, \quad \Lambda_2 = -\beta_1 - \sqrt{\beta_1^2 + \beta_2^2} < 0 \quad (2.40)$$

and

$$\lambda_{1,2} = \pm\sqrt{\Lambda_1}, \quad \lambda_{3,4} = \pm\sqrt{\Lambda_2}. \quad (2.41)$$

Thus, we obtain two real roots, λ_1 and λ_2 , and two imaginary roots, λ_3 and λ_4 , so these solutions are unstable.

On the other hand, for $L_{4,5}$, we have

$$\Omega_{xx}(L_{4,5}) = \frac{3}{4}, \quad \Omega_{yy}(L_{4,5}) = \frac{9}{4} \quad \text{and} \quad \Omega_{xy}(L_{4,5}) = \pm \frac{3\sqrt{3}}{2} \left(\mu - \frac{1}{2} \right), \quad (2.42)$$

such that the characteristic polynomial is

$$\mathcal{P}(\lambda) = \lambda^4 + \lambda^2 + \frac{27}{4}\mu(1-\mu) \quad (2.43)$$

or, by using $\Lambda = \lambda^2$,

$$\mathcal{P}(\Lambda) = \Lambda^2 + \Lambda + \frac{27}{4}\mu(1-\mu), \quad (2.44)$$

Setting $\mathcal{P}(\Lambda) = 0$, we find the roots of the characteristic polynomial to be

$$\Lambda_{1,2} = \frac{-1 \pm \sqrt{d}}{2}, \quad (2.45)$$

with $d = 1 - 27\mu(1-\mu)$, $\lambda_{1,2} = \pm\sqrt{\Lambda_1}$ and $\lambda_{3,4} = \pm\sqrt{\Lambda_2}$. The roots of the discriminant, that is, the solutions of the equation $d = 0$, are $\mu_0 = \frac{1}{2} \left[1 - \sqrt{\frac{23}{27}} \right]$ and $\mu_1 = 1 - \mu_0$. So, when $0 \leq \mu < \mu_0$, the equilibrium point L is linearly stable, because we have two pairs of pure imaginary eigenvalues, while it is unstable when $\mu_0 < \mu \leq \frac{1}{2}$, because the real part of two of the eigenvalues is positive. For $\mu = \mu_0$, the solution contains secular terms and L is also unstable.

The Jacobi constant values evaluated in these static solutions are denoted by C_k , $k = 1, 2, 3, 4, 5$.

2.3 Regions of Motion

The regions obtained by the projection of the \mathcal{M} surface onto the position space x - y are called the *Hill regions*, \mathcal{H} , defined by

$$\mathcal{H}(\mu, C) = \{(x, y) | \Omega(x, y) \geq C/2\}, \quad (2.46)$$

given that we must have $\dot{x}^2 + \dot{y}^2 = 2\Omega(x, y) - C \geq 0$. They constitute the accessible areas to the trajectories for each given C , or analogously, for each energy value.

The Hill regions are bounded by the *zero-velocity curves* which are the locus of points in the x - y plane where the kinetic energy of P_3 vanishes.

For a given μ , there are five basic configurations for these regions, defined by the C_k values. Figure 2.3 shows the values of C_k as a function of the mass parameter and Figure 2.4 displays the first four Hill regions configurations for $\mu = 0.3$. Before proceeding with the description of each case, we define the following terminology:

R^{P_1} : accessible region surrounding P_1 .

R^{P_2} : accessible region surrounding P_2 .

R^E : accessible region that lies outside both P_1 and P_2 realms and extends to infinity.

Case 1: When $C > C_1$, the particle cannot transit from R^{P_1} to R^{P_2} , and vice versa.

Also, P_3 cannot transit between these regions and R^E . That is, the three realms of accessible motion are not connected.

Case 2: When $C_1 > C > C_2$, the realms around the primaries are connected through a neck region around L_1 . Thereby, P_3 can move from R^{P_1} and R^{P_2} , and vice versa.

Case 3: When $C_2 > C > C_3$, there is a neck region around L_2 , besides the connecting

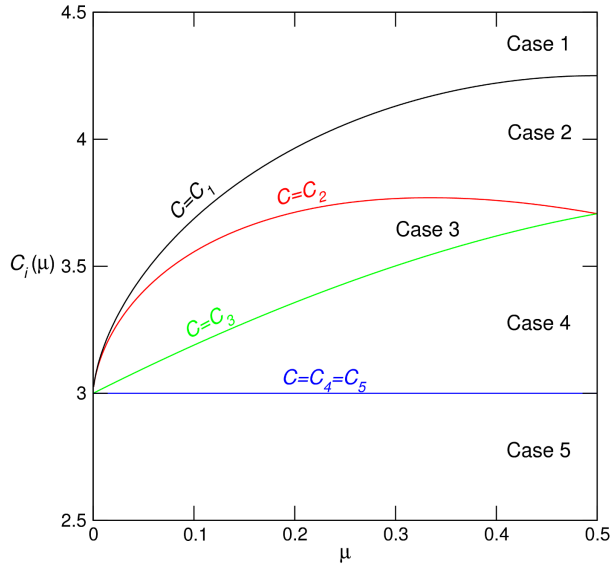


FIGURE 2.3 – C_k , $k = 1,2,3,4,5$, as a function of μ . For each μ the values of C_k define the five possible Hill region cases.

region around L_1 . So, in addition to the possibility of transit between the realms surrounding the primaries, now the particle can move to R^E , and vice versa.

Case 4: When $C_3 > C > C_4 = C_5$, a neck around L_3 opens, increasing the possibility of transit between R^{P_1} , R^{P_2} and R^E . The inaccessible regions diminish as C decreases.

Case 5: Finally, when $C_4 = C_5 > C$, all of the x - y plane is accessible to the particle.

2.4 Lyapunov Orbits

The solutions of the linearized system, i.e., Equation (2.32) after neglecting $\mathcal{O}(2)$ terms, have the form

$$\xi = \sum_{i=1}^4 A_i e^{\lambda_i t}, \quad \eta = \sum_{i=1}^4 B_i e^{\lambda_i t}, \quad (2.47)$$

where A_i and B_i , $i = 1,2,3,4$ are eight constant real numbers determined by the initial conditions of Equation (2.32), $\xi_0 = \xi(t_0)$, $\eta_0 = \eta(t_0)$, $\dot{\xi}_0 = \dot{\xi}(t_0)$, and $\dot{\eta}_0 = \dot{\eta}(t_0)$ and by

$$(\lambda_i^2 - \Omega_{xx}^0) A_i = (2\lambda_i + \Omega_{xy}^0) B_i, \quad i = 1, 2, 3, 4. \quad (2.48)$$

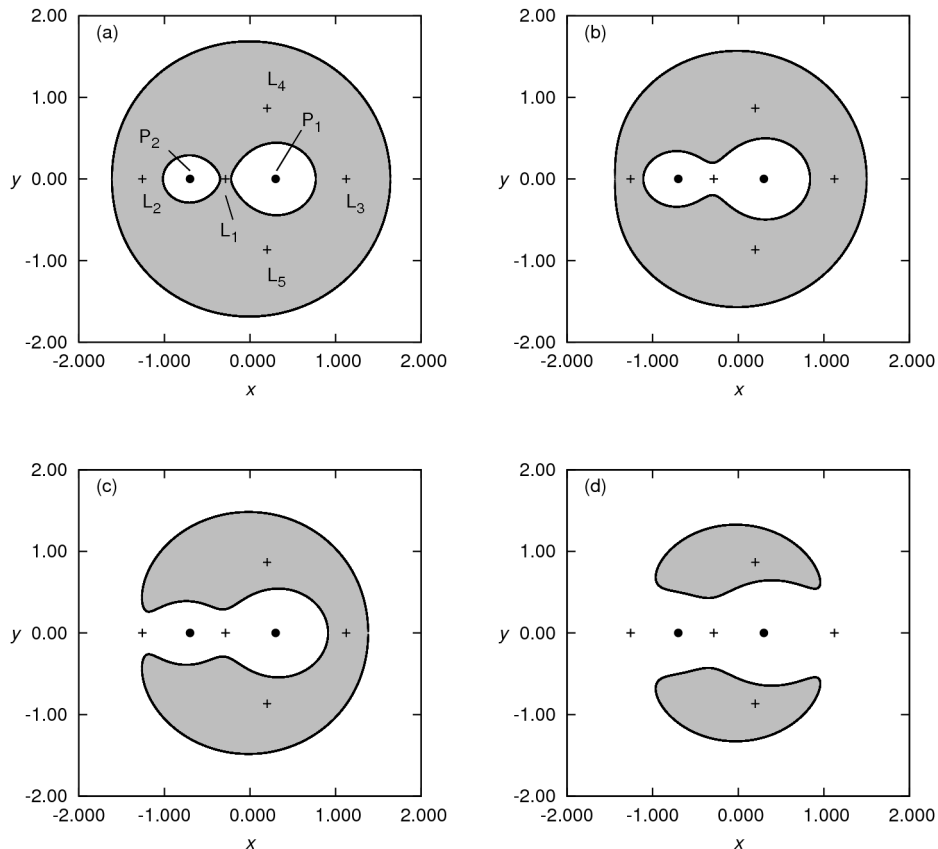


FIGURE 2.4 – Four possible Hill Region cases for $\mu = 0.3$: the white areas correspond to the Hill regions. The inaccessible areas and the zero velocity curves are shown in grey and black, respectively. The black filled circles correspond to the primaries and the plus signs to the equilibrium points $L_k, k = 1, 2, 3, 4, 5$. **(a)** Case 1 ($C > C_1$): no transit orbits between the primaries are possible. **(b)** Case 2 ($C_1 > C > C_2$): the realms around P_1 and P_2 are connected by transit orbits through the neck region around L_1 . **(c)** Case 3 ($C_2 > C > C_3$): in addition to the transit possibility of case 2, now the particle can move to the exterior realm of motion through the neck region around L_2 . **(d)** Case 4 ($C_3 > C > C_4 = C_5$): there is a neck region also around L_3 . In the fifth case ($C < C_4 = C_5$), motion over the entire x - y plane is possible.

For the collinear equilibria, we have $\Omega_{xy}^0 = 0$, so

$$B_i = \frac{\lambda_i^2 - \Omega_{xx}^0}{2\lambda_i} A_i = \alpha_i A_i \quad (2.49)$$

and

$$\begin{aligned} \xi_0 &= \sum_{i=1}^4 A_i e^{\lambda_i t_0}, & \eta_0 &= \sum_{i=1}^4 \alpha_i A_i e^{\lambda_i t_0}, \\ \dot{\xi}_0 &= \sum_{i=1}^4 \lambda_i A_i e^{\lambda_i t_0}, & \dot{\eta}_0 &= \sum_{i=1}^4 \alpha_i \lambda_i A_i e^{\lambda_i t_0}. \end{aligned} \quad (2.50)$$

By taking the inverse of Equations (2.50) we obtain the four coefficients

$$\begin{aligned} A_1 &= \frac{e^{-\lambda_1 t_0}}{\lambda_1^2 - \lambda_3^2} \left[-\xi_0 \alpha_3 \lambda_3 - \dot{\xi}_0 \alpha_3 \delta + \eta_0 \lambda_3 \delta + \dot{\eta}_0 \right], \\ A_2 &= \frac{e^{\lambda_1 t_0}}{\lambda_1^2 - \lambda_3^2} \left[-\xi_0 \alpha_3 \lambda_3 + \dot{\xi}_0 \alpha_3 \delta - \eta_0 \lambda_3 \delta + \dot{\eta}_0 \right], \\ A_3 &= \frac{e^{-\lambda_3 t_0}}{\lambda_1^2 - \lambda_3^2} \left[\xi_0 \alpha_1 \lambda_1 + \dot{\xi}_0 \alpha_1 \delta - \eta_0 \lambda_1 \delta - \dot{\eta}_0 \right], \\ A_4 &= \frac{e^{\lambda_3 t_0}}{\lambda_1^2 - \lambda_3^2} \left[\xi_0 \alpha_1 \lambda_1 - \dot{\xi}_0 \alpha_1 \delta + \eta_0 \lambda_1 \delta - \dot{\eta}_0 \right], \end{aligned} \quad (2.51)$$

where $\delta = \sqrt{\Omega_{yy}^0 / \Omega_{xx}^0}$.

Given that the coefficients A_1 and A_2 are associated to the real exponents λ_1 e λ_2 (Equation (2.41)), the first two terms on the right side of Equations (2.47) account for exponential increase and decay of the solutions with time. A particular solution containing only sine and cosine functions of the time can be obtained by choosing initial conditions such that $A_1 = A_2 = 0$.

For the collinear points and $A_1 = A_2 = 0$, Equation (2.47) gives

$$\xi = A_3 e^{\lambda_3 t} + A_4 e^{-\lambda_3 t} \quad \text{e} \quad \eta = A_3 \alpha_3 e^{\lambda_3 t} - A_4 \alpha_3 e^{-\lambda_3 t}, \quad (2.52)$$

and, substituting the expressions for A_3 and A_4 ,

$$\begin{aligned}\xi &= \xi_0 \cos s(t - t_0) + (\eta_0/\beta_3) \sin s(t - t_0), \\ \eta &= \eta_0 \cos s(t - t_0) - \beta_3 \xi_0 \sin s(t - t_0),\end{aligned}\tag{2.53}$$

where the real quantities s and β are defined by

$$s = +\sqrt{\beta_1 + \sqrt{\beta_1^2 + \beta_2^2}} \quad \text{or} \quad \lambda_3 = is,\tag{2.54}$$

and

$$\beta_3 = \frac{s^2 + \Omega_{xx}^0}{2s} \quad \text{or} \quad \alpha_3 = i\beta_3.\tag{2.55}$$

Once the initial conditions ξ_0 and η_0 are chosen, the corresponding initial velocities cannot be chosen at will, given that Equation (2.53) gives

$$\dot{\xi}_0 = \eta_0 s / \beta_3 \quad \text{and} \quad \dot{\eta}_0 = -\beta_3 \xi_0 s.\tag{2.56}$$

Solving the system given by Equation (2.52) for $A_3 e^{\lambda_3 t}$ and $A_4 e^{-\lambda_3 t}$, we find that the solution is an elliptic orbit with semi-major axis perpendicular to the x -axis. Eliminating the time, we find

$$\xi^2 + \eta^2 / \beta_3^2 = \xi_0^2 + \eta_0^2 / \beta_3^2.\tag{2.57}$$

The motion along the orbit is retrograde, i.e., in clockwise sense, since at $\xi = \xi_0 > 0$ and $\eta = \eta_0 = 0$, Equation (2.56) gives $\dot{\xi}_0 = 0$ and $\dot{\eta}_0 < 0$.

Let ϵ be a continuation parameter connected to the Jacobi constant [12]. For $\epsilon \neq 0$ but sufficiently small, the analytic continuation of the solutions of the linearized system indicates the existence of retrograde periodic orbits around L_k in the nonlinear case, for

all $0 < \mu < 1/2$. These periodic solutions of the nonlinear system, shown in Figure 2.5(a), are called Lyapunov orbits and constitute one of the families of symmetric periodic orbits of the PCR3BP. For a given $C < C_k$, $k = 1, 2, 3$, there exists exactly one of these periodic solutions around the corresponding L_k point. The Lyapunov orbits lie on the two-dimensional central manifold associated to each collinear equilibrium point and can be obtained through the periodic solutions of the linearized system.

For the triangular equilibria, the results of a similar development are described in details in Ref. [12].

Introducing $x_1 = x$, $x_2 = y$, $x_3 = \dot{x}$, and $x_4 = \dot{y}$, the nonlinear system given by Equation (2.20) can be rewritten as

$$\dot{\mathbf{x}} = f(\mathbf{x}), \quad (2.58)$$

where $\mathbf{x} = (x_1, x_2, x_3, x_4)^T$ and f is the vector field of the PCR3BP. For a given initial condition $\mathbf{x}_0 = (x_1^0, x_2^0, x_3^0, x_4^0)^T$, the flow or solution curve of Equation (2.58) is $\phi(\mathbf{x}_0, [t_0, t])$ such that

$$\frac{d}{dt} \phi(\mathbf{x}_0, [t_0, t]) = f(\phi(\mathbf{x}_0, [t_0, t])), \quad (2.59)$$

with $\phi(\mathbf{x}_0, [t_0, t = t_0]) = \mathbf{x}_0$.

Differentiating Equation (2.59) with respect to x_0 and using the chain rule we have

$$\begin{aligned} D_{\mathbf{x}_0} \left[\frac{d}{dt} \phi(\mathbf{x}_0, [t_0, t]) \right] &= D_{\mathbf{x}_0} f(\phi(\mathbf{x}_0, [t_0, t])) \\ \frac{d}{dt} [D_{\mathbf{x}_0} \phi(\mathbf{x}_0, [t_0, t])] &= D_{\mathbf{x}} f(\phi(\mathbf{x}_0, [t_0, t])) D_{\mathbf{x}_0} \phi(\mathbf{x}_0, [t_0, t]), \end{aligned} \quad (2.60)$$

and, evaluating the flow at $t = t_0$, we obtain $D_{\mathbf{x}_0} \phi(\mathbf{x}_0, [t_0, t = t_0]) = \mathbf{I}$.

Defining $\Phi(\mathbf{x}_0, t) = D_{\mathbf{x}_0}\phi(\mathbf{x}_0, [t_0, t])$, Equation (2.60) becomes

$$\frac{d}{dt}\Phi(\mathbf{x}_0, t) = \left[\frac{\partial f}{\partial \mathbf{x}} \right] \Phi(\mathbf{x}_0, t), \quad \Phi(\mathbf{x}_0, t_0) = \mathbf{I}, \quad (2.61)$$

which is called the variational equation, a matrix-valued time-varying linear differential equation that gives the linearization of the vector field along the trajectory $\phi(\mathbf{x}_0, [t_0, t])$.

The matrix $\Phi(\mathbf{x}_0, t)$, called the state transition matrix or the Jacobian of the flow, is the derivative of the flow generated by the vector field of the PCR3BP with respect to initial conditions [15, 16].

The state transition matrix evaluated after a period T of the orbit gives the stability of a Lyapunov orbit and is called the Monodromy matrix, \mathbf{M} , given by

$$\mathbf{M} = \Phi(\mathbf{x}_0, T) = \frac{\partial}{\partial \mathbf{x}_0}\phi(\mathbf{x}_0, [t_0 = 0, T]). \quad (2.62)$$

The mirror image theorem [17] states that the PCR3BP presents the symmetry

$$S : (x, y, \dot{x}, \dot{y}, t) = (x, -y, -\dot{x}, \dot{y}, -t).$$

Thus, if a trajectory crosses the plane $y = 0$ perpendicularly ($\dot{x} = 0$) twice, it is a symmetric periodic orbit. Given the symmetry S and the matrices

$$\mathbf{S} = \begin{bmatrix} 1 & 0 & 0 & 0 \\ 0 & -1 & 0 & 0 \\ 0 & 0 & -1 & 0 \\ 0 & 0 & 0 & 1 \end{bmatrix} \quad \text{and} \quad \mathbf{J} = \begin{bmatrix} 0 & 0 & 1 & 0 \\ 0 & 0 & 0 & 1 \\ -1 & 0 & 0 & 2 \\ 0 & -1 & -2 & 0 \end{bmatrix}, \quad (2.63)$$

we have that

$$\Phi(\mathbf{x}_0, T) = \mathbf{S}\mathbf{J}\Phi^T(\mathbf{x}_0, t_{1/2})\mathbf{J}^{-1}\mathbf{S}\Phi(\mathbf{x}_0, t_{1/2}). \quad (2.64)$$

So, a symmetric periodic orbit can be determined by its half orbit. For the Lyapunov orbits, this means that the Monodromy matrix \mathbf{M} can be calculated knowing the state transition matrix at $t_{1/2} = T/2$.

For the Lyapunov orbits, the matrix \mathbf{M} has a pair of complex eigenvalues, ζ_1 and ζ_2 , associated to the central manifold and a real pair of eigenvalues, ζ_3 and ζ_4 , with $\zeta_3 < 1$, $\zeta_4 > 1$, and $\zeta_3\zeta_4 = 1$, associated to stable and unstable manifolds, respectively.

Let Γ be a Lyapunov orbit. The stable manifold tangent to the subspace spanned by the eigenvector associated to ζ_3 and the unstable manifold tangent to the subspace spanned by the eigenvector associated to ζ_4 are defined by

$$\begin{aligned} W^s(\Gamma) &= \{\mathbf{x} \in \mathbb{R}^4 : \phi(\mathbf{x}, t) \rightarrow \Gamma \text{ when } t \rightarrow \infty\}, \\ W^u(\Gamma) &= \{\mathbf{x} \in \mathbb{R}^4 : \phi(\mathbf{x}, t) \rightarrow \Gamma \text{ when } t \rightarrow -\infty\}. \end{aligned} \quad (2.65)$$

The unstable and stable invariant manifolds, W^s and W^u , whose projections onto the x - y plane are shown in Figure 2.5(b), are locally homeomorphic to two-dimensional cylinders and act as separatrices of the energy shell.

2.5 Geometry of the Solutions Near the Collinear Equilibria

C.C. Conley verified the applicability of the Lyapunov-Moser Theorem¹ for the PCR3BP and studied the geometry of the solutions near the collinear equilibrium points L_k , $k = 1, 2, 3$ [18, 19, 20].

In order to take advantage of the Hamiltonian character of the equations, following

¹Appendix D.

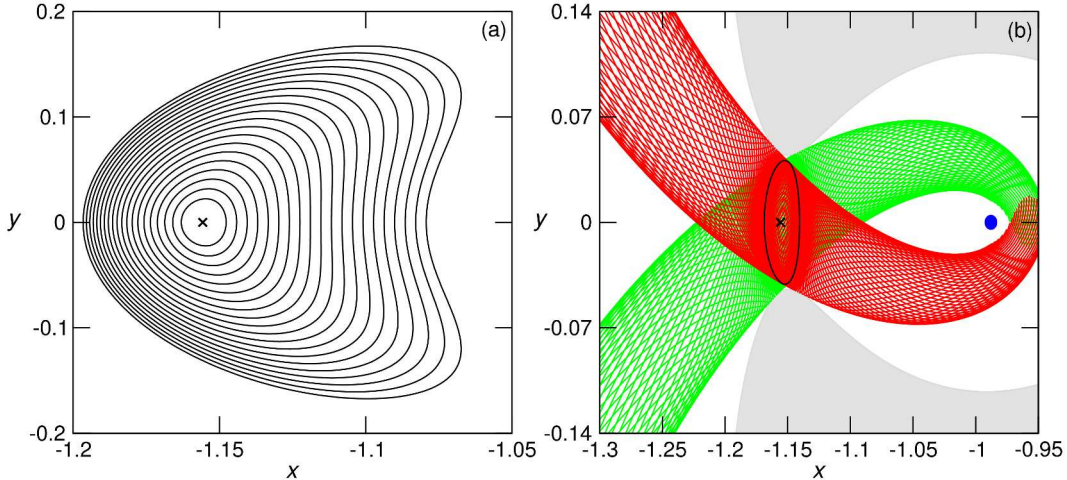


FIGURE 2.5 – (a) Projection onto the x - y plane of Lyapunov orbits around the Lagrangian point L_2 (black cross) for several energy levels of the Earth-Moon system. (b) Projection onto the x - y plane of the stable (green) and the unstable (red) manifolds of the Lyapunov orbit (black curve) for $C = 3.17978834$ around L_2 (black cross) of the Earth-Moon system. The Moon is depicted as a blue ball and the grey areas correspond to the forbidden regions.

Ref. [13], we rewrite Equation (2.20) in Hamiltonian form as

$$\begin{aligned}\dot{x} &= \frac{\partial H}{\partial p_x} = p_x + y, \\ \dot{y} &= \frac{\partial H}{\partial p_y} = p_y - x, \\ \dot{p}_x &= -\frac{\partial H}{\partial x} = p_y - x + \Omega_x, \\ \dot{p}_y &= -\frac{\partial H}{\partial y} = -p_x - y + \Omega_y,\end{aligned}\tag{2.66}$$

with the Hamiltonian function

$$H = \frac{1}{2} [(p_x + y)^2 + (p_y - x)^2] - \frac{x^2 + y^2}{2} - \frac{(1 - \mu)}{r_1} - \frac{\mu}{r_2} - \frac{\mu(1 - \mu)}{2},\tag{2.67}$$

where p_x and p_y are the conjugate momenta.

Let $(x_e, y_e, \dot{x}_e, \dot{y}_e) = (x_e, 0, 0, 0)$ be the coordinates of a generic collinear libration point L . In order to obtain the linearized equations of the system, we need to expand Equation (2.67) about $(x_e, y_e, p_{x_e}, p_{y_e}) = (x_e, 0, 0, 0)$. Introducing a coordinate transformation

that takes $(x_e, 0, 0, 0)$ to the origin, we obtain the Hamiltonian function for the linearized equations

$$H_l = \frac{1}{2} [(p_x + y)^2 + (p_y - x)^2 - ax^2 + by^2], \quad (2.68)$$

where a and b are positive constants defined by $a = 2\rho + 1$ and $b = \rho - 1$, and

$$\rho = \mu|x_e + 1 - \mu|^{-3} + (1 - \mu)|x_e - \mu|^{-3}. \quad (2.69)$$

The linearized equations in Hamiltonian form are

$$\begin{aligned} \dot{x} &= \frac{\partial H_l}{\partial p_x} = p_x + y, \\ \dot{y} &= \frac{\partial H_l}{\partial p_y} = p_y - x, \\ \dot{p}_x &= -\frac{\partial H_l}{\partial x} = p_y - x + ax, \\ \dot{p}_y &= -\frac{\partial H_l}{\partial y} = -p_x - y - by. \end{aligned} \quad (2.70)$$

The inverse Legendre transformation is introduced, rendering variables with a simpler geometrical meaning:

$$v_x = p_x + y \quad \text{and} \quad v_y = p_y - x, \quad (2.71)$$

with v_x and v_y corresponding to the particle's velocity in the rotating coordinate system.

Equations (2.70) become

$$\begin{aligned} \dot{x} &= v_x, \\ \dot{y} &= v_y, \\ \dot{v}_x &= 2v_y + ax, \\ \dot{v}_y &= -2v_x - by, \end{aligned} \quad (2.72)$$

and the energy integral H_l of Equation (2.68) is given by,

$$E_l = \frac{1}{2} [v_x^2 + v_y^2 - ax^2 + by^2]. \quad (2.73)$$

$E_l = \varepsilon = 0$ corresponds to the energy surface which passes through the libration point, and a neck around the libration point exists for $\varepsilon > 0$.

The eigenvalues of the linear system of Equation (2.72) are given by $\pm\lambda$ and $\pm i\tau$, with λ and τ positive real constants, so that the collinear equilibria are saddle-center type. The corresponding eigenvectors are

$$\begin{aligned} u_1 &= (1, -\sigma_1, \lambda, -\sigma_1\lambda), \\ u_2 &= (1, \sigma_1, -\lambda, -\sigma_1\lambda), \\ w_1 &= (1, -i\sigma_2, i\tau, \sigma_2\tau), \\ w_2 &= (1, i\sigma_2, -i\tau, \sigma_2\tau), \end{aligned} \quad (2.74)$$

where σ_1 and σ_2 are real constants.

A linear transformation is introduced such that the eigenvectors become the axes of the new coordinate system and the linearized equations take a simpler form:

$$\begin{aligned} \dot{\xi} &= \lambda\xi, \\ \dot{\eta} &= -\lambda\eta, \\ \dot{\gamma}_1 &= \tau\gamma_2, \\ \dot{\gamma}_2 &= -\tau\gamma_1, \end{aligned} \quad (2.75)$$

where $\gamma = \gamma_1 + i\gamma_2$. The energy function becomes

$$E_l = \lambda\xi\eta + \frac{\tau}{2} (\gamma_1^2 + \gamma_2^2). \quad (2.76)$$

The solutions of the linearized system given by Equation (2.75) can be written as

$$\begin{aligned} \xi(t) &= \xi^\circ \exp [\lambda t], \quad \eta(t) = \eta^\circ \exp [-\lambda t], \\ \gamma(t) &= \gamma_1(t) + i\gamma_2(t) = \gamma^\circ \exp [-i\tau t], \end{aligned} \quad (2.77)$$

where the constants $\xi^\circ, \eta^\circ, \gamma^\circ = \gamma_1^\circ + i\gamma_2^\circ$ are the initial conditions.

Besides the energy integral given by Equation (2.76), the system of Equation (2.75) admits another two constants of the motion, namely, functions $\xi\eta$ and $|\gamma|^2 = \gamma_1^2 + \gamma_2^2$.

There exists a region \mathcal{R} determined by a fixed energy surface $E_l = \varepsilon$ and $|\eta - \xi| \leq c$, which is homeomorphic to the product of a two-sphere crossed with the real line. The projection of \mathcal{R} onto the position space is denoted by R . Given a fixed positive ε , with an additional coordinate transformation of the form

$$\begin{aligned} \xi &= r + s, \\ \eta &= r - s, \end{aligned} \quad (2.78)$$

leading to

$$\begin{aligned} \xi - \eta &= 2s, \\ \xi\eta &= r^2 - s^2, \end{aligned} \quad (2.79)$$

we can see that a bi-ellipsoid is defined for each value of $s \in [-c, c]$ by

$$\varepsilon + \lambda s^2 = \lambda r^2 + \frac{\tau}{2} (\gamma_1^2 + \gamma_2^2), \quad (2.80)$$

and the two-spheres that bound the \mathcal{R} region correspond to $\xi - \eta = -c$ and $\xi - \eta = +c$.

Conley proved that for sufficiently small positive values of c and ε , the \mathcal{R} region is inside a closed ball B , which corresponds to a region in which all the power series of the Lyapunov-Moser Theorem converge. Moreover, in the ball B , these series as well as their first partial derivatives are dominated by the lower order terms. The region around L_k for $C \lesssim C_k$, $k = 1, 2, 3$, was called a neck region by Conley, who proved the existence of transit orbits through that neck.

Given the linearly independent solutions (Equation (2.77)), the general solution of the linear system can be expressed as

$$u(t) = \alpha_u u_1 \exp[\lambda t] + \alpha_s u_2 \exp[-\lambda t] + 2\mathbf{Re} \{ \beta w_1 \exp[i\tau t] \}, \quad (2.81)$$

where the arbitrary constants α_u and α_s are real and β is complex.

The real constants α_u and α_s define three possible signs $(+, 0, -)$ for $\xi(t)$ and $\eta(t)$. The combination of these three possibilities results in nine different classes of solutions in the energy shell.

To classify the solutions, one must observe the asymptotic behavior of $x(t)$ as $t \rightarrow \pm\infty$. When $t \rightarrow \infty$, $x \rightarrow -\infty$ if $\alpha_u < 0$; x is limited if $\alpha_u = 0$; and $x \rightarrow \infty$ if $\alpha_u > 0$. The same is valid when $t \rightarrow -\infty$ using α_s instead of α_u .

If x remains limited as $t \rightarrow \pm\infty$, the trajectory corresponds to a periodic solution given by $\alpha_u = \alpha_s = 0$. Therefore, the nine classes of orbits can be classified into four

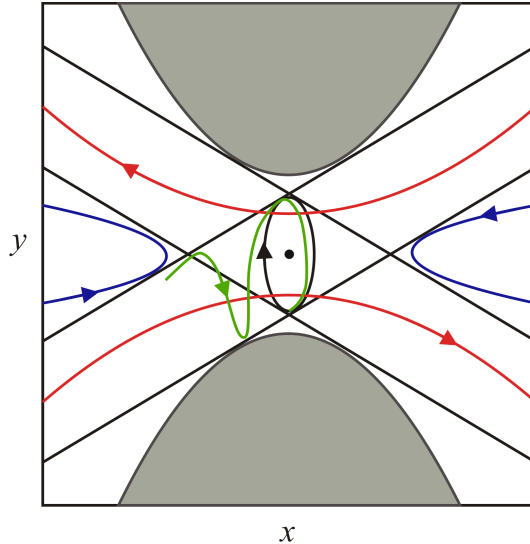


FIGURE 2.6 – The four categories of orbits are shown in the x - y projection R of the neck region \mathcal{R} around a generic collinear equilibrium point L . The periodic orbit is the black curve around the black point that represents L . The transit, nontransit and asymptotic orbits are depicted by the red, blue and green curves, respectively.

categories or types of motion (see Figure 2.6):

1. **Asymptotic orbits**, $\alpha_u = 0$ or $\alpha_s = 0$ and $\alpha_u \neq \alpha_s$ (four classes of orbits).
2. **Transit orbits**, $\alpha_u \alpha_s < 0$ (two classes of orbits).
3. **Non-transit orbits**, $\alpha_u \alpha_s > 0$ (two classes of orbits).
4. **Periodic orbits**, $\alpha_u = \alpha_s = 0$ (one class of orbits).

Let $\Delta = (n_1, n_2)$ be the ordered pair of signs of α_u and α_s , respectively. The four classes of asymptotic orbits are related to two pairs of invariant tubes which depart from the periodic orbit. The pair with $\Delta = (+, 0)$ and $(-, 0)$ is associated to the stable set W^s , while the pair with $\Delta = (0, +)$ and $(0, -)$ is associated to the unstable set W^u . As already mentioned, these tubes are topologically equivalent to two-dimensional cylinders, and the orbits which rest on them are spirals.

The two classes of transit orbits, correspond to the pairs of signs $\Delta = (-, +)$ and $\Delta = (+, -)$. The first pair correspond to transit orbits which pass through the periodic

orbit from the left to the right, while the second pair corresponds to transit orbits which pass through the periodic orbit from the right to the left. For the non-transit orbits, there is a class of orbits confined at the left side of R , corresponding to $\Delta = (-, -)$, and a class of orbits confined at the right side of R , corresponding to $\Delta = (+, +)$.

Finally, the pair of signs $\Delta = (0, 0)$ corresponds to the periodic orbits. The set of periodic solutions associated to each collinear Lagrangian point constitutes the biparametric (C, μ) family of Lyapunov orbits around that equilibrium.

The two-dimensional stable and unstable manifolds, W^s and W^u , associated to the Lyapunov orbits separate transit and non-transit solutions in the three-dimensional energy shell immersed in the four-dimensional phase space, in such a way that, the transit trajectories are inside the tubes and the non-transit trajectories are outside the tubes.

Conley [19] outlined a scheme to design low energy “periodic” Earth-to-Moon transfers, according to the following criteria:

“(i) the cost per cycle should be as small as is practical; (ii) control and stability problems should be as easy as possible; (iii) as much flexibility should be build into the scheme as possible.”

The author argued that the first criterion could be satisfied by orbits with a Jacobi constant value only slightly less than C_1 , the Jacobi constant value of the critical point between the Earth and the Moon. Some of the possible objections to that choice are the length of time required to complete a cycle and the extreme sensitive dependence on the initial conditions so that small variations could imply in orbits of distinct classes. On the other hand, one could take advantage of this sensitive behavior to satisfy the second and the third criteria listed above.

3 Weak Stability Boundaries

In the context of low energy Earth-to-Moon transfers, the Weak Stability Boundary concept was proposed by E. Belbruno in the late 80's as an initiative to establish practical stable regions related to temporary capture orbits around the Moon. In this approach, the gravitational effects of the Earth, the Moon, and the Sun are considered when modeling the motion of the spacecraft.

Specifically, as originally proposed by E. Belbruno, the WSB is related to a special type of capture by the Moon called *ballistic capture*. Thus, the mathematical model considered for the proposition of the WSB is the PCR3BP which describes the dynamics of the spacecraft under the gravitational influence of the Earth-Moon subsystem of the full Sun-Earth-Moon system.

Organization of the Chapter: In Section 3.1, we present a brief discussion of capture in the PCR3BP. In Section 3.2, three different approaches to obtain weakly stable regions are described. Also, the WSB algorithmic definition and the WSB analytical approximation are presented. In Section 3.3, we discuss the presented definitions and make some remarks that will guide the investigation of Chapters 5 and 6.

3.1 Capture in the PCR3BP

Let $\mathbf{q} = (x, y) \in \mathbb{R}^2$ be the position vector of P_3 . In general, a capture state of P_3 is defined when P_3 is somehow geometrically *bounded* to P_1 and (or) P_2 . Following Ref. [7], we state the definitions of some relevant types of capture.

Definition 1 (Permanent capture). *P_3 is permanently captured into the P_1 - P_2 system in forward time if $|\mathbf{q}|$ is bounded as $t \rightarrow \infty$, and $|\mathbf{q}| \rightarrow \infty$ as $t \rightarrow -\infty$. P_3 is permanently captured in backward time if $|\mathbf{q}|$ is bounded as $t \rightarrow -\infty$, and $|\mathbf{q}| \rightarrow \infty$ as $t \rightarrow \infty$.*

For the General Problem of Three Bodies, it was proved by J. Chazy that the set of initial values leading to permanent capture comprises a set of measure zero. The existence of such orbits was later shown by V.M. Alekseev. For further discussion we refer the reader to Ref. [21].

Definition 2 (Temporary capture). *P_3 has temporary capture at $t = t^*$, $|t^*| < \infty$, if $|q(t^*)| < \infty$ and $\lim_{t \rightarrow \pm\infty} |q(t)| = \infty$.*

The temporary capture state implies the ejection of the particle as $t \rightarrow \pm\infty$, that is, P_3 is neither permanently captured nor describes an unbounded oscillatory orbit.

Definition 2 can be modified to *finite temporary capture* considering that P_3 achieves a prescribed finite distance $|q(t)| = d > 0$ from P_2 , for instance, at time t^* . In this case, the time interval $\Delta t = |t^* - T^*|$ represents the duration of the capture relative to a reference time T^* . This definition measures the interval of time that P_3 remains within a given neighborhood of P_2 .

The ballistic capture is an alternative type of capture said to be defined analytically in order to be distinguished from the previously geometrically defined types of capture.

According to Ref. [7], this analytical definition of capture makes use of the Keplerian (two-body) energy of P_3 with respect to P_2 , given by

$$h_K = \frac{1}{2} (\dot{\tilde{x}}^2 + \dot{\tilde{y}}^2) - \frac{Gm_2}{\tilde{r}_2}, \quad (3.1)$$

where $(\tilde{x}, \tilde{y}, \dot{\tilde{x}}, \dot{\tilde{y}})$ is the state of P_3 in an inertial reference frame with origin in P_2 , $\tilde{r}_2 = \sqrt{\tilde{x}^2 + \tilde{y}^2}$ is the distance between P_3 and P_2 , m_2 is the mass of the primary and G stands for the universal gravitational constant [22].

Definition 3 (Ballistic capture). P_3 is ballistically captured by P_2 at time $t = t_c$ if, for a solution $\varphi(t) = (x(t), y(t), \dot{x}(t), \dot{y}(t))$ of the R3BP,

$$h_K(\varphi(t_c)) \leq 0.$$

We note that Definition 3 is not unique. In Ref. [5], for example, ballistic capture by the Moon refers to an orbit which, under natural dynamics of the R3BP, gets within a 20,000 km radius region around the Moon and performs at least one revolution around that primary. In general, the idea behind the ballistic capture is a situation in which no propulsion ($\Delta V = 0$) is necessary to achieve a “temporary” capture orbit around the destination body [23].

Although the Kepler energy h_K is not an invariant for the PCR3BP dynamics, it is used as an indicator of ballistic capture state in Definition 3 in analogy with the characteristic bounded and unbounded conic solutions of the two-body problem. As known, in the Kepler problem, h_K is constant at all points of the orbit and depends only on the semi-major axis a . For all closed orbits (ellipses or circles), h_K is negative; for the limiting case of parabolic orbits with $a = \infty$, h_K equals zero; and for the case when the solutions of

the Kepler equation are unbounded (hyperbolas), h_K is positive [24].

3.2 Approaches to Obtain Weakly Stable Regions

The identification of weak stability regions in the phase space was meant to be associated to the ballistic capture state given by Definition 3 in order to reduce or, ideally, eliminate the hyperbolic excess velocity at lunar periapsis upon arrival. Since the concept was first introduced, several approaches were proposed aiming to identify such regions and provide feasible mission solutions. In the context of low energy Earth-to-Moon transfers, at least three different definitions share the WSB terminology.

Iterative approach:

The first definition refers to the so called WSB or fuzzy boundary region, a qualitative region where the gravitational forces of the Sun, the Earth, and the Moon cancel each other. In configuration space, this region is located at approximately 1.5 million km away from the Earth in the Sun-Earth direction [1, 3, 6].

In this approach, the constructive method is usually based on four body models. Starting from the final selenocentric orbit with prescribed orbital parameters $(\Omega_M, i_M, \omega_M)$, periselenium height, and arrival time, the selenocentric eccentricity e_M is adjusted iteratively in order to obtain an adequate apogee in the WSB region that matches a geocentric orbit with a specified perigee height.

In the general case, this method provides tri-impulsive maneuvers that are somehow similar to bi-elliptic transfers. The maneuvers are required to (i) leave the Earth parking orbit, (ii) adjust the positions and the velocities at the WSB region, and (iii) stabilize the spacecraft into the final selenocentric orbit. Then, the obtained preliminary solution is used as an initial guess for optimization methods in order to reduce the total ΔV .

However, transfer trajectories with no intermediate maneuver can be found depending on factors such as arrival time, the Sun-Earth-Moon configuration, and the assigned periselenium direction. Take, for example, the transfers obtained by C. Circi and P. Teofilatto in Ref. [6] where the Sun-Earth-Moon system is modeled by a JPL ephemeris model and a backwards propagation method is used.

Algorithmic construction:

The second definition relies on a constructive algorithm based on the dynamical evolution of specific sets of initial conditions around the Moon under the Earth-Moon system PCR3BP dynamics and their classification according to certain stability criteria [3, 7, 8]. This WSB algorithmic definition has been numerically rebuilt and specific applications and analyses have been considered by some authors [10, 11, 25].

The current numerical algorithmic definition is stated by E. Belbruno in Ref. [7] (Chapter 3.2.1) and the construction procedure was reviewed and extended by F. García and G. Gómez [8].

Let $l(\theta)$ be the radial segment connecting the positions of P_2 and P_3 , where θ is the counterclockwise angle measured from the x -axis, for $x > -1 + \mu$, to $l(\theta)$. Sets of initial conditions are constructed for which P_3 is assumed to start its motion on the periapsis of an osculating ellipse around P_2 with the magnitude of the sidereal initial velocity, ν , given by

$$\nu^2 = \frac{\mu(1+e)}{r_2}, \quad (3.2)$$

where e is the eccentricity of the osculating ellipse. The initial Kepler energy of P_3 with respect to P_2 is negative for $e \in [0, 1)$ since the two-body energy computed at the periapsis is $h_K = \mu(e-1)/2r_2$ [22].

For a fixed position on $l(\theta)$, prograde osculating motions about P_2 are generated by initial conditions with positive velocity, i.e., counterclockwise sense, given by

$$\begin{aligned} x &= -1 + \mu + r_2 \cos \theta, & y &= r_2 \sin \theta, \\ \dot{x} &= r_2 \sin \theta - \nu \sin \theta, & \dot{y} &= -r_2 \cos \theta + \nu \cos \theta, \end{aligned} \tag{3.3}$$

while retrograde osculating motions about P_2 are generated by initial conditions with negative velocity, i.e., clockwise sense, given by

$$\begin{aligned} x &= -1 + \mu + r_2 \cos \theta, & y &= r_2 \sin \theta, \\ \dot{x} &= r_2 \sin \theta + \nu \sin \theta, & \dot{y} &= -r_2 \cos \theta - \nu \cos \theta. \end{aligned} \tag{3.4}$$

For the trajectories generated by these initial conditions, the following definition of stable behavior is given [7].

Definition 4 (Stability). *The motion of a particle under the PCR3BP dynamics is said to be **stable** about P_2 if after leaving $l(\theta)$ it makes a full cycle about P_2 without going around P_1 and returns to $l(\theta)$ at a point with negative Kepler energy with respect to P_2 . Otherwise, the motion will be **unstable**. (See Figure 3.1.)*

This stability classification associated to the ballistic capture of Definition 3 generates stable and unstable subsets and leads to the definition of regions in phase space known as boundaries of stability.

Definition 5 (Algorithmic WSB). *The Weak Stability Boundary is given by the set*

$$\partial\mathcal{W} = \{r^*|\theta \in [0, 2\pi), e \in [0, 1)\}, \tag{3.5}$$

where $r^*(\theta, e)$ are the points along the radial line $l(\theta)$ for which there is a change of

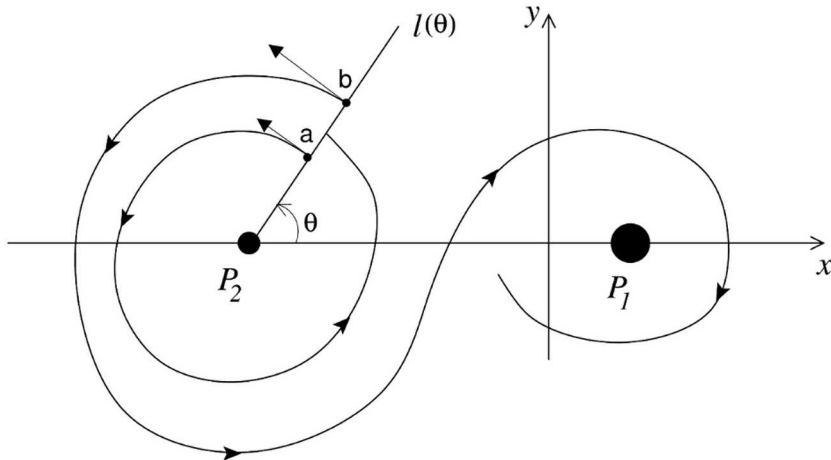


FIGURE 3.1 – Schematic representation of the definition of stable and unstable trajectories, indicated by a and b , respectively.

stability in the sense of Definition 4. The subset obtained by fixing the eccentricity e of the osculating ellipse is

$$\partial\mathcal{W}^e = \{r^*|\theta \in [0, 2\pi), e = \text{constant}\}. \quad (3.6)$$

In this approach, it is implicit that the initial conditions of the algorithmic definition correspond to states which are candidate solutions for the final portion of a transfer trajectory which ideally must correspond to a ballistic capture orbit. Thereby, a circularization maneuver can be applied both at the beginning or at the end of the turn around P_2 .

Definition 4 is readily extended for n revolutions of P_3 about P_2 without going around P_1 , so that the set of points along the radial line $l(\theta)$ for which there is a change of stability after n revolutions gives the n -WSB $\partial\mathcal{W}_n$ [8].

Analytical approximation:

The third definition constitutes an analytical approximation constructed by the intersection of three subsets of the phase space [7, 9].

Let (x, y, \dot{x}, \dot{y}) be the state of P_3 in the synodic reference frame and $J(x, y, \dot{x}, \dot{y})$ be the

integral of Jacobi (Equation (2.25)). Consider the sets

$$J^{-1}(C) = \{(x, y, \dot{x}, \dot{y}) | J(x, y, \dot{x}, \dot{y}) = C\}, \quad (3.7)$$

$$\Sigma = \{(x, y, \dot{x}, \dot{y}) | h_K(x, y, \dot{x}, \dot{y}) \leq 0\}, \quad (3.8)$$

$$\sigma = \{(x, y, \dot{x}, \dot{y}) | \dot{r}_2 = 0\}, \quad (3.9)$$

where \dot{r}_2 is the radial velocity of P_3 relative to P_2 , so that σ is the set of points corresponding to local periapsis or apoapsis of osculating ellipses.

Definition 6 (WSB analytically defined).

$$\partial W = J^{-1}(C) \cap \Sigma \cap \sigma, \quad (3.10)$$

associated to a certain value of the Jacobi constant C , with $C < C_1$, is called the Weak Stability Boundary, a set where ballistic capture occurs in the R3BP.

Equation (2.25) can be rewritten as a function of r_2 , θ , and e , as

$$C(r_2, \theta, e) = (1 - \mu) + \frac{2\mu}{r} - 2(1 - \mu)r \cos(\theta) + r^2 + \frac{2(1 - \mu)}{\sqrt{1 - 2r \cos(\theta) + r^2}} - (r \mp \nu)^2, \quad (3.11)$$

where the - sign accounts for initial conditions with positive initial velocity, while the + sign accounts for initial conditions with negative initial velocity, and ν is given by Equation (3.2). Since we are considering a fixed value for μ , the dependence on this parameter is suppressed.

Alternatively, we must have $C \in [C^*, C_2)$ if only external ballistic capture is to be considered. The upper bound of C is needed in order to assure that there exist transit

orbits through that neck region around L_k . Belbruno argues that the value of C^* can be estimated graphically for each μ so that ∂W exists.

3.3 Comments on the Presented Definitions

A few remarks are to be made concerning the previously presented definitions of capture and the association of that concept with the determination of effective or practical stable regions in the phase space.

In Definitions 1 and 2, it is usual to include a geometric limit for capture, motivated by the existence of a region around a primary called the Sphere of Influence (SOI)¹. In this region it is convenient to assume that P_3 and that primary constitute a two-body problem, considering the gravitational influence of other massive bodies as perturbations [26].

Unlike Definitions 1 and 2, the capture state given by Definition 3 is indicated exclusively by the real quantity h_K , neglecting the natural geometric limit imposed by the SOI. We will see examples in the Earth-Moon-sc system (Chapters 5 and 6) in which, although the Kepler energy of P_3 with respect to P_2 is negative outside the lunar SOI, if an impulsive maneuver is applied aiming to obtain a final circular or elliptic orbit around P_2 , that orbit will be unstable due to the action of other forces acting upon P_3 besides the gravitational influence of P_2 .

The WSB analytical approximation of Definition 6 is given as the intersection of three subsets of the phase space, so the dimension of ∂W is restricted by the conditions expressed in the construction of these subsets. The construction of this analytical approximation of the WSB depends on the value of the Jacobi constant C , that is, ∂W is built on an energy shell in such a way that the set $J^{-1}(C)$ constitutes a three-dimensional surface

¹Appendix B.

immersed in the four-dimensional phase space, which reduces in one unit the dimension of the phase space. The set σ of phase space states with null radial velocity also reduces in one unit the dimension of the phase space. Thus, the maximum dimension of $\partial\mathcal{W}$ is 2.

On the other hand, the algorithmic construction of $\partial\mathcal{W}$ is based on the dynamical evolution of sets of initial conditions and their subclassification according to a certain stability criterion. These specific sets of initial conditions are generated for fixed e , and for each $\partial\mathcal{W}^e$ obtained, no restriction is imposed for the value of the Jacobi constant C that varies freely over the sets. The fractal dimension of $\partial\mathcal{W}$ is expected to be between 2 and 3 and numerical experiments suggest that this set is the reminiscent of a Cantor set [9]. For a given $\partial\mathcal{W}^e$, the fractal dimension is expected to be one unit less than the dimension of $\partial\mathcal{W}$.

The stable sets obtained by keeping constant e or C are fundamentally different. Therefore, the algorithmic definition and the analytical approximation imply in distinct topologies for the WSB [27].

To obtain low energy Earth-to-Moon transfers, among other aspects, one must seek transfer orbits that minimize the ΔV for the stabilization of the spacecraft into a prescribed final orbit around the Moon. Therefore, both the definition of ballistic capture and the determination of weak stability regions in the phase space where that kind of capture occurs should be connected to the identification of such orbits. The investigation performed in this work is guided by this premise in order to characterize the algorithmic WSB, to verify its applicability and the consistency of its constructive procedure.

For space mission design, it is implicit that the initial conditions of the algorithmic definition correspond to states which are candidate solutions for the final portion of a transfer trajectory which ideally must correspond to a ballistic capture orbit. Thereby, a

circularization maneuver can be applied both at the beginning or at the end of the turn around P_2 .

4 Patched Three-Body Approach

In Chapter 2, we mentioned that C.C. Conley outlined a scheme to design low energy Earth-to-Moon transfers. In his preliminary model, only two primaries, namely, the Earth and the Moon, were taken into account when modeling the motion of the spacecraft. This simple preliminary model is suited mostly for trajectories through the L_1 neck region. Throughout this text, the transfers generated by such orbits are called *direct inner transfers*. Particularly, Earth-to-Moon inner transfers, using both the R3BP and a Sun perturbed version of that problem, have been obtained by K. Yagasaki [28, 29] with durations ranging from 4 to 44 days. Also, optimal LEO-to-LLO (Low Earth Orbit to Low Lunar Orbit) trajectories with duration of 4.5 days were obtained by A. Miele and S. Mancuso [30] using a simplified version of the R3BP. These transfers have costs comparable to or lower than traditional Hohmann transfers, which have a duration of approximately 4 to 5 days.

However, one needs to consider the Sun-Earth-Moon-sc four-body dynamics in order to design Earth-to-Moon trajectories which take considerable advantage of the Sun's gravity to lower the total energy cost. Originally, the method of construction of such transfer trajectories was associated to the WSB or fuzzy boundary region and consisted in: (i) performing an impulsive maneuver to leave the Earth parking orbit and integrating forwards in time up to the WSB region; (ii) integrating backwards in time from the Moon target orbit up to the WSB region; and (iii) adjusting the positions and velocities of the

two portions by means of an impulsive maneuver. The solution obtained through this method is used as an initial guess for optimization methods in order to reduce the total ΔV . The rescue of the Japanese Hiten mission to the Moon was based on this WSB strategy. Throughout this text, the Hiten-like transfer orbits are called *external transfers*.

Alternatively, external transfers can be obtained considering the *patched three-body approach* presented by W.S. Koon, *et al.* [4, 5]. This model approximates the Sun-Earth-Moon-sc four-body system as two coupled three-body systems: Sun-Earth-sc (SE-system) and Earth-Moon-sc (EM-system). As an initial approach, each restricted three body system is modeled by a PCR3BP. The construction of transfer orbits is based on the transport channels provided by the invariant manifolds associated to unstable periodic orbits around the collinear Lagrangian points of these two subsystems. Usually, these solutions are associated with long flight time, i.e., over 100 days. The solutions obtained from these two three-body problems are then used as an initial guess for a numerical procedure that converges to a full four-body solution. In this approximation, the EM portion of the trajectory is related to the ballistic part of the complete four-body orbit.

This Chapter is dedicated to the patched three-body approach, given that the understanding of the patching mechanism is fundamental to guide future investigations concerning the accomplishment of ballistic capture by the Moon in the final portion of Earth-to-Moon transfer trajectories, considering the EM-system.

Organization of the Chapter: In Section 4.1, we review the general mechanism of construction of transfer trajectories in the patched three-body approach and present our particular patching procedure. Following, in Section 4.2, we explore some dynamical features of the mechanism. In the EM-system we focus on how to determine initial spatial configurations of the primaries that provide feasible transfers. In the SE-system we define

specific sets of initial conditions around the Earth and characterize the trajectories in order to determine transfer trajectories corresponding to better project specifications. Finally, Section 4.3 is devoted to the discussion of the results of the presented analyses.

4.1 Mechanism of Construction

The main idea behind the patched three-body approach is that a preliminary approximated orbit, \mathbf{o}_c , departing from and arriving at prescribed geocentric and selenocentric orbits, \mathbf{o}_i and \mathbf{o}_f , respectively, can be decomposed into a nontransit orbit, \mathbf{o}_n , associated to a Lyapunov orbit around L_1 or L_2 of the SE-system and a transit orbit, \mathbf{o}_t , associated to a Lyapunov orbit around L_2 of the EM-system. For the effectiveness of this approach, the configuration of the considered four bodies must allow that the invariant manifold structures of the two three-body systems intersect each other within a reasonable time. The patching procedure consists in performing an impulsive maneuver to match the energy levels of both systems at an adequate Poincaré section, usually defined in the SE rotating frame along a line of constant x -position passing through the Earth, where the involved manifolds intersect each other. The stable invariant manifold tube of the Lyapunov orbit associated to L_2 of the EM-system provides the dynamical channel in phase space that enables ballistic capture of the spacecraft by the Moon. It is generally accepted that Hiten-like transfer trajectories are obtained through the described mechanism [4].

The total energy cost of such a transfer is given by the sum of three impulses: Δv_1 , needed to leave \mathbf{o}_i ; Δv_2 , needed to match the SE and the EM energy levels at the patching point; Δv_3 , needed to stabilize the spacecraft into the final orbit \mathbf{o}_f .

Some work has been done for systems other than EM and SE, in the case that the intersection between the manifolds is empty [31].

The development of this Section follows closely the results of Refs. [4, 5, 13]. Before proceeding, we will devote some time to develop the terminology we have adopted throughout this chapter. The SE and the EM systems are represented by \odot and \oplus , respectively. We denote the state of P_3 in the *SE* synodic normalized reference frame by the vector $\mathbf{X} = (X, Y, \dot{X}, \dot{Y})$, while the state of P_3 in the *EM* synodic normalized reference frame is given by $\mathbf{x} = (x, y, \dot{x}, \dot{y})$. Moreover, we adopt $P_0 \leftrightarrow$ Sun, $P_1 \leftrightarrow$ Earth, $P_2 \leftrightarrow$ Moon, and $P_3 \leftrightarrow$ spacecraft. In this work we are concerned only with the L_2 equilibrium of each system, namely, L_2^\odot for the SE-system and L_2^\oplus for the EM-system. The Lyapunov orbits associated to these equilibria are denoted Γ^\odot and Γ^\oplus , respectively, and their stable and unstable manifolds are W_\odot^s , W_\oplus^s , and W_\odot^u , W_\oplus^u , where we have suppressed the reference to the L_2 equilibrium in order to simplify the notation. The branches of the stable and unstable manifolds associated to Γ^\odot (Γ^\oplus) around L_2^\odot (L_2^\oplus) that go into the smaller primary realm are called inner branches, while the branches that extend to the exterior realm to the left of L_2^\odot (L_2^\oplus) are called outer branches.

With respect to an inertial reference frame, each of the two three-body systems rotates around its barycenter with distinct angular velocity, specifically, $\omega_\odot = 1.99095 \times 10^{-7}$ rad/s and $\omega_\oplus = 2.66170 \times 10^{-6}$ rad/s. As a result, the Moon describes a counterclockwise circular orbit around the Earth with an approximate period of 29.5 days. We define the angle α between the P_0 - P_1 axis and the P_1 - P_2 axis and call it the initial phase (of a time reverse integration departing from a neighborhood around the Moon). This angle gives the relative initial position of the Moon with respect to the X -axis of the SE synodic system. Because of the distinct barycenters and angular velocities, the patching procedure involves translations, rotations and rescaling transformations. For the sake of simplicity, we denote by Υ the sequence of geometrical transformations that maps

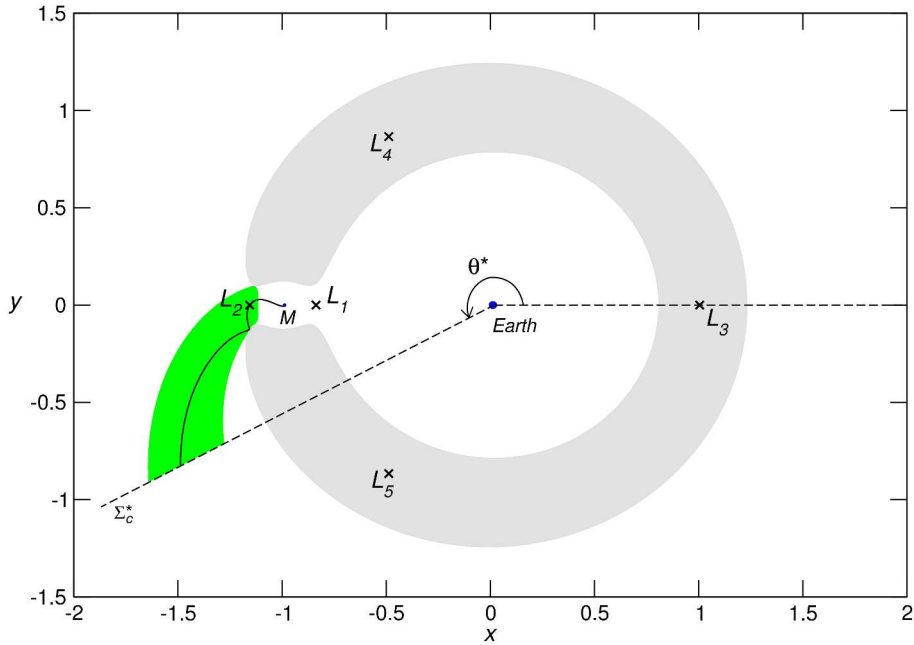


FIGURE 4.1 – Projection onto the x - y plane of \mathbf{o}_t , the EM portion of the complete transfer orbit \mathbf{o}_t . The projection of the outer branch of W_{\oplus}^s is shown in green and grey corresponds to the forbidden region for $C^{\oplus} = 3.16117289$. θ^* is the angle defined by the position of Σ_c at the patching instant.

a point \mathbf{x} in the EM synodic normalized reference frame onto a point \mathbf{X} in the SE synodic normalized reference frame.

Usually, the patching maneuver is performed at a Poincaré section Σ_c defined in the SE rotating frame as $X = X_{P_1} = -1 + \mu_{\odot}$, $\dot{X} > 0$, $Y < 0$. Let θ be the counterclockwise angle measured in the EM reference frame from the P_1 - P_2 axis, for $X > X_{P_1}$, to the patching plane Σ_c . Due to the relative rotation of the two three-body subsystems, the Σ_c plane, which is fixed in the SE reference frame, rotates around P_1 in the EM reference frame. Thus, $\theta(t)$ varies with the time. Considering a time reverse integration departing from a given final state around the Moon (initial condition of the retrograde integration), we have that $\theta(0) = \alpha + \pi/2$. Moreover, at the patching instant t_c , the angular position $\theta^* = \theta(t_c)$ defines the Σ_c^* in the EM reference frame. Figure 4.1 shows the x - y projection of \mathbf{o}_t , i.e., the EM portion of the complete transfer orbit \mathbf{o}_c , along with the outer branch of the W_{\oplus}^s .

The patched three-body construction begins by choosing a pair of Jacobi constant values, C^\odot for the SE-system and C^\oplus for the EM-system, such that $C^\odot < C_2^\odot$ and $C^\oplus < C_2^\oplus$, given that the neck region \mathcal{R} around L_2 of both systems must exist. These C values unequivocally determine the Lyapunov orbits around L_2^\odot and L_2^\oplus with their stable and unstable manifolds. Furthermore, the choice of C^\odot and C^\oplus must observe the following criteria: (i) the inner branch of W_\odot^s must come near the Earth, (ii) the outer branch of W_\oplus^s must intercept W_\odot^u in Σ_c , and (iii) the inner branch of W_\oplus^u must come near the Moon.

Figure 4.2 displays the Poincaré cut γ_1 at section Σ_c of the inner branch of W_\odot^u associated to Γ^\odot around L_2^\odot for $C^\odot = 3.00080369$. Also, we can see the Poincaré cuts γ_{2a} , γ_{2b} , and γ_{2c} , of the outer branch of W_\oplus^s associated to Γ^\oplus around L_2^\oplus for $C^\oplus = 3.16117289$ for three different phases α_a , α_b , and α_c . In the Σ_c section, the transfer orbit is a point $\mathbf{X}_c = (X_c = X_{P_1}, Y_c, \dot{X}_c, \dot{Y}_c)$ outside and near γ_1 and inside one of the three γ_2 curves. The representation of \mathbf{X}_c in the EM synodic reference frame is $\mathbf{x}_c = (x_c, y_c, \dot{x}_c, \dot{y}_c)$.

Ideally, in a costless patching, i.e., $\Delta v_2 = 0$, \mathbf{X}_c is a point with the following properties:

- (i) the direct ($t > 0$) integration of \mathbf{x}_c in the EM-system gives a trajectory that takes P_3 through the interior of W_\oplus^s and W_\oplus^u , so that the spacecraft is temporarily captured by the Moon;
- (ii) the reverse ($t < 0$) integration of \mathbf{X}_c in the SE-system gives a trajectory that, guided by W_\odot^u , approaches Γ^\odot , and then, guided by W_\odot^s , returns to the neighborhood of the Earth. However, the most general situation is the case at which an impulsive maneuver is needed to correct the energy at the patching point, as we will explain later on.

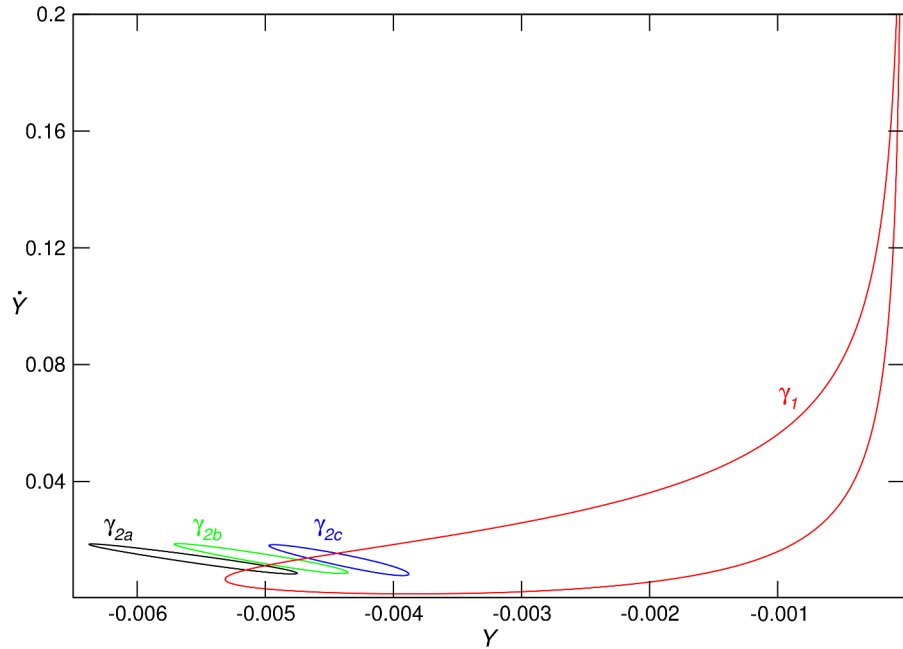


FIGURE 4.2 – The red curve γ_1 corresponds to the Poincaré cut at section Σ_c of the inner branch of W_\odot^u associated to Γ^\odot around L_2^\odot for $C^\odot = 3.00080369$. The black, green, and blue curves, γ_{2a} , γ_{2b} , and γ_{2c} , respectively, correspond to the cuts of the outer branch of W_\oplus^s associated to Γ^\oplus around L^\oplus for $C^\oplus = 3.16117289$ for three different phases α_a , α_b , and α_c .

4.1.1 Patching Procedure

To our knowledge, there isn't an unique or an optimized procedure to determine Earth-to-Moon trajectories in the patched three-body approach. The literature concerning this subject mostly presents the guidelines we have described so far, lacking an extensive analysis of the patching procedure. Also, very little is said about the details involved in the construction of effective transfer trajectories.

In this work, a complete transfer orbit \mathbf{o}_c , starting at a prescribed circular geocentric orbit \mathbf{o}_i and ending at a prescribed circular selenocentric orbit \mathbf{o}_f , was built as follows:

1. For the SE-system, we defined a Poincaré section Σ_e as $X = X_{P_1}$, $\dot{X} < 0$, and determined the intersection γ_0 of the inner branch of W_\odot^s with Σ_e for a given C^\odot .
2. We took a line segment η_0 outside and near the curve γ_0 in the Σ_e section, with

$Y = \text{constant}$, corresponding to the altitude of \mathbf{o}_i . Then, using $X = X_{P_1}$ and C^\odot , we determined $\dot{X} < 0$ for each of the (Y, \dot{Y}) points of the η_0 segment. This defines initial conditions that under forward integration map onto the η_1 curve in the Σ_c section, along the γ_1 cut of W_\odot^u (see Figure 4.3).

3. For the EM-system, we defined a Poincaré section Σ_m as $x = x_{P_2}$, $\dot{x} > 0$, and determined the intersection γ_3 of the inner branch of W_\oplus^u with Σ_m for a given C^\oplus .
4. We picked an initial condition inside curve γ_3 , with $y = \text{constant}$ corresponding to the prescribed altitude of \mathbf{o}_f , and integrated backwards ($t < 0$) until the trajectory crossed the Σ_c^* section, defined by an arbitrary θ^* , determining a \mathbf{x}_c state at Σ_c^* . By doing this for $0 \leq \theta^* < 2\pi$ and applying the geometrical transformation Υ for every \mathbf{x}_c state, we obtained the corresponding states in the Σ_c section (curve β of Figure 4.3).
5. Using a iterative bisection method we defined a point (Y_c, \dot{Y}_c) in the Σ_c plane. This point corresponds to the intersection of the curves η_1 and β .
6. Given $X_c = X_{P_1}$ and C^\odot , we computed $\dot{X}_c > 0$, completely defining the state $\mathbf{X}_c = (X_c, Y_c, \dot{X}_c, \dot{Y}_c)$ of the \mathbf{o}_n trajectory in the Σ_c section.
7. Applying the inverse transformation Υ^{-1} , we obtained $\mathbf{x}_c = (x_c, y_c, \dot{x}_c, \dot{y}_c)$, corresponding to \mathbf{X}_c in the EM reference frame. Usually, \mathbf{x}_c is not in the energy surface defined by the original C^\oplus . So, an impulsive maneuver Δv_2 is needed to correct the velocity \dot{x}_c . After the maneuver, the spacecraft lies at the C^\oplus energy surface, with its new state given by $\mathbf{x}'_c = (x_c, y_c, \dot{x}_c + \Delta v_2, \dot{y}_c)$.
8. We obtained \mathbf{o}_t integrating \mathbf{x}'_c forwards, under the EM-system dynamics, and obtained \mathbf{o}_n integrating \mathbf{X}_c backwards, under the SE-system dynamics. Finally, the

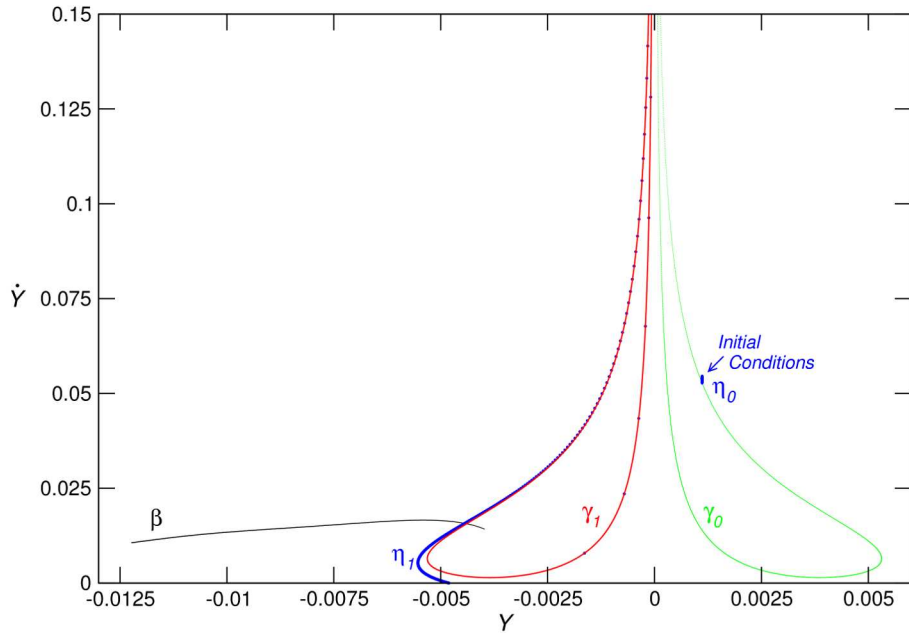


FIGURE 4.3 – The nearby initial conditions around the Earth in the η_0 line segment are mapped onto the blue curve η_1 along the red curve γ_1 , which is the cut of the inner branch of W_{\odot}^u in the Σ_c section. The green curve γ_0 corresponds to the cut of the inner branch of W_{\odot}^s in the Σ_c section. The black curve β corresponds to the Poincaré cuts of trajectories generated by the time reverse integration under the EM-system dynamics of a single initial condition near the Moon for $0 \leq \theta^* < 2\pi$, that is, for different initial phase angles between the SE and EM systems at the patching instant.

complete transfer orbit \mathbf{o}_c was composed by \mathbf{o}_t and \mathbf{o}_n (see Figure 4.4).

4.2 Investigation of the Patching Procedure

In this Section, we will outline some analyses of the constructive process meant to establish criteria that might define transfer solutions corresponding to better project specifications.

4.2.1 Earth-Moon Portion

The important issue in the Earth-Moon portion of the mission project is to seek trajectories that provide a natural temporary capture state by the Moon in order to reduce the impulse needed to stabilize the spacecraft into the final orbit \mathbf{o}_f . In the particular experiment presented in this section we worked with initial conditions around the Moon defined in Σ_m inside the cut γ_3 of W_{\oplus}^u of Γ^{\oplus} around L_2^{\oplus} for $C^{\oplus} = 3.16117289$, with

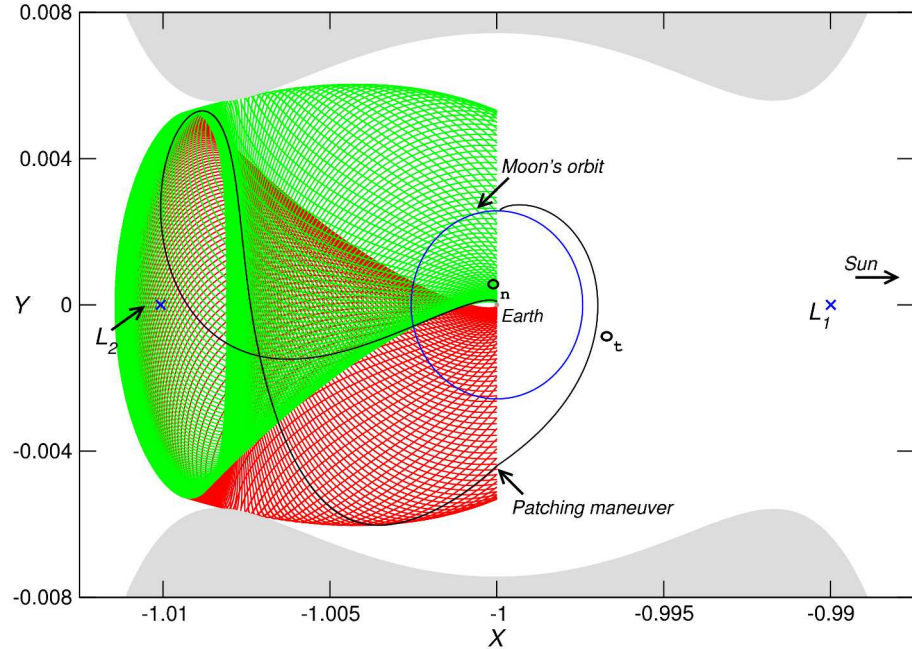


FIGURE 4.4 – Projection onto the X - Y plane of a complete transfer orbit \mathbf{o}_c (black curve). The SE and EM portions are labeled as \mathbf{o}_n and \mathbf{o}_t , respectively. The projections of the inner branches of W_{\odot}^s and W_{\odot}^u are shown in green and red, respectively. The grey areas correspond to the forbidden region, for $C^{\odot} = 3.00080369$. The blue curve corresponds to the orbit of the Moon as seen in the SE rotating frame.

$y = 4.78147 \times 10^{-3}$, corresponding to a constant altitude of about 100 km. The line of initial conditions defined by these requirements are shown in Figure 4.5. These initial conditions integrated forward under the EM-system dynamics generate trajectories that naturally approach the Moon.

A key point to perform the conjugation of the portions is to determine the initial phase α for each candidate trajectory of the Earth-Moon portion, that is, the position of the Moon with respect to the line connecting the Earth and the Sun at $t = 0$ of the time reversed integration of the initial conditions around the Moon in Σ_m . This is equivalent to finding the time of flight until the patching section Σ_c in the SE-system which is rotating with respect to the EM synodic reference frame.

Alternatively, to overcome this difficulty, instead of defining Σ_c , we define a Σ_c^* corresponding to a certain θ^* in the Earth-Moon reference frame. Each value of θ^* defines an

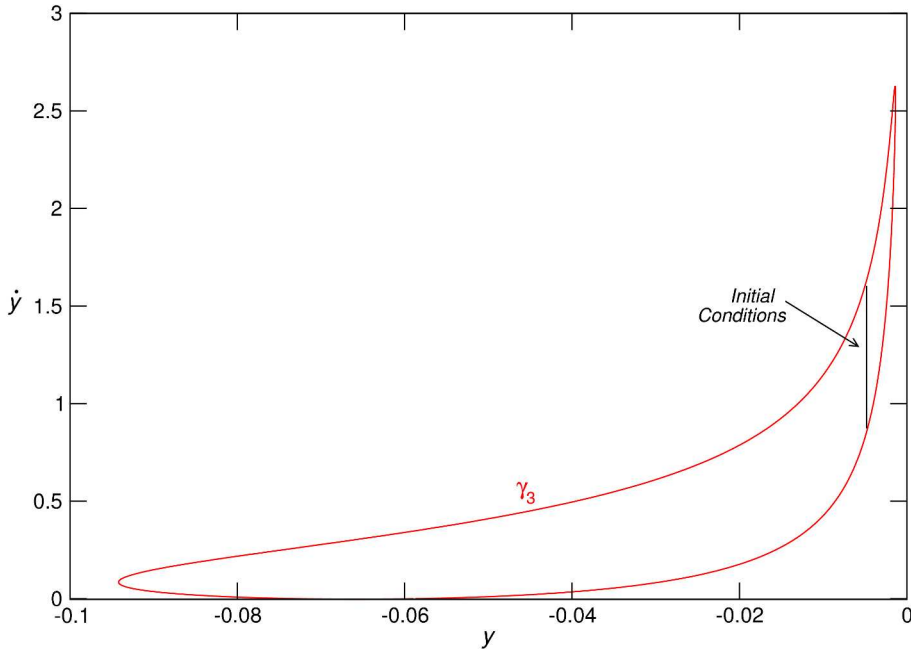


FIGURE 4.5 – Line of initial conditions (black) defined at Σ_m by $y = 4.78147 \times 10^{-3}$ inside the γ_3 cut of the inner branch of W_{\oplus}^u (red curve).

initial phase α for each initial condition. The initial phase is easily found given that we know the time of flight of each trajectory from the initial state up to Σ_c^* .

We are interested only in trajectories that cross Σ_c^* in the exterior realm of the EM-system. For the particular energy shell considered in this investigation, this requirement implies that $\theta^* \geq \theta_{min}^* \approx 3.49$ rad. From this threshold value, we consider a 2π angular variation in order to compute the corresponding flight time and the values of the initial phase α for a given initial condition.

Considering, $\theta_{min}^* \leq \theta^* < \theta_{min}^* + 2\pi$ with angular step $\Delta\theta^* = 0.017453$ rad, we obtain Figure 4.6 which displays the Poincaré cuts of the generated trajectories at section Σ_c^* as seen in section Σ_c . Each line corresponds to the successive Poincaré cuts of a single initial condition as $\theta_{min}^* \leq \theta^* < 2\theta_{min}^* + 2\pi$. Figure 4.7 shows how the phase α and the time of flight up to section Σ_c^* depend on the choice of θ^* for a given initial condition in the line of Figure 4.5. The discontinuity occurs because we have chosen to represent $\theta^* \geq 2\pi$ as $\theta^* - 2\pi$.

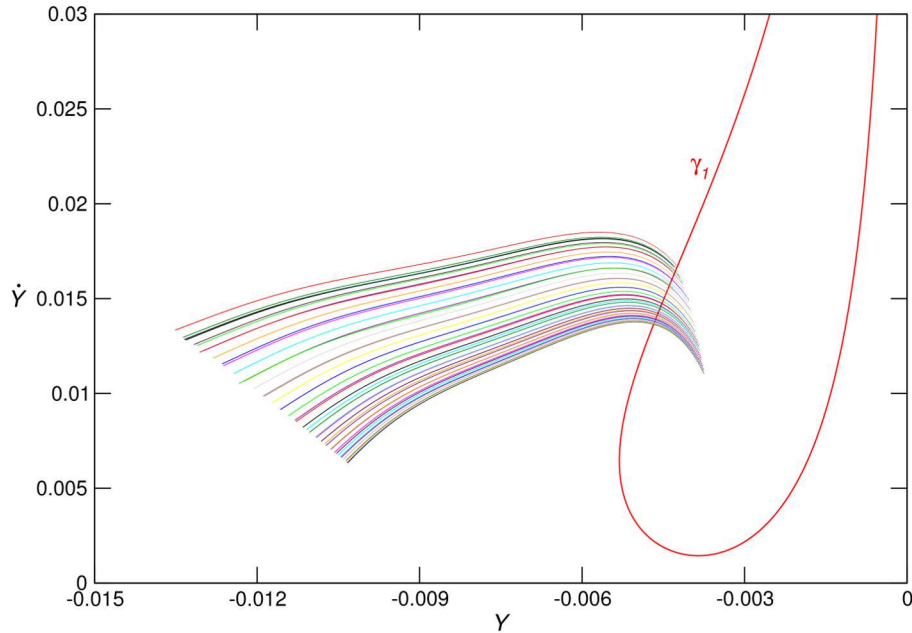


FIGURE 4.6 – Σ_c Poincaré cuts of trajectories inside W_\oplus^s for several initial phases. The initial conditions considered are defined around the Moon inside the cut γ_3 of W_\oplus^u in the Σ_m section for $C^\oplus = 3.16117289$, and $y = 4.78147 \times 10^{-3}$. Each line corresponds to the successive Poincaré cuts of a single initial condition as $\theta_{min}^* \leq \theta^* < +\theta_{min}^* + 2\pi$, with $\Delta\theta^* = 0.017453 \text{ rad}$. The red curve is the γ_1 cut of W_\oplus^u at section Σ_c .

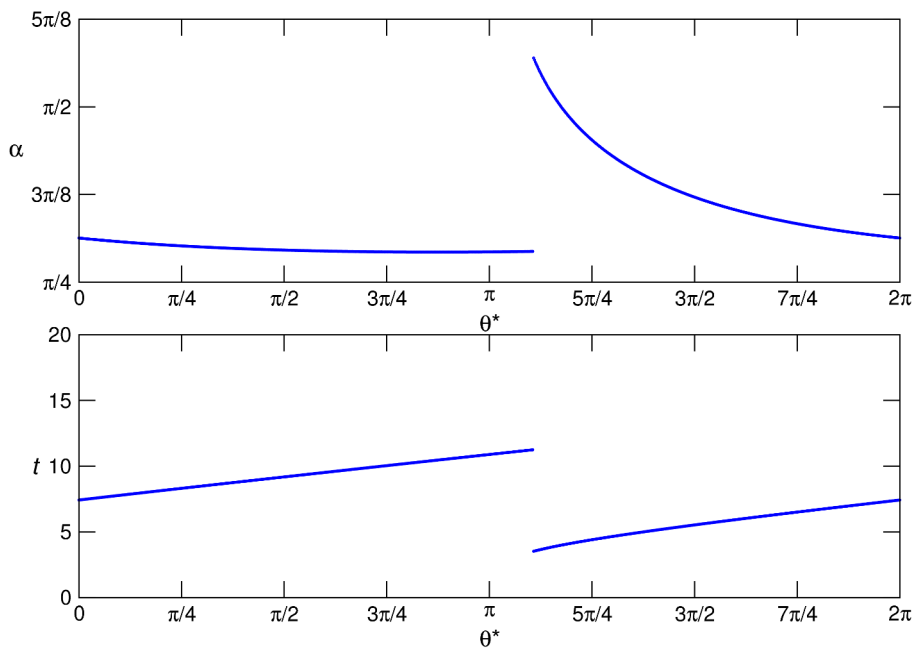


FIGURE 4.7 – (a) Initial phase α as a function of θ^* . (b) Flight time (in Earth-Moon dimensionless time units) up to Σ_c^* section for an initial condition with $y = 4.78147 \times 10^{-3}$ as a function of θ^* .

This experiment shows that not all $\alpha \in [0, 2\pi]$ are allowed. Specifically, for the case presented in Figure 4.7, we find that $0.87266463 \lesssim \alpha \lesssim 1.91986218$. Moreover, the best flight time intervals are found for α values slightly below 1.91986218.

4.2.2 Sun-Earth Portion

Neighboring initial conditions around the Earth defined in the Σ_e section nearby the Poincaré cut γ_0 of the inner branch of W_\odot^s are mapped along the γ_1 cut of the inner branch of W_\odot^u in the Σ_c section (see Figure 4.3). This sensitive dependence on initial conditions, which is a signature of chaotic behavior, must be taken into account when projecting the Sun-Earth portion of the transfer trajectory.

The important issue in the Sun-Earth portion of the mission is to seek trajectories that fulfill practical mission requirements and that reach Σ_c in a region that provides intersection with the outer branch of W_\oplus^s within a reasonable time interval. These requirements are not certainly fulfilled by an arbitrary choice of initial conditions in the η_0 segment.

The practical requirement considered in this work refers to feasible LEO and MEO geocentric parking orbits¹. Also, we will require that initial conditions around the Earth have null radial velocity, so that an impulsive maneuver tangent to the circular parking orbit will suffice to inject the spacecraft into the transfer orbit \mathbf{o}_n .

The usual approach consists in determining a single patching solution based on the construction presented in Section 4.1.1. Aiming to establish a more general approach that allows the determination of sets of initial conditions with practical applicability, we define the following subsets of the phase space:

¹The LEO (Low Earth Orbit) region extends from Earth's surface up to 2,000 km of altitude. LEO orbits usually have low eccentricities, inclinations from 0 to 60° and altitudes ranging from 160 km to 2,000 km, since orbital decay of objects in lower orbits is very pronounced. For the MEO (Medium Earth Orbit) region we have considered altitudes going from 2,000 km up to 35,786 km.

$$A_0 = \left\{ (X, Y, \dot{X}, \dot{Y}) \in \mathbb{R}^4 \mid J(X, Y, \dot{X}, \dot{Y}) = C^\odot \right\}, \quad (4.1)$$

$$A_1 = \left\{ (X, Y, \dot{X}, \dot{Y}) \in \mathbb{R}^4 \mid R_i \leq R_1 \leq R_f \right\}, \quad (4.2)$$

$$A_2 = \left\{ (X, Y, \dot{X}, \dot{Y}) \in \mathbb{R}^4 \mid \dot{R} = 0 \right\}, \quad (4.3)$$

where $R_1 = \sqrt{(X - X_{P_1})^2 + Y^2}$ is the distance from P_3 to P_1 in the SE synodic normalized reference frame and \dot{R} is the radial velocity of P_3 with respect to P_1 . We chose $R_i = R_E + 150$ km and $R_f = R_E + 36000$ km, where R_E is the Earth's Equatorial radius, in order to define an annular region that contains LEO and MEO orbits.

Now, we define

$$A = A_0 \cap A_1 \cap A_2, \quad (4.4)$$

the set of prograde ($\dot{\theta} > 0$) or retrograde ($\dot{\theta} < 0$) initial conditions in a given energy shell, with null radial velocity, and in an annular region around the Earth that allows feasible parking orbits.

4.2.3 Characterization of Trajectories in the Sun-Earth Portion

Let A^+ denote the subset of prograde initial conditions in A (Equation (4.4)). In this Subsection, we will investigate five subsets A_I^+ , A_{II}^+ , A_{III}^+ , A_{IV}^+ , and A_V^+ , generated for

$$C_I = 3.00089571, \quad C_{II} = 3.00088303, \quad C_{III} = 3.00085596,$$

$$C_{IV} = 3.00081838, \quad C_V = 3.00077291.$$

In order to simplify the notation we have dropped the \odot superscript that refers to the Sun-Earth system. The generation of the initial condition sets for each C_N value was accomplished with a discrete grid of points in position space using P_1 -centered polar

coordinates, R_1 and θ . We took $0 \leq \theta < 2\pi$, with $\Delta\theta = \pi/720$, and $R_i \leq R_1 < R_f$, with $\Delta R_1 \approx 8 \times 10^{-7}$.

The ΔV_0 needed to inject the spacecraft into the orbits defined by these sets of initial conditions is comparable to the first impulse of a tri-impulsive bi-elliptic transfer with the apoapsis of the first transfer semi-ellipse equal to 1.0×10^6 km. So, comparing to a bi-elliptic transfer, the energy savings provided by the employment of the SE and EM systems invariant structures are to be expected only in the second maneuver (at the patching point) and in the third maneuver (to stabilize the trajectory into the final selenocentric orbit).

Figure 4.8 shows the five Lyapunov orbits around L_2^\odot corresponding to the energy levels defined by C_N . The Σ_c Poincaré cuts of the inner branches of the unstable manifolds of such orbits are also shown. The vertical straight line in the right frame of Figure 4.8 is adopted as a practical boundary between the exterior realm (to the left side of the line) and the lunar realm on the EM-system. The limiting Y value $Y_{lim} = Y_{L_2^\oplus}$ is needed in order to ensure that the manifolds intersect in the exterior realm of the EM-system.

So, the initial conditions in A_N^+ were integrated forward and separated in five subsets according to the behavior of the generated trajectories:

B_2^+ : Trajectories that reach Σ_c with $Y < Y_{lim}$, $\dot{Y} \geq 0$.

B_3^+ : Trajectories that reach Σ_c with $Y < Y_{lim}$, $\dot{Y} < 0$.

B_w^+ : Trajectories that reach Σ_c with $Y > Y_{lim}$.

B_K^+ : Trajectories that collide with the Earth before they reach Σ_c .

B_T^+ : Trajectories that don't reach Σ_c and don't collide before the maximum integration time T . In these experiments we set $T = 10$ dimensionless SE time units, which corresponds to about 580 days.

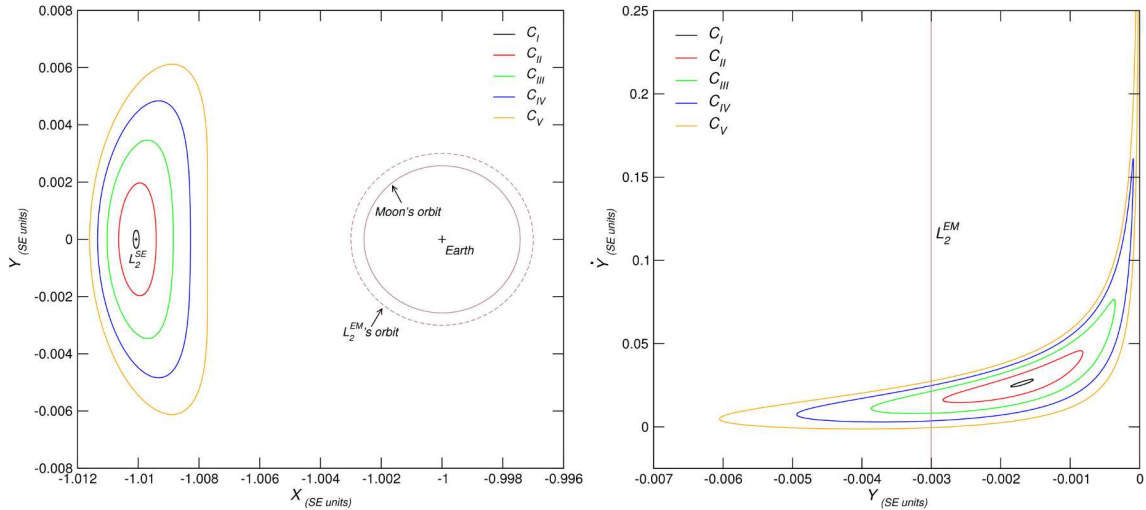


FIGURE 4.8 – **Left:** Projection onto the X - Y plane of five Lyapunov orbits around L_2^\odot , corresponding to C_I , C_{II} , C_{III} , C_{IV} , and C_V . The orbit of the Moon as seen in the SE synodic normalized reference frame is shown as a brown curve around the Earth. The orbit of L_2^\oplus is also shown (dashed brown curve around the Earth). **Right:** Σ_c Poincaré cuts of the inner branches of the unstable manifolds of the Lyapunov orbits shown in the left frame. The brown vertical line corresponds to the orbit of L_2^\oplus in the SE synodic normalized reference frame.

We will be interested in initial conditions that belong to B_2^+ , given that the intersection of W_\oplus^s and W_\odot^u in Σ_c occurs for $Y < Y_{lim}$, $\dot{Y} \geq 0$, as seen in Figure 4.2. Trajectories generated by initial conditions in B_w^+ are not appropriate for mission design in the patched three-body approach because they reach Σ_c with $Y > Y_{lim}$, that is, inside the Moon realm of the EM-system. Trajectories generated by initial conditions in B_3^+ are not appropriate because they reach Σ_c with opposite sense of velocity in the Y direction.

Figures 4.9 and 4.10 show the classification of the A_N^+ sets, and how B_2^+ , B_3^+ , and B_w^+ are mapped in Σ_c . The first observation we draw from these Figures is that the amount of candidate states, i.e., initial conditions in B_2^+ , is very small for the five energy shells considered in the experiments (see Table 4.1). In addition, we find that the number of initial conditions in B_3^+ remains practically unchanged with C , while the amount of collisional trajectories diminishes as C decreases. Subset B_T^+ was empty for C_I and C_{II} , and the number of initial conditions belonging to that subset increases as C decreases for

	C_I	C_{II}	C_{III}	C_{IV}	C_V
% of IC in B_2^+	0.318	0.266	3.192	3.401	0.742

TABLE 4.1 – Percentage of initial conditions in B_2^+ relative to the total number of initial conditions in each A_N^+ , corresponding to C_N , with $N = I, II, III, IV, V$.

C_{III} , C_{IV} , and C_V .

Concerning the spatial distribution of candidate trajectories, we find that subset B_2^+ is grouped in the second quadrant of the X - Y plane for C_I and C_{II} , while it splits in two groups for C_{III} and C_{IV} . One group remains in the second quadrant of the X - Y plane, while another group lies at right side of A_N^+ . Finally, for C_V , B_2^+ is again a single group, now in the fourth quadrant of the X - Y plane.

The following nomenclature is defined:

T1: trajectories generated by B_2^+ initial conditions in the second quadrant of the X - Y plane;

T2: trajectories generated by B_2^+ initial conditions in the first quadrant of the X - Y plane;

T3: trajectories generated by B_2^+ initial conditions in the fourth quadrant of the X - Y plane.

Figures 4.11, 4.12, 4.13, 4.14, and 4.15 show the X - Y projection of the trajectories generated by initial conditions in B_2^+ for C_I , C_{II} , C_{III} , C_{IV} , and C_V , respectively. Figure 4.16 displays the flight time until those trajectories reach Σ_c . We find that T2 orbits correspond to the same kind of o_n trajectory of the patched three-body construction presented by Koon, *et al.* [4, 5] and also employed in the complete transfer trajectory of Figure 4.4. Most of these orbits follow W_\odot^u and W_\odot^s closely, i.e., although they are outside the invariant tubes, they wind around them closely, approaching the Lyapunov orbit around L_2^\odot before reaching Σ_c . Thus, their flight time intervals are quite long. Partic-

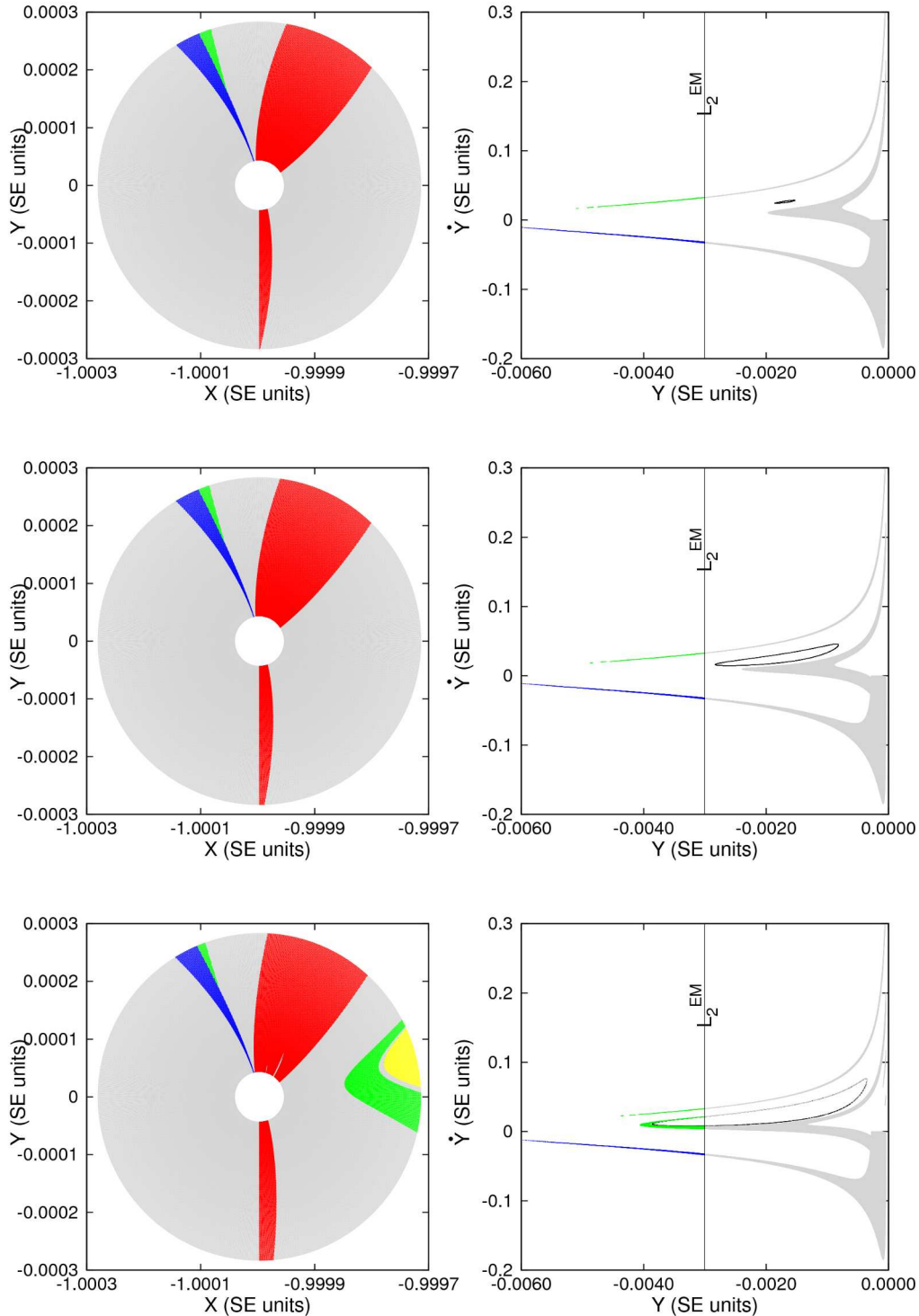


FIGURE 4.9 – Classification of initial conditions in (Top) A_I^+ , (Middle) A_{II}^+ , and (Bottom) A_{III}^+ . Each color corresponds to a subset: **Green:** B_2^+ ; **Blue:** B_3^+ ; **Grey:** B_w^+ ; **Red:** B_K^+ ; **Yellow:** B_T^+ . **Left:** X - Y projection of the initial conditions. **Right:** final states at the Σ_c section of trajectories generated by B_2^+ , B_3^+ , and B_w^+ . The line labeled as L_2^{EM} delimits the region of interest for the patched three-body construction. The Σ_c Poincaré cut of W_\odot^u of the corresponding Γ_2^\odot is shown in black.

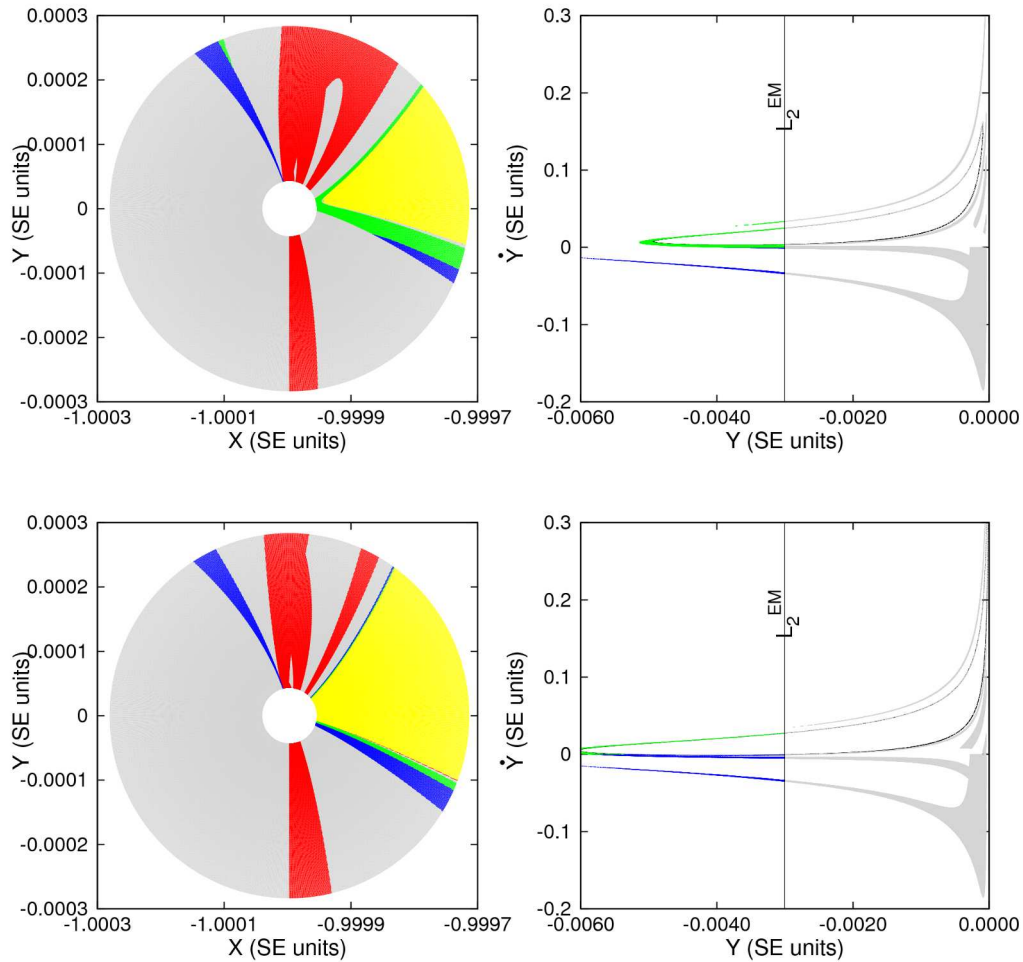


FIGURE 4.10 – Classification of initial conditions in (Top) A_{IV}^+ and (Bottom) A_V^+ . Each color corresponds to a subset: **Green:** B_2^+ ; **Blue:** B_3^+ ; **Grey:** B_w^+ ; **Red:** B_K^+ ; **Yellow:** B_T^+ . **Left:** X - Y projection of the initial conditions. **Right:** final states at the Σ_c section of trajectories generated by B_2^+ , B_3^+ , and B_w^+ . The line labeled as L_2^{EM} delimits the region of interest for the patched three-body construction. The Σ_c Poincaré cut of W_{\odot}^u of the corresponding Γ_2^{\odot} is shown in black.

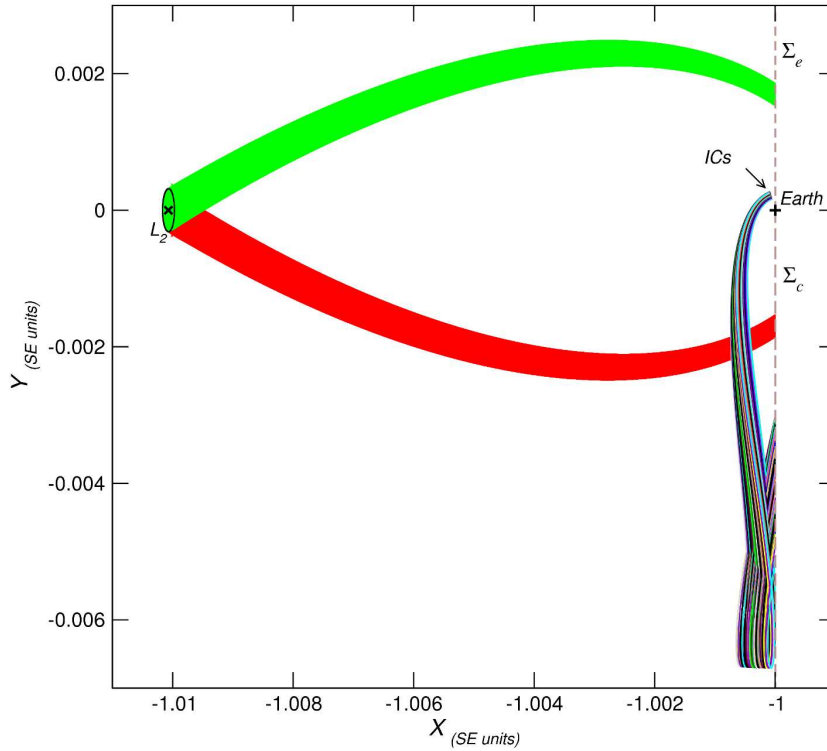


FIGURE 4.11 – X - Y projection of trajectories generated by initial conditions in B_2^+ for C_I . The Lyapunov orbit around L_2^\odot (black curve) and its stable (green) and unstable (red) manifolds are also shown.

ularly, for C_{III} , the flight time varies from about 100 days to about 150 days. Some trajectories are so close to the stable tube that may take up to 300 days to reach Σ_c . Usually, the flight time increases as C decreases. For C_V , it varies from about 150 days to about 220 days.

$T3$ orbits still follow the W_\odot^u and W_\odot^s , but many of them are not so close to the SE-system invariant structures, so the intervals of flight time are considerably shorter compared to the ones of $T2$ orbits. Also, unlike $T2$ orbits, the trajectories generated by initial conditions in the fourth quadrant of the X - Y plane do not come very close to the Lyapunov orbit around L_2^\odot .

Unexpectedly, $T1$ orbits do not follow the invariant tubes. They are quasiperiodic trajectories, each of them lying on a torus of a large stable island around the Earth. The most striking feature of this type of orbits is that they present the shortest flight time

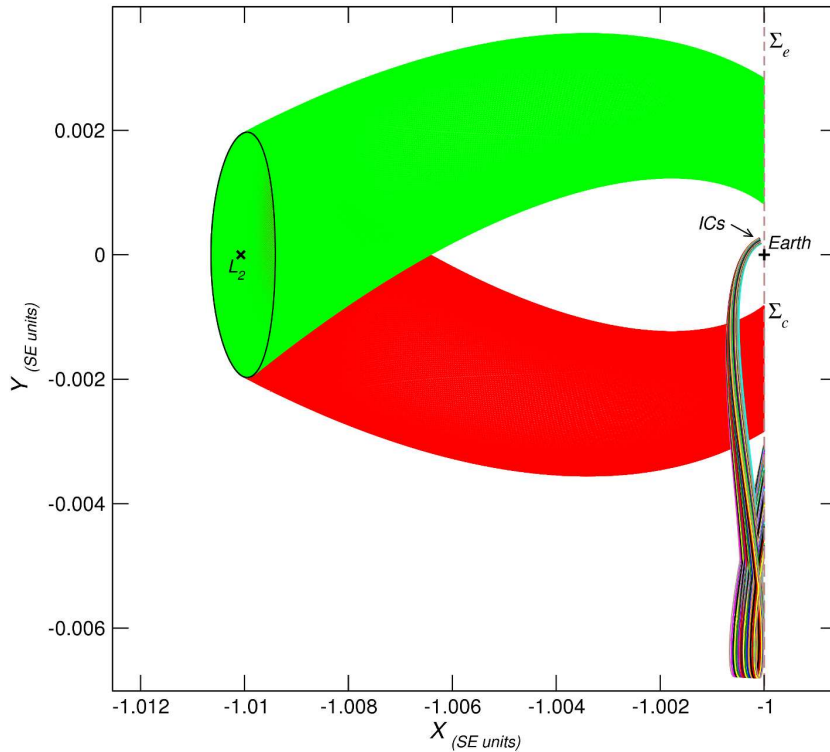


FIGURE 4.12 – X - Y projection of trajectories generated by initial conditions in B_2^+ for C_{II} . The Lyapunov orbit around L_2^\odot (black curve) and its stable (green) and unstable (red) manifolds are also shown.

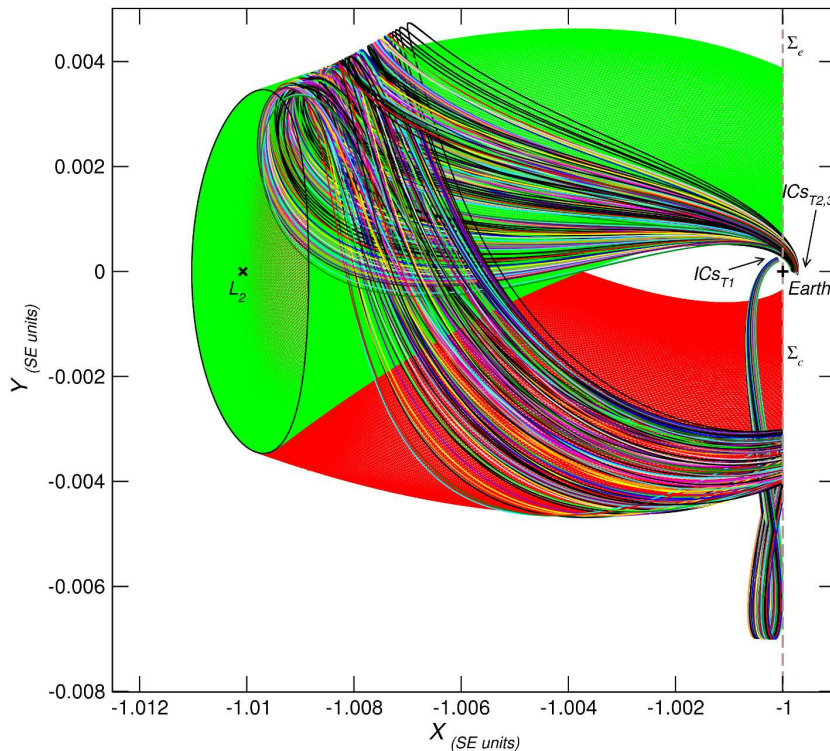


FIGURE 4.13 – X - Y projection of trajectories generated by initial conditions in B_2^+ for C_{III} . The Lyapunov orbit around L_2^\odot (black curve) and its stable (green) and unstable (red) manifolds are also shown.

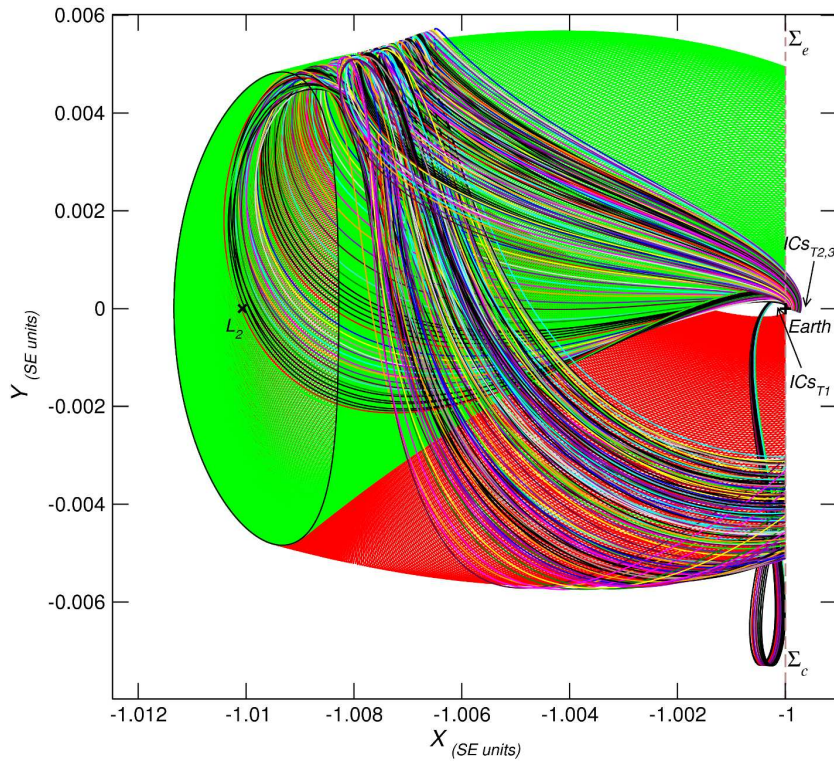


FIGURE 4.14 – X - Y projection of trajectories generated by initial conditions in B_2^+ for C_{IV} . The Lyapunov orbit around L_2^\odot (black curve) and its stable (green) and unstable (red) manifolds are also shown.

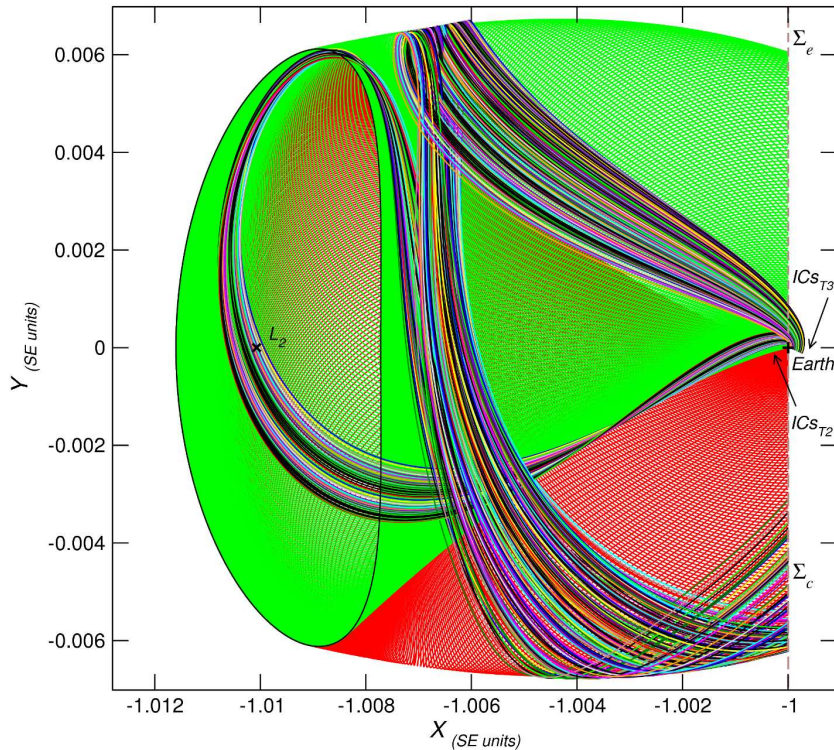


FIGURE 4.15 – X - Y projection of trajectories generated by initial conditions in B_2^+ for C_V . The Lyapunov orbit around L_2^\odot (black curve) and its stable (green) and unstable (red) manifolds are also shown.

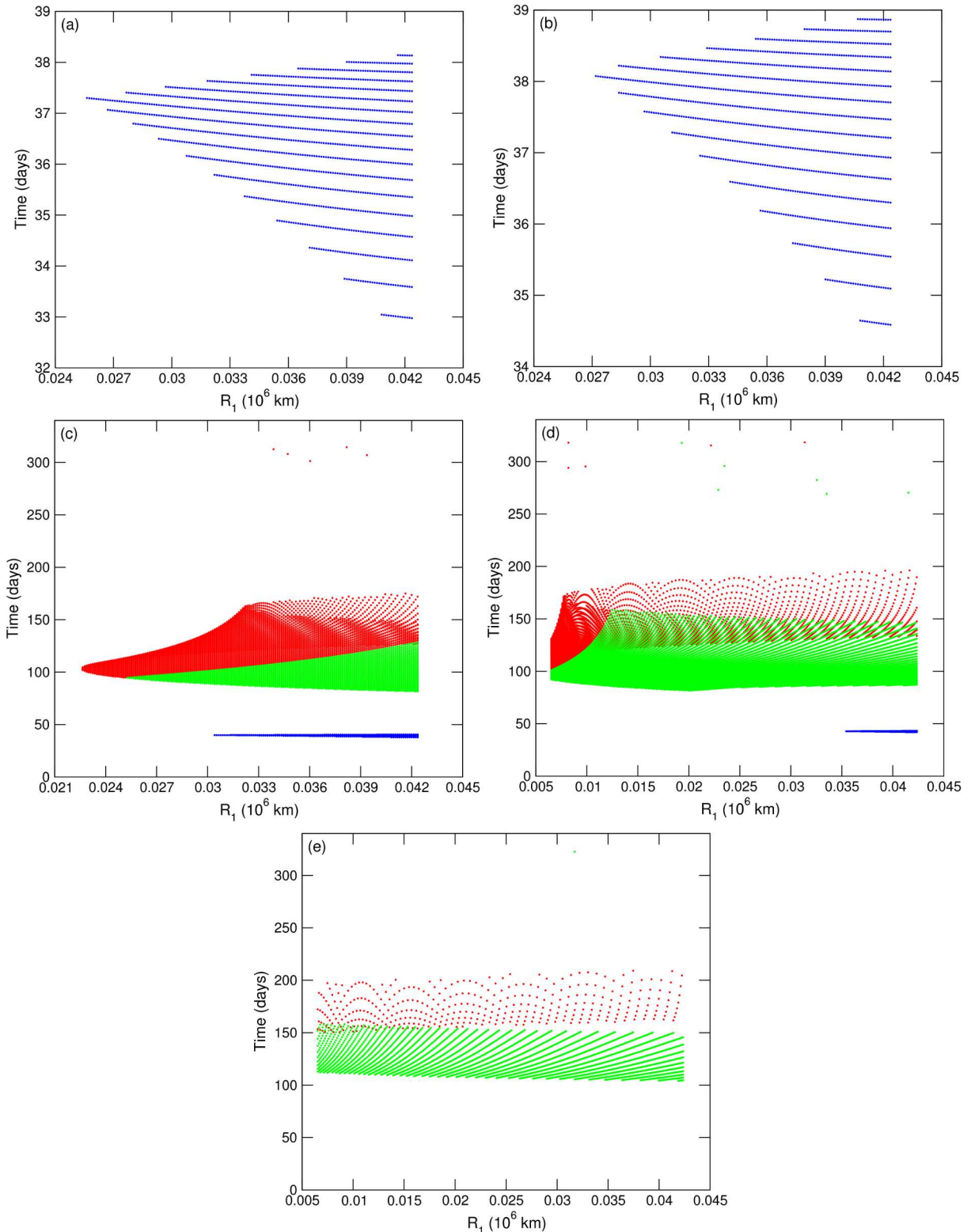


FIGURE 4.16 – Flight time until section Σ_c of trajectories generated by initial conditions in B_2^+ , for (a) C_I , (b) C_{II} , (c) C_{III} , (d) C_{IV} , and (e) C_V . The blue, red, and green points correspond to T_1 , T_2 , and T_3 trajectories, respectively.

intervals. For C_I , these *shortcut* orbits reach Σ_c in 33 to 39 days. The intervals of flight time increase slightly as C decreases, but for all the C values considered, the maximum flight time is less than 50 days. This type of orbits provides an alternative way to reach the patching zone. Besides, given that they are stable solutions of the restricted three-body dynamics they provide a more reliable pathway than $T2$ trajectories, which wonder through the chaotic sea.

From Figures 4.9 and 4.10, we see that the amount of $T1$ trajectories decreases as C decreases. Also, for the C values considered up to now, the initial conditions of those trajectories correspond to high altitude parking orbits around the Earth. Aiming to find initial conditions closer to the Earth, we extended the investigation for higher C values. Given that there is no reason to consider these quasiperiodic *shortcut* orbits only for $C < C_2^\odot$, we included situations at which there is no neck region around L_2^\odot and L_1^\odot . However, candidate trajectories must cross Σ_c with $Y < Y_{lim}$, $\dot{Y} \geq 0$, so we found that the maximum Jacobi constant value allowed is $C_{max} = 3.00201329$. We generated the set of initial conditions A_*^+ with $C_* = 3.00150665$. Around this value of C , the percentage of *shortcut* trajectories reaches its maximum value. From C_* , as $C \rightarrow C_{max}$, the number of initial conditions in B_2^+ diminishes because the trajectories fail to reach Σ_c with $Y < Y_{lim}$. Figure 4.17 shows the classification of set A_*^+ and how B_2^+ , B_3^+ , and B_w^+ are mapped in Σ_c . In this case, initial conditions in subset B_2^+ are 1.865% of the complete set A^+ . The blade of *shortcut* initial conditions comes very near the Earth, corresponding to low altitude parking orbits, and the intervals of flight time range from about 9 to 16 days (see Figure 4.18).

Although some aspects, like the energy cost of the patching of the *shortcut* orbits, need to be further investigated in the complete Sun-Earth-Moon-Sc system, the results

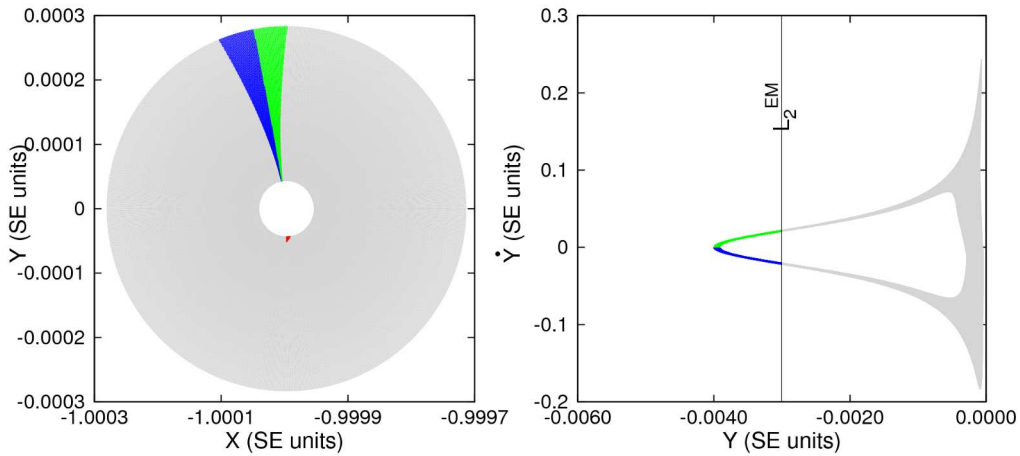


FIGURE 4.17 – Classification of initial conditions in A_*^+ . Each color corresponds to a subset: **Green:** B_2^+ ; **Blue:** B_3^+ ; **Grey:** B_w^+ ; **Red:** B_K^+ ; **Yellow:** B_T^+ . **Left:** X - Y projection of the initial conditions. **Right:** final states at the Σ_c section of trajectories generated by B_2^+ , B_3^+ , and B_w^+ . The line labeled as L_2^{EM} delimits the region of interest for the patched three-body construction. The Σ_c Poincaré cut of W_{\odot}^u is shown in black.

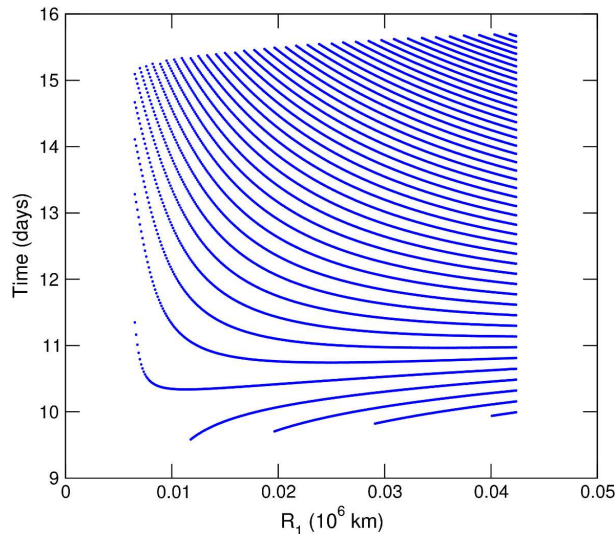


FIGURE 4.18 – Flight time until section Σ_c of trajectories generated by initial conditions in B_2^+ for C_* .

presented in this Section suggest that these quasiperiodic solutions constitute appropriate candidate trajectories for application in Earth-to-Moon transfers, reducing considerably the flight time of the Sun-Earth portion of the mission.

4.3 Discussion

In this Chapter, we investigated the patched three-body approach for construction of Earth-to-Moon transfers. Concerning the EM-system, considering a final selenocentric orbit of 100 km of altitude, the relevant dynamical variables in the patching procedure are the Jacobi constant value and the initial phase angle between the EM and the SE systems. Concerning the SE portion of the transfer, we proposed and analysed a convenient set of initial conditions around the Earth. We verified the existence of alternative *shortcut* trajectories that can be employed instead of the typical ones of the method. While these typical trajectories follow the invariant structures of L_2 , the *shortcut* orbits are quasiperiodic solutions of the SE PCR3BP.

Although lacking some aspects concerning the complete characterization of the construction procedure, the investigation presented in this Chapter is deep enough to guide our analyses of the WSB, regarding its applicability in ballistic lunar capture in the final portion of a complete Earth-to-Moon transfer trajectory.

5 WSB Associated Sets in the Lunar SOI

In the earliest statements of the algorithmic construction of the stability boundary nothing was asserted about the extension of the region in the phase space of the PCR3BP for the Earth-Moon system to which the concept was associated. Since the reviewed algorithmic definition by F. García and G. Gómez [8], several papers have appeared in which the sets of initial conditions from which the algorithmic WSB is extracted are generated over a broad region in the x - y plane that extends far away from the Moon.

At an early stage of this work, the WSB algorithmic definition was implemented choosing the ranges of the spatial coordinates according to Ref. [8]. The results of a series of dynamical analyses performed in order to characterize the generated sets in view of ballistic capture transfers are published in Ref. [25].

Following, we restricted our analyses to initial conditions inside the lunar SOI for two main reasons. In the first place, the Kepler energy can be used as a reliable quantifier of the P_2 - P_3 subsystem of the three-body problem in this region, in the sense that the third body effects can be treated as a perturbation. We have considered Laplace's definition of the SOI¹, so that the Moon's SOI radius, r_{S2} , can be approximated by the Hill radius² $r_H \approx 6.4 \times 10^4$ km (≈ 0.1678 EM-system dimensionless units).

Secondly, each initial condition of the algorithmic construction corresponds to a possible arrival state of a complete Earth-to-Moon transfer orbit; therefore these points should

¹Appendix B.

²In the PCR3BP, the Hill radius is the distance from P_2 to the L_1 Lagrangian point.

be chosen in the vicinity of the Moon so that they are near enough for mission design. Although, the subsets that are appropriated for typical selenocentric orbits for practical applications are initial conditions with altitudes near 100 km, for completeness, the characterization of the sets generated by the algorithmic definition is performed in the entire lunar SOI.

Organization of the Chapter: In Section 5.1, our two WSB algorithmic implementations are presented. In Section 5.2, the generated initial conditions are classified according to the integral of motion of the PCR3BP in order to verify the availability of possible transport channels. Also, we discuss the grid-dependency of the results. In Section 5.3, we establish some applicability criteria based on two alternatives for transfer mission projects, namely, direct inner transfers and external transfer procedures based on a patched three-body approximation. In this section we compile the results of the retrograde analyses of applicability for the complete sets of initial conditions in the lunar SOI. In Section 5.4, we focus on the stable sets given that they are the natural candidates to produce ballistic capture orbits. First, the retrograde applicability analyses are quantified. Secondly, we proceed with two prograde analyses meant to elucidate the classification criteria of the WSB algorithmic construction, namely, the location of the final state after a complete cycle with respect to the lunar sphere of influence and the permanence within that region during a full cycle around the Moon. In addition, the dynamical diversity in the stable set is presented and characterized. Finally, Section 5.5 is devoted to the discussion of the results of the presented analyses. The analyses and results of this Chapter were recently submitted for publication [32].

5.1 Implementations of the Algorithmic Definition

The generation of the initial condition sets for each eccentricity value was accomplished with a discrete grid of points in position space using P_2 -centered polar coordinates, r_2 and θ . We took $0 \leq \theta < 2\pi$, with $\Delta\theta = \pi/1000$, and $0.00465140 \leq r_2 < 0.21263787$, with $\Delta r_2^0 = 7.80437044 \times 10^{-4}$. The chosen radial range corresponds to altitudes from 50 to 80,000 km. Although we are interested in analysing only initial conditions with $r_2 < r_H$, the maximum r_2 exceeds r_H by approximately 14,000 km.

We will refer to the sets of initial conditions inside the lunar SOI with positive and negative initial velocity as $IC^+(e)$ and $IC^-(e)$, respectively, where e identifies the eccentricity of the osculating ellipse. The number of initial conditions generated in the lunar SOI for each grid of constant eccentricity is $N_0 = 4.20210 \times 10^5$.

For the classification procedure and all the subsequent analyses, the numerical integration of the equations of motion of P_3 was achieved using a Runge-Kutta-Felberg 7-8 method with automatic step size control and local truncation error less than 10^{-14} . When the particle moves inside a region of radius 10^{-2} around any primary, the equations of motion are regularized using Lemaître's global regularization method³.

We implemented two versions of the WSB algorithmic definition. In implementation A, we considered the usual punctual mass idealization for the primaries, while in implementation B, the Moon was regarded as a finite body with mean radius of $\approx 1,738$ km, such that trajectories may collide with that primary. Both implementations generate stable and unstable sets, \mathcal{S} and \mathcal{U} , respectively, according to Definition 4. The unstable set is subclassified according to five instability criteria:

\mathcal{E} : instability due to non-negative Keplerian energy, when trajectories return to $l(\theta)$

³Appendix C.

after one turn around the Moon;

\mathcal{G}^1 : primary interchange through the neck around the L_1 Lagrangian point with $C > C_3$;

\mathcal{G}^2 : primary interchange through the neck around the L_2 Lagrangian point with $C > C_3$;

\mathcal{G}^3 : generic geometric escape with $C < C_3$;

\mathcal{T} : instability due to exceeding the maximum integration time, without returning to $l(\theta)$ or going around the larger primary.

As in Ref. [8], the maximum integration time for the classification procedure was set equal to 80 dimensionless time units, which corresponds to nearly 350 days. In the second, third and fourth unstable cases, P_3 is required to complete a full revolution around P_1 . The existence of different unstable behaviors lead us to expect different types of transitions.

In Figure 5.1, frames (a,c,e) present the projection onto the x - y plane of the $\partial\mathcal{W}^e$ associated sets generated by implementation A, for positive initial velocity with the following eccentricity values: (a) $e = 0.0$, (c) $e = 0.6$, and (e) $e = 0.9$. Frames (b,d,f) display only the stable (\mathcal{S}) and the lunar collisional (\mathcal{C}^M) sets obtained through implementation B for (b) $e = 0.0$, (d) $e = 0.6$, and (f) $e = 0.9$. The same is shown in Figure 5.2 for initial conditions with negative initial velocity.

Figures 5.1 and 5.2 show that the spatial distribution of the associated sets generated by the proposed algorithm in the cases of initial conditions with positive and with negative initial velocities is completely different. For low eccentricity, the stable set is usually located in a large region around the Moon, for both senses of the initial velocity. Thin structures spread vertically from this central region for positive initial velocity. As the eccentricity increases, this core region diminishes and, for negative velocities, its shape becomes irregular.

For initial conditions with positive initial velocity, the lunar collisional set spreads

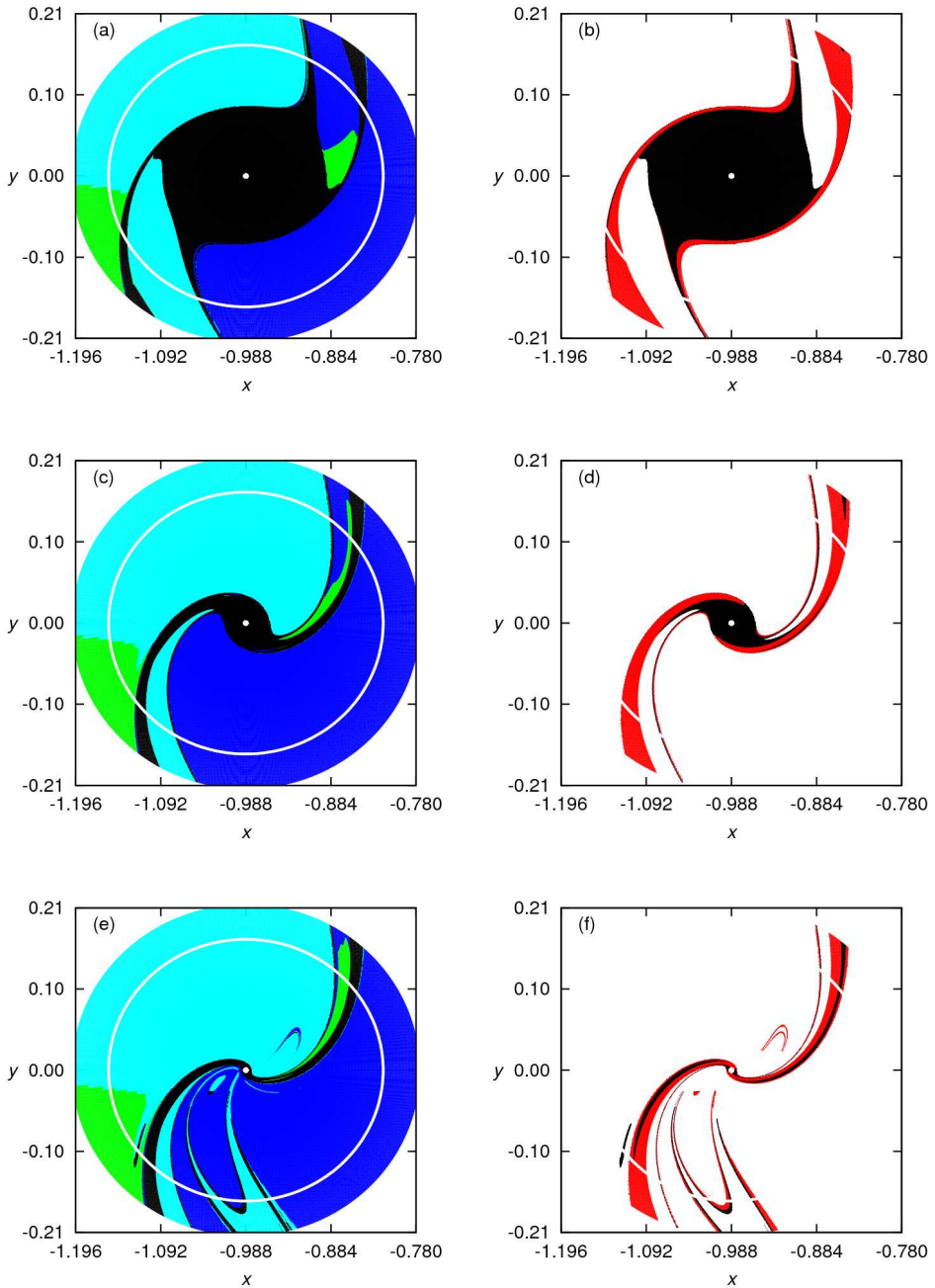


FIGURE 5.1 – Projection onto the x - y plane of the sets generated by the WSB algorithmic definition with positive initial velocity (osculating prograde motion about P_2) for: **(a,b)** $e = 0.0$, **(c,d)** $e = 0.6$, and **(e,f)** $e = 0.9$. Frames **(a,c,e)** refer to the case when no collision with the finite mean radius of the Moon is taken into account; i.e., implementation A, while frames **(b,d,f)** display the stable and the lunar collisional sets when the finite radius of the Moon is taken into account in the implementation B. **Black:** \mathcal{S} , stable; **Red:** \mathcal{C}^M , collision with the Moon; **Green:** \mathcal{E} , instability due to non-negative Kepler energy; **Blue:** \mathcal{G}^1 , primary interchange through L_1 with $C > C_3$; **Cyan:** \mathcal{G}^2 , primary interchange through L_2 with $C > C_3$. The white curve depicts the lunar SOI boundary, which is approximated by the circle with the Hill radius.

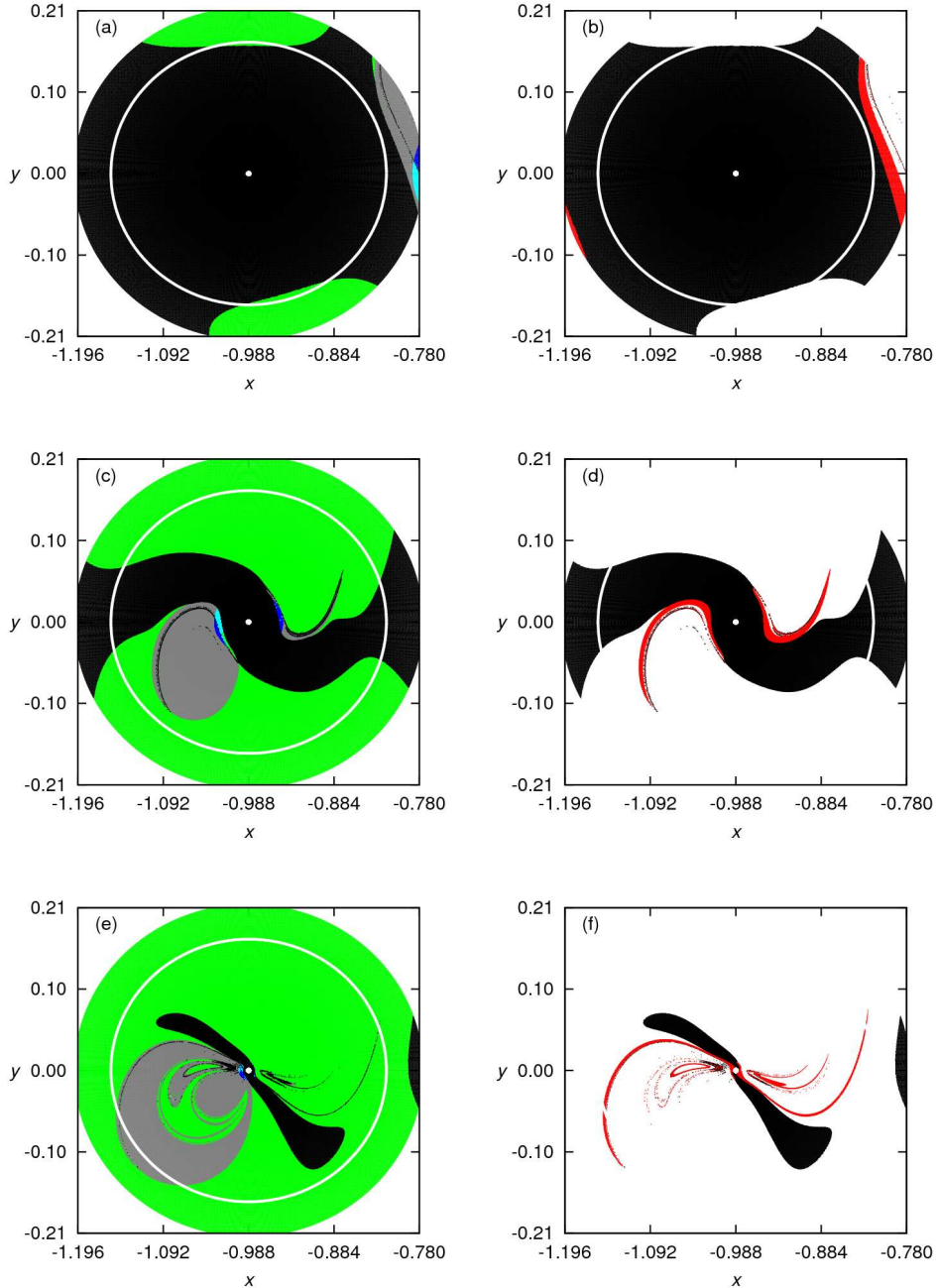


FIGURE 5.2 – Projection onto the x - y plane of the sets generated by the WSB algorithmic definition with negative initial velocity (osculating retrograde motion about P_2) for: (a,b) $e = 0.0$, (c,d) $e = 0.6$, and (e,f) $e = 0.9$. Frames (a,c,e) refer to the case when no collision with the finite mean radius of the Moon is taken into account; i.e., implementation A, while frames (b,d,f) display the stable and the lunar collisional sets when the finite radius of the Moon is taken into account in the implementation B. **Black:** \mathcal{S} , stable; **Red:** \mathcal{C}^M , collision with the Moon; **Green:** \mathcal{E} , instability due to non-negative Kepler energy; **Blue:** \mathcal{G}^1 , primary interchange through L_1 with $C > C_3$; **Cyan:** \mathcal{G}^2 , primary interchange through L_2 with $C > C_3$; **Grey:** \mathcal{G}^3 , geometric escape with $C < C_3$. The white curve depicts the lunar SOI boundary, which is approximated by the circle with the Hill radius.

along the stable set boundary, as can be seen from Figure 5.1. In the case of negative initial velocity, Figure 5.2, the lunar collisional set is more restricted and there are regions of the boundary of the stable set that do not coexist with collisional orbits.

In principle, the stable set would be associated to ballistic capture since it corresponds to the set of initial conditions that, under natural dynamics, depart from and return to a radial segment $l(\theta)$ and have $h_K < 0$ both in the initial and the final state of the trajectory. It is claimed in Ref. [7] that the ideal transfer trajectories lie in the WSB set, i.e., along the boundary between sets with different stability behaviors.

With the explicit generation of unstable set and its subclassification, we see that WSB can be decomposed into distinct subsets with diverse stable-unstable transitions.

Given that the stability criterion is related to a temporary ballistic capture, an impulsive maneuver has to be applied to achieve a permanent capture orbit for the stable set of initial conditions. In this case, circularization can be performed either at the initial condition itself or after one turn around the Moon. However, after one revolution around the primary, stabilization may be energetically more expensive than it would be if it had been performed at the initial condition. Also, even the unstable set can be considered as an arrival state if an impulsive maneuver is performed at the initial condition.

In the usual implementation of the algorithmic WSB found in the literature, the Moon collisional set is overlooked. If circularization is chosen to be performed at the initial condition itself, this does not constitute an issue, but our alternative approach for the numerical implementation reveals that there exist stable trajectories that collide with the Moon under natural dynamics. Moreover, as seen in Figures 5.1 and 5.2, the boundary itself may be partially contained in the collisional set. Thus, unless collision is desirable, the practical applicability of such trajectories must be restricted to circularization at the

initial conditions.

5.2 Classification of the Initial Conditions Sets According to the Jacobi Constant

Every $\partial\mathcal{W}^e$ set is obtained by fixing a two-body problem quantity, i.e., the osculating ellipse eccentricity, while the Jacobi constant, the invariant of the PCR3BP, is left free.

Transport properties in the PCR3BP are intimately related with the five possible Hill region profiles which are delimited by the critical Jacobi constants, C_k , and have direct implications for the availability of Earth-to-Moon natural ballistic capture transfer trajectories. Thus, it is important to classify the initial conditions in the $IC^\pm(e)$ sets according to their C values. For each eccentricity, this classification generates five subsets \mathcal{C}^k , $k = 1,2,3,4,5$.

For the grid considered in our numerical experiments and $e \in [0, 1)$, we find initial conditions in all \mathcal{C}^k subsets. Figure 5.3 displays the percentage of initial conditions with positive and negative initial velocities and with $r \leq r_H$ in each subset \mathcal{C}^k , $k = 1,2,3,4,5$, for $0 \leq e < 1$.

Orbits with their initial conditions in subset \mathcal{C}^1 , $C > C_1$, cannot transit between the primaries; therefore, they do not play any role in ballistic capture transfer design. Initial conditions in subset \mathcal{C}^2 may generate trajectories that transit through the neck region around L_1 that connects the realms around P_1 and P_2 for $C_1 > C > C_2$. These orbits can only be associated to internal transfers. The third subset, \mathcal{C}^3 , comprises orbits with $C_2 > C > C_3$. In this case, trajectories may transit to the external realm of motion through the neck region around L_2 , besides transit through the connecting region around L_1 . Initial conditions belonging to \mathcal{C}^3 are important because they allow the less energetic

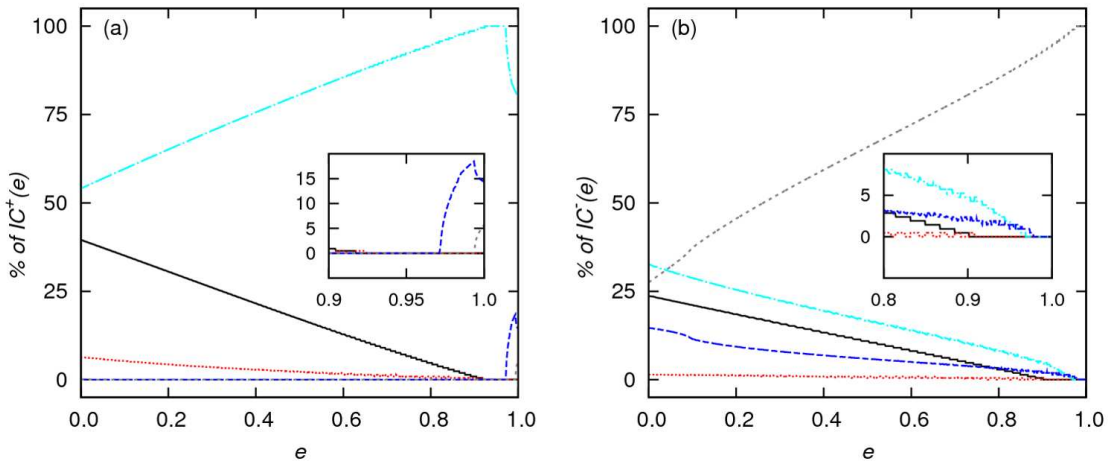


FIGURE 5.3 – The percentage of points in subsets \mathcal{C}^1 (solid, black), \mathcal{C}^2 (dotted, red), \mathcal{C}^3 (dot-dashed, cyan), \mathcal{C}^4 (long-dashed, blue) and \mathcal{C}^5 (dashed, grey) obtained through the classification of (a) $IC^+(e)$ and (b) $IC^-(e)$ according to the Jacobi constant.

external transfers. For $C_3 > C > C_4 = C_5$ there is a neck region also around L_3 and trajectories belong to the fourth subset, \mathcal{C}^4 . Finally, motion over the entire x - y plane is possible for trajectories in subset \mathcal{C}^5 , with $C < C_4 = C_5$.

For the set of initial conditions with positive initial velocity, $IC^+(e)$, subset \mathcal{C}^3 is dominant for all eccentricities. It starts with 54.2% of the points when $e = 0.0$ and increases to 100% when $e = 0.924$. All initial conditions belong to \mathcal{C}^3 for $0.924 \leq e \leq 0.971$. Then, the number of points in \mathcal{C}^3 decreases to about 80.0% as $e \rightarrow 1.0$. Although the $IC^+(e)$ sets provide orbits in energy levels that are appropriate for external transfers, the spatial distribution of such solutions must be observed for actual applications. The percentages of initial conditions in \mathcal{C}^1 and \mathcal{C}^2 are 39.5% and 6.4%, respectively, for $e = 0.0$. So, for low eccentricity, many initial conditions with positive initial velocity are not suited for low energy transfers or only inner transfers may be available, but as $e \rightarrow 0.924$, the percentage of initial conditions in \mathcal{C}^1 and \mathcal{C}^2 decrease to zero. Subset \mathcal{C}^4 is empty for all $e \leq 0.971$. The amount of points in this subset increases up to a maximum of 18.3% at $e = 0.993$, then it decreases to about 14.3% as $e \rightarrow 1.0$. The last subset, \mathcal{C}^5 , which provides trajectories with the highest energy, is nonempty only for $e > 0.993$.

The set of initial conditions with negative initial velocity, $IC^-(e)$, behaves quite differently. Points belonging to all \mathcal{C}^k , $k = 1, 2, 3, 4, 5$ can be found for low and moderate e . For $e = 0.0$, 23.7% of the points with $r_2 < r_H$ do not allow Earth-to-Moon transfer orbits under natural dynamics since they belong to \mathcal{C}^1 . This percentage diminishes as e increases and, for the grid considered, is null for $e > 0.901$. \mathcal{C}^3 starts as the dominant subset with 32.6% of the points for $e = 0.0$ and the number of elements of $\mathcal{C}^3(e)$ decreases as e increases, until this subset is empty for $e \geq 0.969$. Subset \mathcal{C}^5 starts with 27.5% and becomes dominant for $e > 0.039$. The \mathcal{C}^5 subset is equal to $IC^-(e)$ for $e \geq 0.978$. So, as $e \rightarrow 1$, initial conditions with negative initial velocity correspond to solutions of high energy cost.

Figure 5.4 displays the spatial distribution of the subsets $\mathcal{C}^k(e)$, $k = 1, 2, 3, 4, 5$ obtained through the classification according to the Jacobi constant value for initial conditions with positive and negative initial velocities with (a,b) $e = 0.0$, (c,d) $e = 0.6$, and (e,f) $e = 0.9$. Frames (a,c,e) refer to the sets with positive initial velocity, while frames (b,d,f) refer to the sets with negative initial velocity. The percentages of initial conditions in \mathcal{C}^k , relative to the total number of initial conditions in each of these $IC^\pm(e)$ sets are shown in Table 5.1.

The results show the effect of incorporating a two-body quantity as an indicator for a three-body dynamics. For a given eccentricity value, useful and useless orbits appear in the same $IC^\pm(e)$ set. By useless we refer to orbits in \mathcal{C}^1 with energy that does not allow natural transfer trajectories under the dynamics of the PCR3BP. Disconcertingly, the figures show that these initial conditions are usually located at regions associated to typical low lunar orbits of traditional transfers.

As seen in Figure 5.4 (a) and (b), there is a large core region around the Moon with

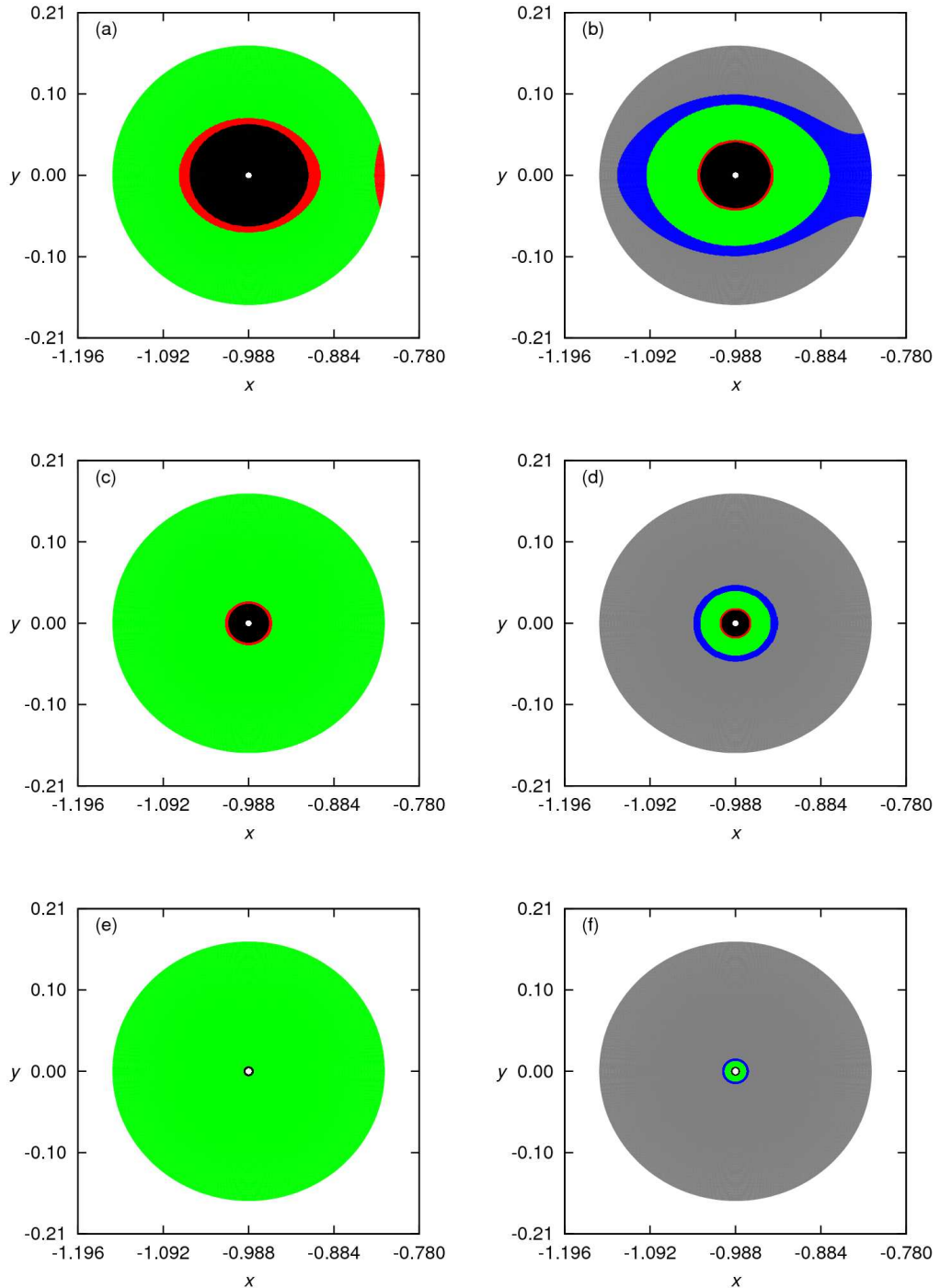


FIGURE 5.4 – Classification according to the Jacobi constant of the initial condition sets for (a,b) $e = 0.0$, (c,d) $e = 0.6$, and (e,f) $e = 0.9$. Frames (a,c,e) refer to positive initial velocity, while frames (b,d,f) refer to negative initial velocity. **Case 1**, \mathcal{C}^1 : $C > C_1$ (black); **Case 2**, \mathcal{C}^2 : $C_1 > C > C_2$ (red); **Case 3**, \mathcal{C}^3 : $C_2 > C > C_3$ (green); **Case 4**, \mathcal{C}^4 : $C_3 > C > C_4 = C_5$ (blue); **Case 5**, \mathcal{C}^5 : $C < C_4 = C_5$ (grey).

initial conditions belonging to \mathcal{C}^1 for low eccentricity values. As the eccentricity increases, \mathcal{C}^1 shrinks, becoming almost nonexistent for higher eccentricities. Generally, for fixed eccentricity, at a same distance r_2 from the Moon, initial conditions with negative initial velocity belong to higher energy cases than initial conditions with positive initial velocity.

For low to moderate eccentricity, both in the case of positive and negative initial velocity, initial conditions that correspond to usual altitudes of selenocentric final orbits considered in realistic projects (approximately 100 km) have very low energy, i.e., they belong to \mathcal{C}^1 or \mathcal{C}^2 . So, for this range of eccentricity values, transfer trajectories that are natural solutions of this three-body model do not exist or only interior transfer trajectories may occur. Thus, for practical applications, e has to be set sufficiently high (typically, $e > 0.9$), implying higher energy costs, with initial conditions belonging to \mathcal{C}^3 for $IC^+(e)$ and to \mathcal{C}^5 for $IC^-(e)$.

	$\mathcal{C}^1 \%$	$\mathcal{C}^2 \%$	$\mathcal{C}^3 \%$	$\mathcal{C}^4 \%$	$\mathcal{C}^5 \%$
$IC^+(0.0)$	39.54	6.39	54.07	0.0	0.0
$IC^+(0.6)$	12.86	1.62	85.52	0.0	0.0
$IC^+(0.9)$	0.95	0.0	99.05	0.0	0.0
$IC^-(0.0)$	23.68	1.51	32.60	14.66	27.55
$IC^-(0.6)$	8.10	0.95	13.79	5.03	72.13
$IC^-(0.9)$	0.48	0.0	4.76	1.90	92.86

TABLE 5.1 – Percentage of initial conditions in each \mathcal{C}^k , $k = 1,2,3,4,5$, relative to the total number of initial conditions in each $IC^\pm(e)$ set.

5.2.1 Grid Dependence of the Classification According to the Jacobi Constant

By implementing several different grids of initial conditions, we find that the results of the classification according to the Jacobi constant are grid-dependent. This occurs because the construction of $IC^+(e)$ and $IC^-(e)$ relies on the discretization of the x - y plane.

Figure 5.5 displays the percentage of initial conditions in \mathcal{C}^1 for $0.82 < e < 0.84$

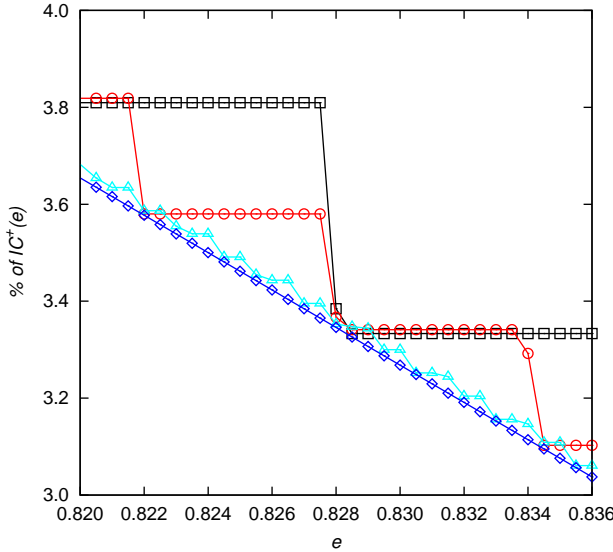


FIGURE 5.5 – The grid dependence of the classification according to the Jacobi constant. The percentages of initial conditions with positive initial velocity in the \mathcal{C}^1 subset are shown for four radial increments: 300 km (black squares), 150 km (red circles), 30 km (cyan triangles), and 3 km (blue lozenges).

when the sets $IC^+(e)$ are generated with fixed $\Delta\theta$ and four different radial increments:

Δr_2^0 , $\Delta r_2^1 = \Delta r_2^0/2$, $\Delta r_2^2 = \Delta r_2^0/10$, and $\Delta r_2^3 = \Delta r_2^0/100$. In physical units, the radial increments correspond to 300, 150, 30, and 3 km, respectively, and the number of initial conditions in the lunar SOI for each grid is N_0 , $N_1 = 2N_0$, $N_2 = 10N_0$, and $N_3 = 100N_0$. For this particular eccentricity range, we see that the percentage of initial conditions in \mathcal{C}^1 depends linearly on e for the finest mesh of points, while the percentage presents pronounced plateaus for larger radial increments.

Figures 5.6 and 5.7 show the variation of the percentage of $IC^\pm(0.9)$ initial conditions in \mathcal{C}^i as a function $\log(\Delta r)$, with $500 \text{ km} \leq \Delta r \leq 1 \text{ km}$. For the tested eccentricity values, we found that radial increments of less than $\approx 10 \text{ km}$ are needed in order to stabilize the percentage of points in each \mathcal{C}^i subset. As an illustration, we also plot the variation of the percentage of $IC^\pm(0.9)$ points in \mathcal{C}^i as a function of the number of initial conditions in $IC^\pm(0.9)$ (Figures 5.8 and 5.9).

The effect is more striking when the spatial distribution of initial conditions belonging

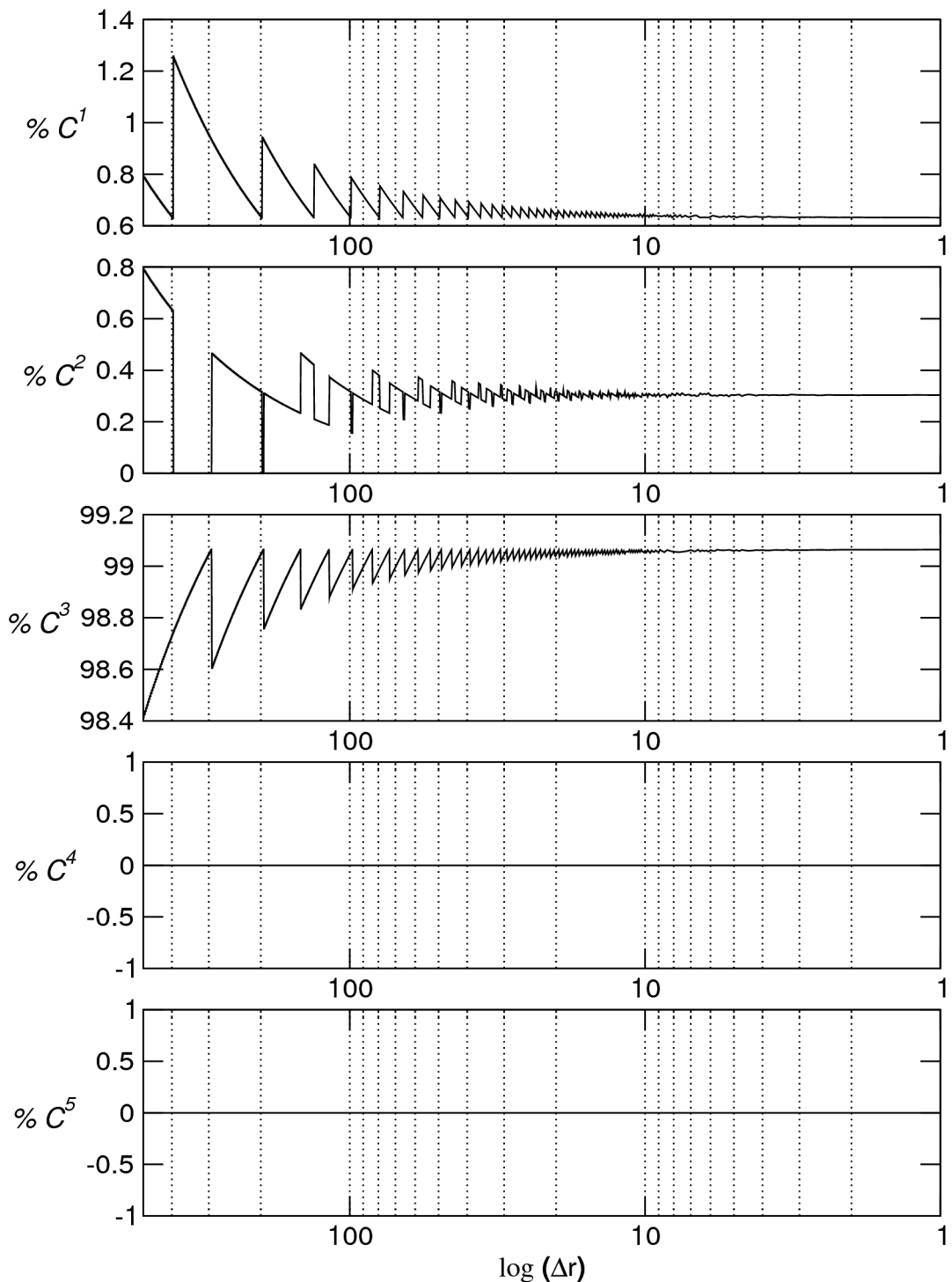


FIGURE 5.6 – Variation of the percentage of $IC^+(0.9)$ initial conditions in \mathcal{C}^k as a function of $\log(\Delta r)$, with $500 \text{ km} \leq \Delta r \leq 1 \text{ km}$.

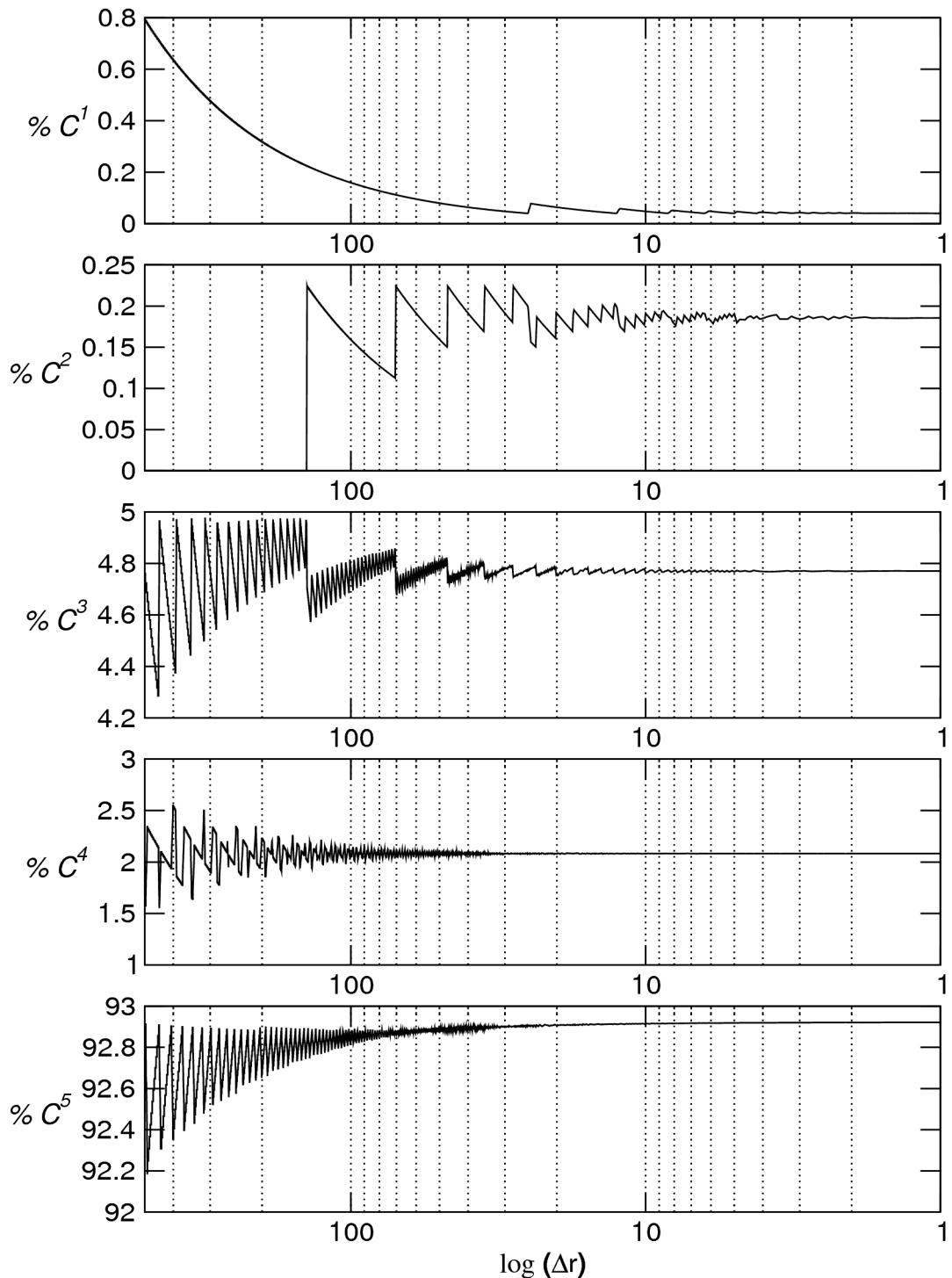


FIGURE 5.7 – Variation of the percentage of $IC^-(0.9)$ initial conditions in \mathcal{C}^k as a function of $\log(\Delta r)$, with $500 \text{ km} \leq \Delta r \leq 1 \text{ km}$.

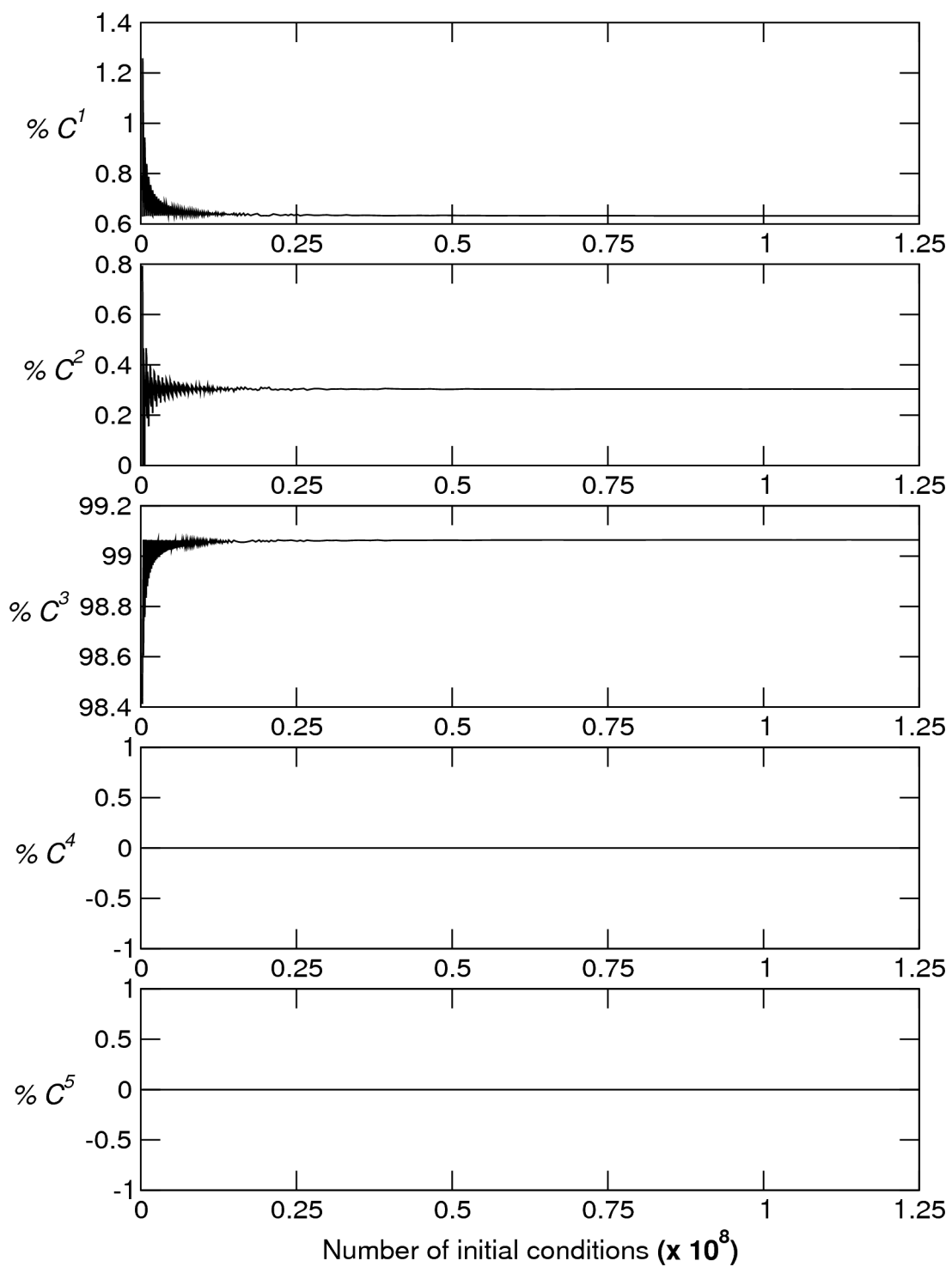


FIGURE 5.8 – Variation of the percentage of $IC^+(0.9)$ points in \mathcal{C}^k as a function of the number of initial conditions in $IC^+(0.9)$ as Δr varies from 500 km to 1 km.

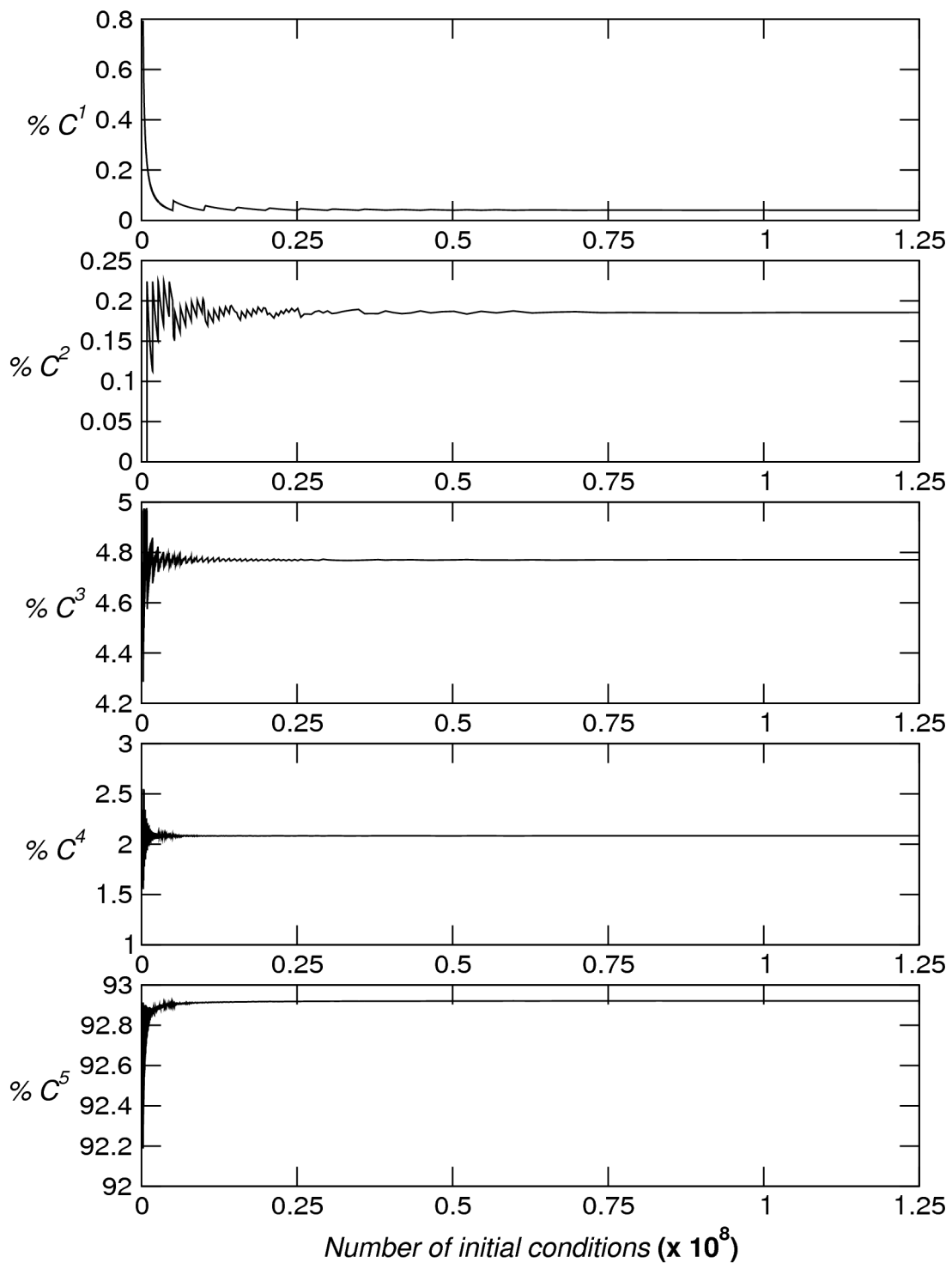


FIGURE 5.9 – Variation of the percentage of $IC^-(0.9)$ points in \mathcal{C}^k as a function of the number of initial conditions in $IC^-(0.9)$ as Δr varies from 500 km to 1 km.

to a specific set is very restricted. See, for example, subset \mathcal{C}^2 in Figures 5.3 and 5.4. Such a set may be poorly covered (or not covered at all) by a given radial variation as was observed for e ranging from approximately 0.6 to 0.92 in the case of positive initial velocity and e ranging from approximately 0.4 to 0.98 in the case of negative initial velocity.

In the lunar SOI, the classification according to the Jacobi constant does not depend significantly on $\Delta\theta$ due to the nearly radial symmetry of the effective potential.

5.3 Dynamical Investigation of Initial Condition Sets in the Lunar SOI

The WSB definition as proposed by E. Belbruno and stated in Ref. [8] does not give any information about the past behavior of the trajectories, since the classification of the IC^\pm sets is performed based only on the direct time integration ($t > t_0$) of the generated initial conditions. In this WSB context, Definitions 3 and 4 only contemplate part of the requirements for suitable ballistic transfer trajectories, i.e., capture orbits are given by initial conditions ($t = t_0 = 0$) that, under natural dynamics of the PCR3BP, take P_3 back to $l(\theta)$ with $h_K \leq 0$ at some $t_{f+} > t_0$. However, it should also be required that P_3 is at an appropriate location defined by some design strategy at some previous time $t_{f-} < t_0$.

Thus, our next analyses examine the trajectories generated as the initial conditions are integrated backwards ($t < t_0$) under the PCR3BP dynamics. They are based on the verification of the aforementioned retrograde requirement in light of two transport possibilities: (i) direct inner transfers and (ii) external transfers based on a patched three-body approach, although alternative four-body approaches could be considered.

We establish two sets of criteria, displayed in Figure 5.10.

Criteria for direct inner transfers: For direct inner transfer applications, as the initial conditions are integrated backwards, we test if: (i) trajectories enter a closed disk

B_1 of radius $r_{B1} = 80,000$ km around the Earth in the x - y plane; (ii) trajectories enter a closed disk B_2 of radius $r_{B2} = 40,000$ km around the Earth in the x - y plane. We mark the times t^{B1} and t^{B2} at which each criterion is satisfied.

These criteria were chosen in order to seek trajectories that, considering the time reversibility of this dynamical system, for $t < 0$, go into the Earth realm and approach that primary enough to obtain typical parking orbits through adequate circularization of the three-body solution. Usual parking orbits, consistent with currently existing infrastructure are Low Earth Orbits (LEO), Geostationary Earth Orbits (GEO), and GEO Transfer Orbits (GTO) [33].

Criteria for external transfers: Let ϕ be the counterclockwise angle formed by the radial line passing through the position of P_1 and the x -axis, with $x > \mu$ and let Σ be the Poincaré section defined by the angle ϕ , $\dot{x} > 0$ and $r_1 = [(x - \mu)^2 + y^2]^{1/2} > r_S$, where $r_S = 0.9928$ is the distance between the Earth and the Lagrangian point L_3 of the EM-system. For external transfers, we verify which trajectories cross the Poincaré sections Σ_i , $i = 1,2,3,4,5$ determined by the angles $\phi_1 = 195^\circ$, $\phi_2 = 210^\circ$, $\phi_3 = 225^\circ$, $\phi_4 = 240^\circ$, and $\phi_5 = 275^\circ$. The instants at which each criterion is satisfied are denoted by $t^{\Sigma i}$, $i = 1,2,3,4,5$.

The choice of the sections is related to different initial configurations of the EM-system relative to the SE-system in a patched three-body construction. The $r_1 > r_S$ restriction is essential in order to take advantage of the transport channels provided by the invariant structures of the EM-system and of the SE-system. With this requirement, P_3 will cross the Poincaré section in the exterior realm of the EM-system, where the stable manifold of a L_2 EM-Lyapunov orbit intersects the unstable manifold of a L_1 (or L_2) SE-Lyapunov

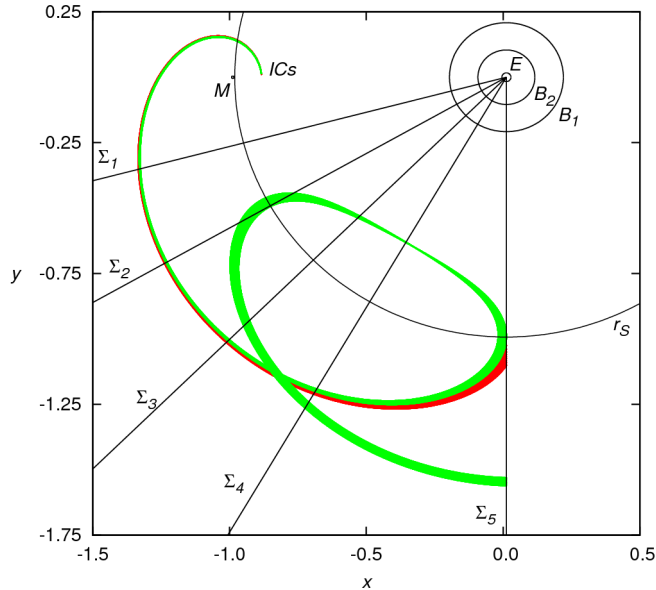


FIGURE 5.10 – Criteria for direct inner transfers and for external transfers in the patched three-body approach. The boundaries of the circular disks B_1 and B_2 and the projections onto the x - y of the sections Σ_i are shown. The curve labeled as r_S depicts the boundary of a region around the Earth with radius equal to the distance from the Earth to L_3 of the EM-system. The label ICs indicates the x - y projections of the initial conditions of the red and green bunches of trajectories.

orbit.

By using the presented geometrical criteria for the prior dynamical evolution, we classify trajectories according to a certain measure of employability. As an example, we display in Figure 5.10 the projections of two bunches of trajectories (red and green) that start at nearby initial conditions and behave quite similarly for a considerable interval of time. Through the performed analysis of applicability, we detect that the red bunch of trajectories is more adequate for a patching procedure at section Σ_5 than the green bunch of trajectories, given that the first bunch crosses that section at an earlier time.

For the retrograde analyses, the maximum time interval, Δt_{max} , for the numerical integration was set to be equal to 6 months.

5.3.1 Retrograde Analyses for Direct Inner Transfers

Figures 5.11 and 5.12 display the results of the retrograde analysis regarding applicability in direct inner transfers of the sets of initial conditions with positive and negative initial velocity, respectively, for (a) $e = 0.6$ and (b) $e = 0.9$.

In these figures, we identify the spatial distribution of the few candidates for this kind of transfer. For $e = 0.6$, we see that trajectories that reach B_2 start at inadequate altitudes for typical final selenocentric orbits. As the eccentricity increases, candidate trajectories appear at lower altitudes. The amount of trajectories that reach B_2 is always very small. Also, from the color code, we see that the time intervals until B_2 is reached is very long. These results are quantified in Table 5.2.

Although the $IC^+(e)$ sets present a slightly larger number of candidates for inner transfers, the minimum flight time interval differs considerably among the sets and the best ones are found in the $IC^-(e)$ sets. Nonetheless, even for the best cases, the time of flight until criterion (ii) is satisfied is usually quite long. This means that the generated sets of initial conditions are inefficient for direct inner transfers both in view of time adequacy and with respect to the amount of applicable solutions.

Actually, the lack of feasible direct inner trajectories is to be expected in the considered mathematical model due to the existence of an invariant torus which prevents the proximity of P_3 to the largest primary, in such a way that it is impossible for the particle to pass from a region arbitrarily close to the Moon to a region arbitrarily close to the Earth. The existence of this torus that blocks the approach of P_3 was shown by R. McGehee [34] and is discussed in some detail in Ref. [13].

As an example of this feature, consider the Poincaré section II through $\dot{x} = 0$ with $\dot{y} > 0$ for $C = 3.06734276$. This value of the Jacobi constant corresponds to the energy

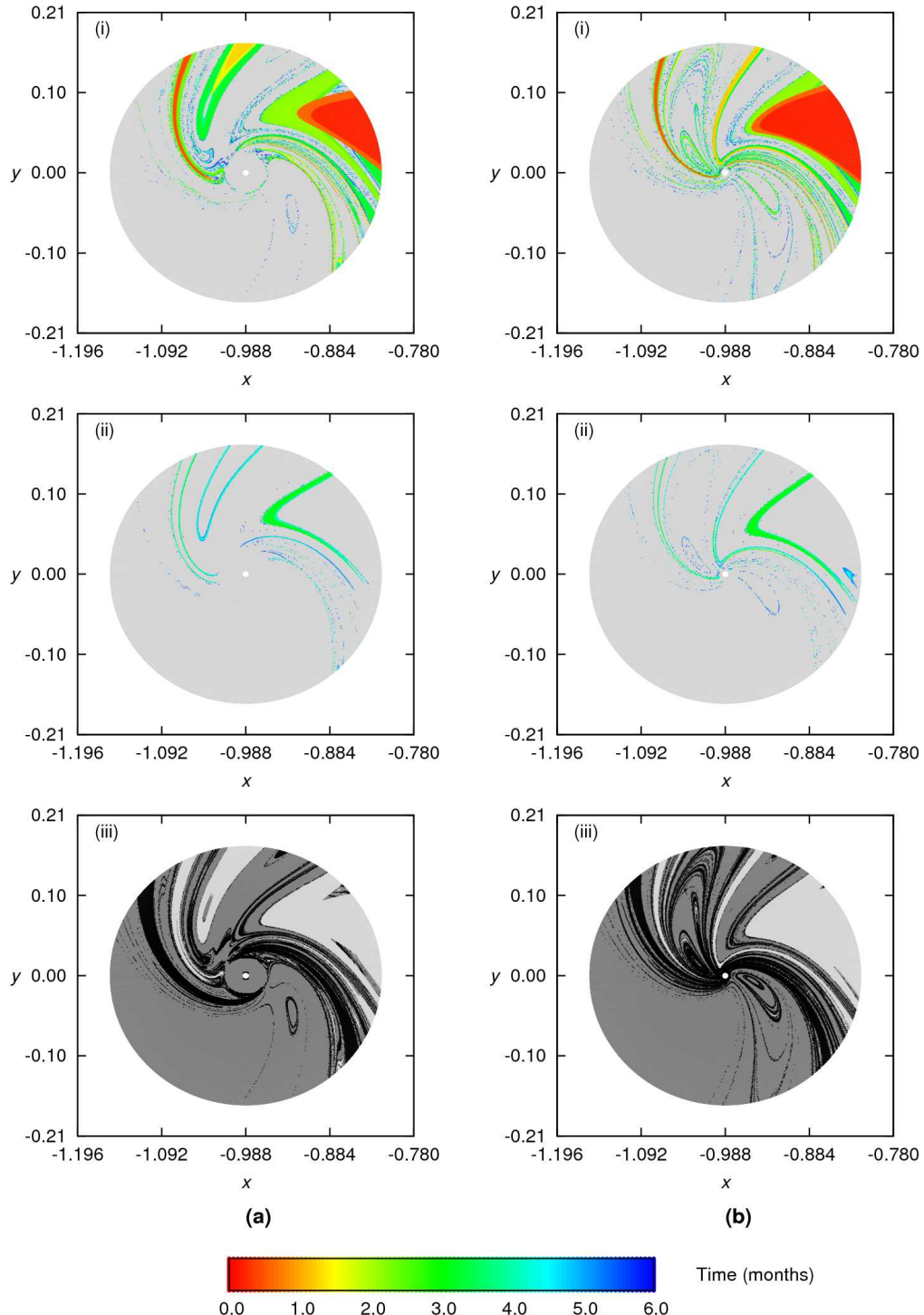


FIGURE 5.11 – Retrograde analysis regarding application in direct inner transfers for (a) $IC^+(0.6)$ and (b) $IC^+(0.9)$: (i) Trajectories that reach B_1 ; (ii) Trajectories that reach B_2 . In the plots, the colors represent the time of flight until each criterion is fulfilled. (iii) Collisional orbits (black) and trajectories which do not satisfy any of the established criteria (dark grey). In all frames the light grey points represent the complementary set of initial conditions.

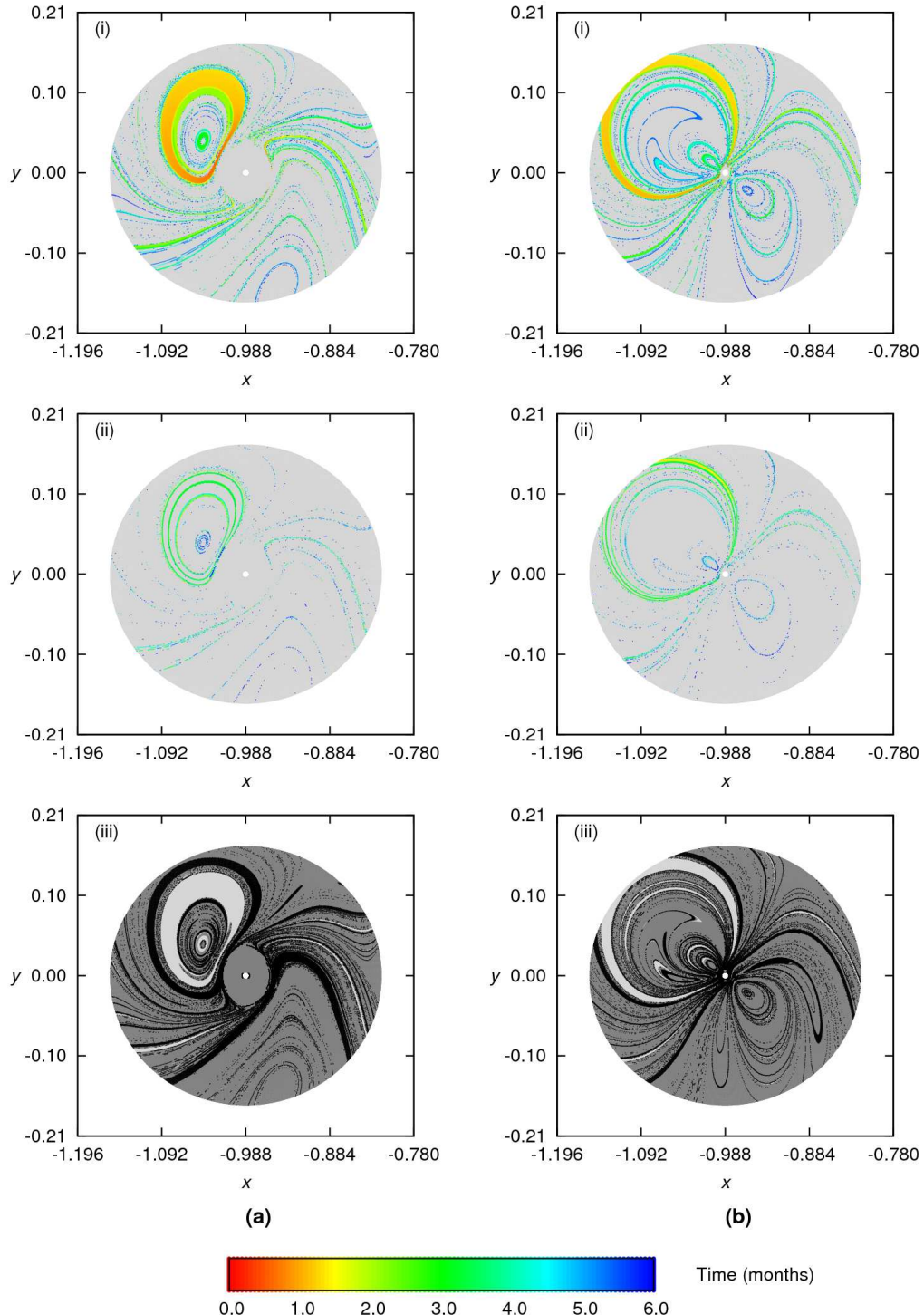


FIGURE 5.12 – Retrograde analysis regarding application in direct inner transfers for (a) $IC^-(0.6)$ and (b) $IC^-(0.9)$: (i) Trajectories that reach B_1 ; (ii) Trajectories that reach B_2 . In the plots, the colors represent the time of flight until each criterion is fulfilled. (iii) Collisional orbits (black) and trajectories which do not satisfy any of the established criteria (dark grey). In all frames the light grey points represent the complementary set of initial conditions.

	B_1 %	B_2 %	Collision %	None %	Δt_{min} (days)	Δt_{mean} (days)
$IC^+(0.6)$	15.17	2.44 (16.08)	12.69	72.14	86.0	104.8
$IC^+(0.9)$	15.29	2.53 (16.55)	14.77	69.94	59.8	101.4
$IC^-(0.6)$	10.21	1.49 (14.50)	16.87	72.91	50.9	104.1
$IC^-(0.9)$	9.49	1.84 (19.36)	13.60	76.91	35.8	100.5

TABLE 5.2 – Retrograde analysis of the complete sets of initial conditions for application in direct inner transfers. In the first four columns, the values pertain to the percentage of initial conditions that behave according to each criteria relative to the total number of initial conditions in the sets $IC^\pm(e)$. The numbers in parenthesis refer to the percentage of trajectories that enter B_2 relative to the total number of trajectories that enter B_1 . The fifth and sixth columns display, respectively, the minimum and the mean flight time (in days) to enter sphere B_2 .

level of the stable initial condition with positive initial velocity ic_1 with $e = 0.9$ for which the time of flight until criterion (ii) is satisfied is minimum in the stable subset of $IC^+(0.9)$.

In Figure 5.13 we display the Poincaré iterates on the x - y plane of several initial conditions integrated for 2×10^4 dimensionless time units, along with the 35 Poincaré iterates of the trajectory generated by ic_1 , integrated backwards during 75.4 dimensionless time units (nearly one year). In this interval of time, the minimum distance of P_3 from Earth, r_1^{min} , was 34,072.9 km, achieved after 25.2 dimensionless units of time or approximately 109.4 days.

From the Poincaré section, we see that the phase space is extremely intermixed, presenting large periodic islands interspersed with regions of chaotic motion. Figure 5.14 shows a detail of the B_2 region around the Earth, where we can clearly see a barrier of quasiperiodic orbits preventing P_3 from approaching P_1 .

We note that, for this particular trajectory, the minimum distance between P_3 and P_1 slightly decreases if longer integration time is considered. Also, as higher energy levels are considered, P_3 can further approach the Earth. This is the case, for example, of the stable initial condition with negative initial velocity ic_2 with $e = 0.95$ and $C = 2.88681599$. The

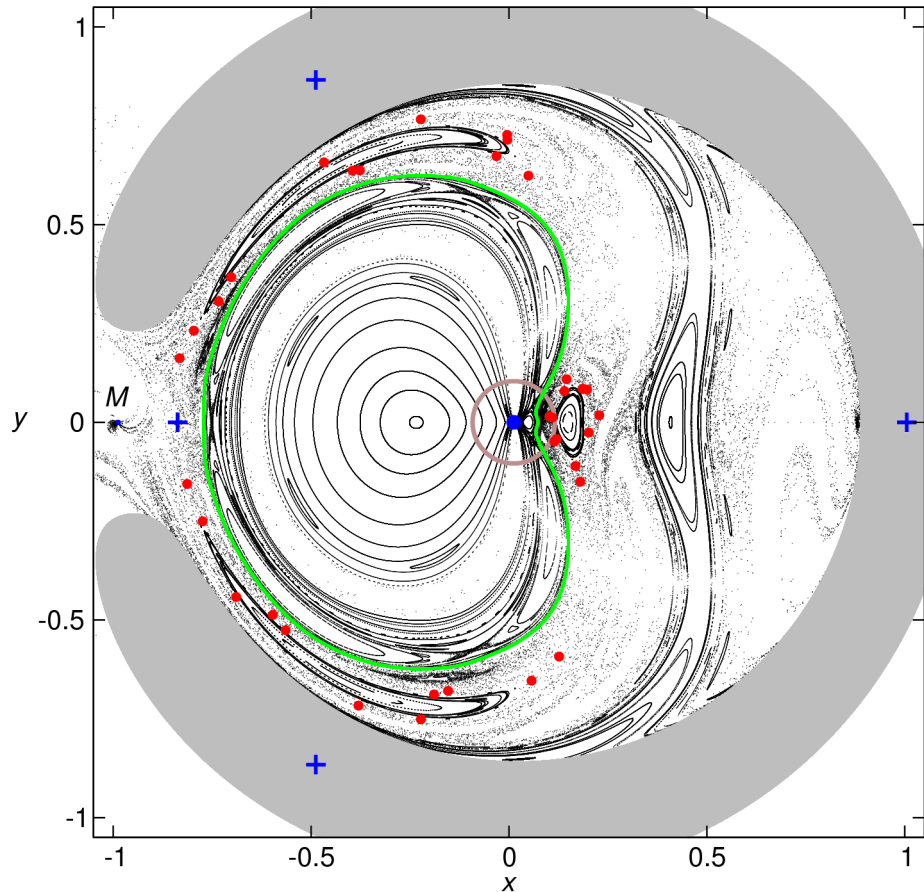


FIGURE 5.13 – Poincaré section $\dot{x} = 0$, $\dot{y} > 0$ for $C = 3.06734276$. We display the Poincaré iterates on the x - y plane of several initial conditions that were integrated for 2×10^4 dimensionless units of time. The red dots in the chaotic region are the 35 Poincaré iterates of the trajectory generated by initial condition ic_1 integrated backwards during approximately 75 dimensionless units. The primaries are represented by blue balls and four equilibrium points are shown as blue crosses. The green dots account for the Poincaré iterates of the trajectory that represents the last torus of the large stable island around the Earth. The brown curve delimits the B_2 region around the Earth with radius of 40,000 km. The grey area represents the forbidden region.

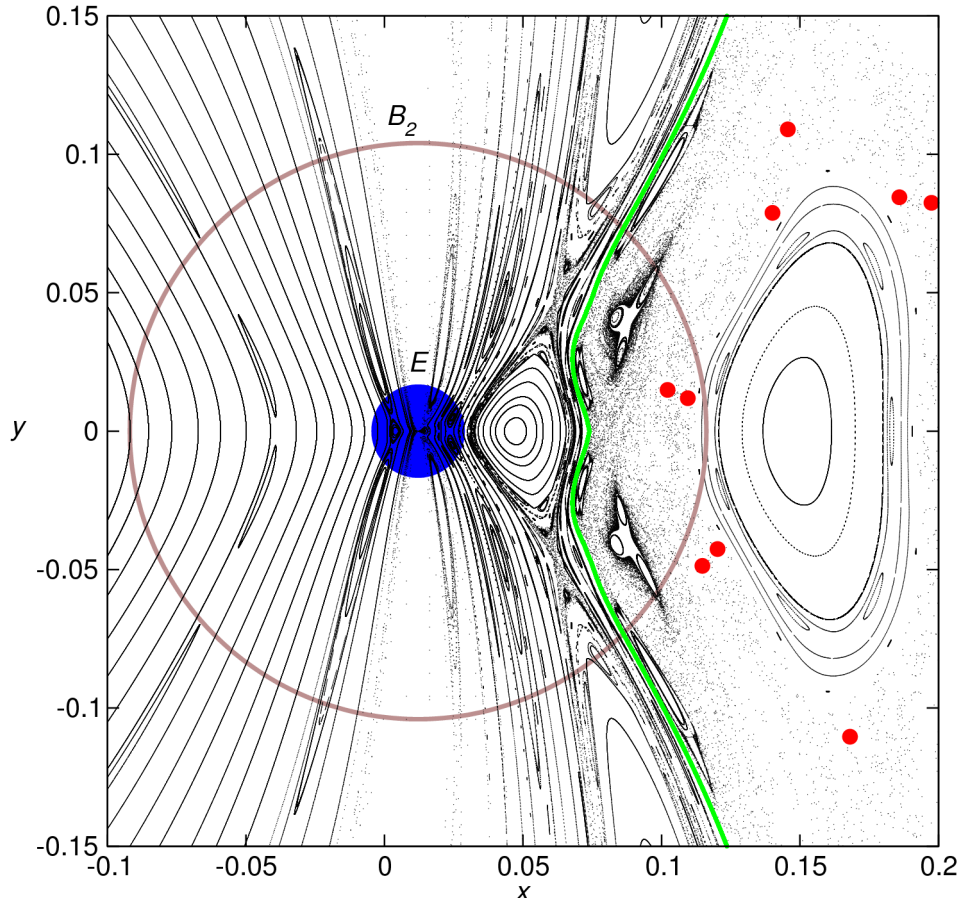


FIGURE 5.14 – Poincaré section $\dot{x} = 0$, $\dot{y} > 0$ for $C = 3.06734276$. We display a detail of the B_2 region (see Figure 5.13) around the Earth. The red dots in the chaotic sea are the Poincaré iterates of the trajectory generated by initial condition ic_1 . Here we can clearly see a barrier of quasiperiodic trajectories preventing P_3 from approaching P_1 . The green curve connects the Poincaré iterates of the trajectory that represents the last torus of the large stable island. The Earth is represented by a blue ball and the brown curve delimits the B_2 region with radius of 40,000 km around the primary.

	ic_1	ic_2
Stable set, $e = 0.9$	Stable set, $e = 0.95$	
Positive initial velocity	Negative initial velocity	
$C = 3.06734276$ (3)	$C = 2.88681599$ (5)	
x_0	-0.929846	-1.134481
y_0	0.047373	0.004147
\dot{x}_0	-0.303840	0.015508
\dot{y}_0	0.372014	0.548369
T	75.4	376.9
r_1^{min}	34,072.9	29,572.8
t_1^{min}	25.2	176.7
#	35	141
		11

TABLE 5.3 – Specific information of the trajectories generated by ic_1 and ic_2 . For the first initial condition, two experiments are displayed in which two different maximum integration times are considered. In the table, x_0 , y_0 , \dot{x}_0 and \dot{y}_0 refer to the initial conditions, T is the integration time (in dimensionless units), r_1^{min} is the minimum distance of P_3 from P_1 (in km), achieved at time t_1^{min} and # accounts for the number of Poincaré iterates on section Π . The numbers in parenthesis refer to the \mathcal{C}^i set of the classification according to the Jacobi constant value.

minimum distance from P_3 to the Earth is achieved after 27.2 dimensionless time units, or approximately 118.3 days. This particular trajectory approaches the Earth and crosses the Π plane 11 times before returning to the lunar region and colliding with the Moon after 56.4 dimensionless units of time. For the sake of comparison, we display some specific information of the trajectories generated by ic_1 and ic_2 in Table 5.3.

5.3.2 Retrograde Analyses for External Transfers

The results of the retrograde analysis of the sets $IC^+(0.6)$ and $IC^+(0.9)$ for application in external transfers are displayed in Figures 5.15 and 5.16, respectively, while Figures 5.17 and 5.18 show the results for the sets $IC^-(0.6)$ and $IC^-(0.9)$.

We find that, for the sets of initial conditions with positive initial velocity, the subsets of trajectories which cross Σ_i , $i = 1,2,3,4,5$, in a short interval of time do not change considerably with i . Conversely, for the sets of initial conditions with negative initial

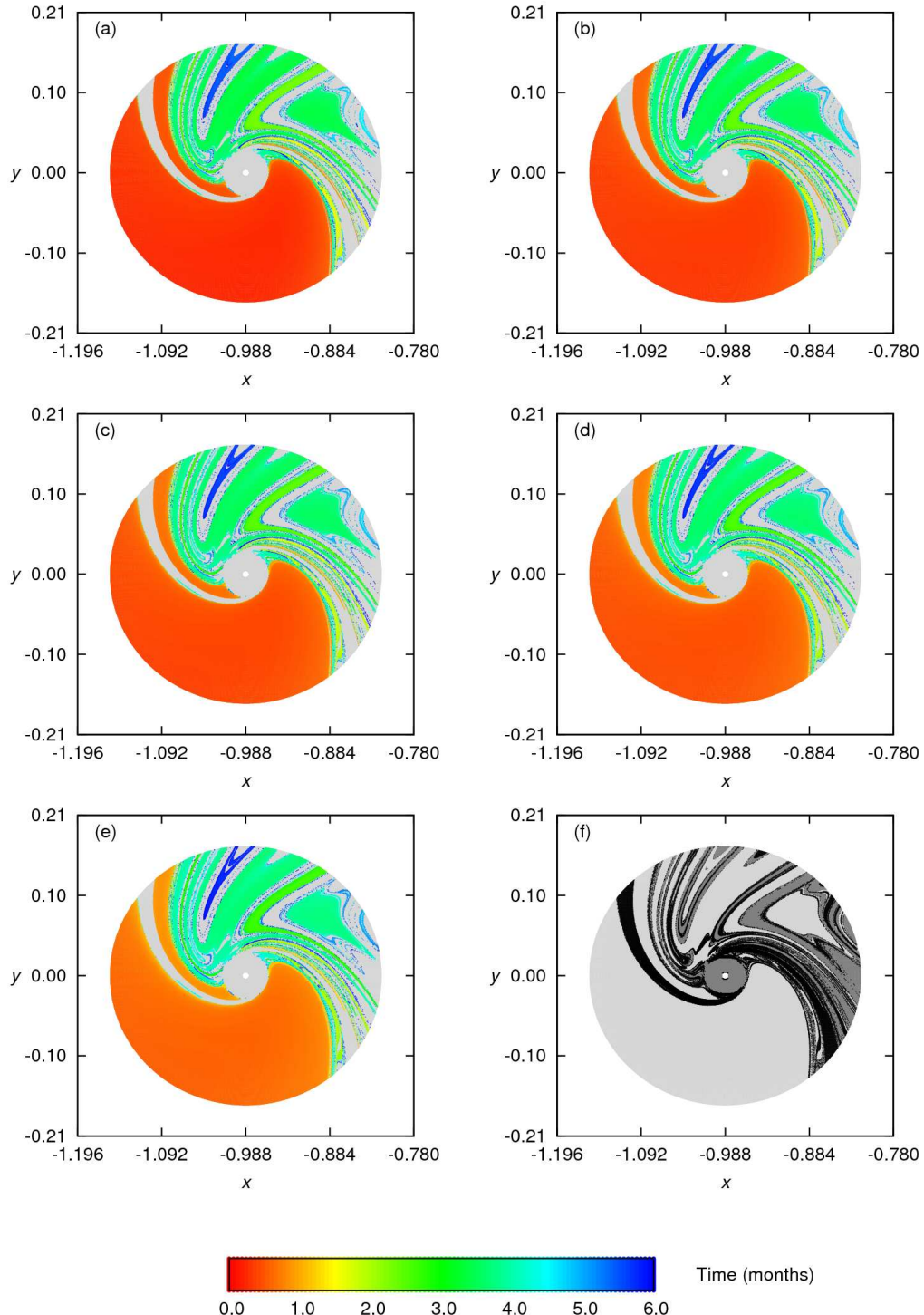


FIGURE 5.15 – Retrograde analysis regarding application in external transfers for $IC^+(0.6)$. Frames (a) to (e): Initial conditions which generate trajectories that cross each Σ_i section, $i = 1,2,3,4,5$. In the plots, the colors represent the time of flight until each criterion is fulfilled. Frame (f): Collision (black) or none of the established criteria are satisfied (dark grey). In all frames the light grey points represent the complementary set of initial conditions.

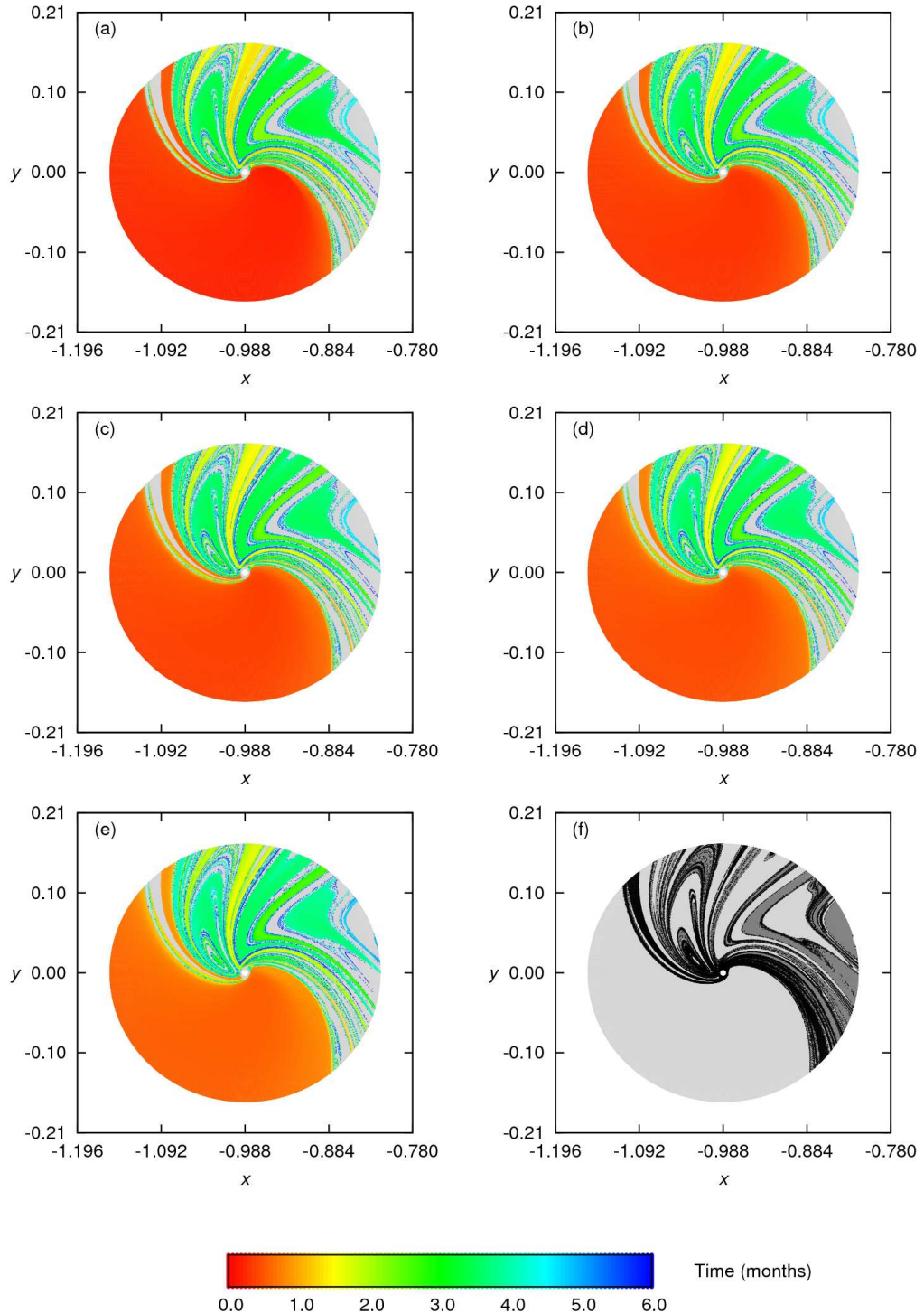


FIGURE 5.16 – Retrograde analysis regarding application in external transfers for $IC^+(0.9)$. Frames (a) to (e): Initial conditions which generate trajectories that cross each Σ_i section, $i = 1,2,3,4,5$. In the plots, the colors represent the time of flight until each criterion is fulfilled. Frame (f): Collision (black) or none of the established criteria are satisfied (dark grey). In all frames the light grey points represent the complementary set of initial conditions.

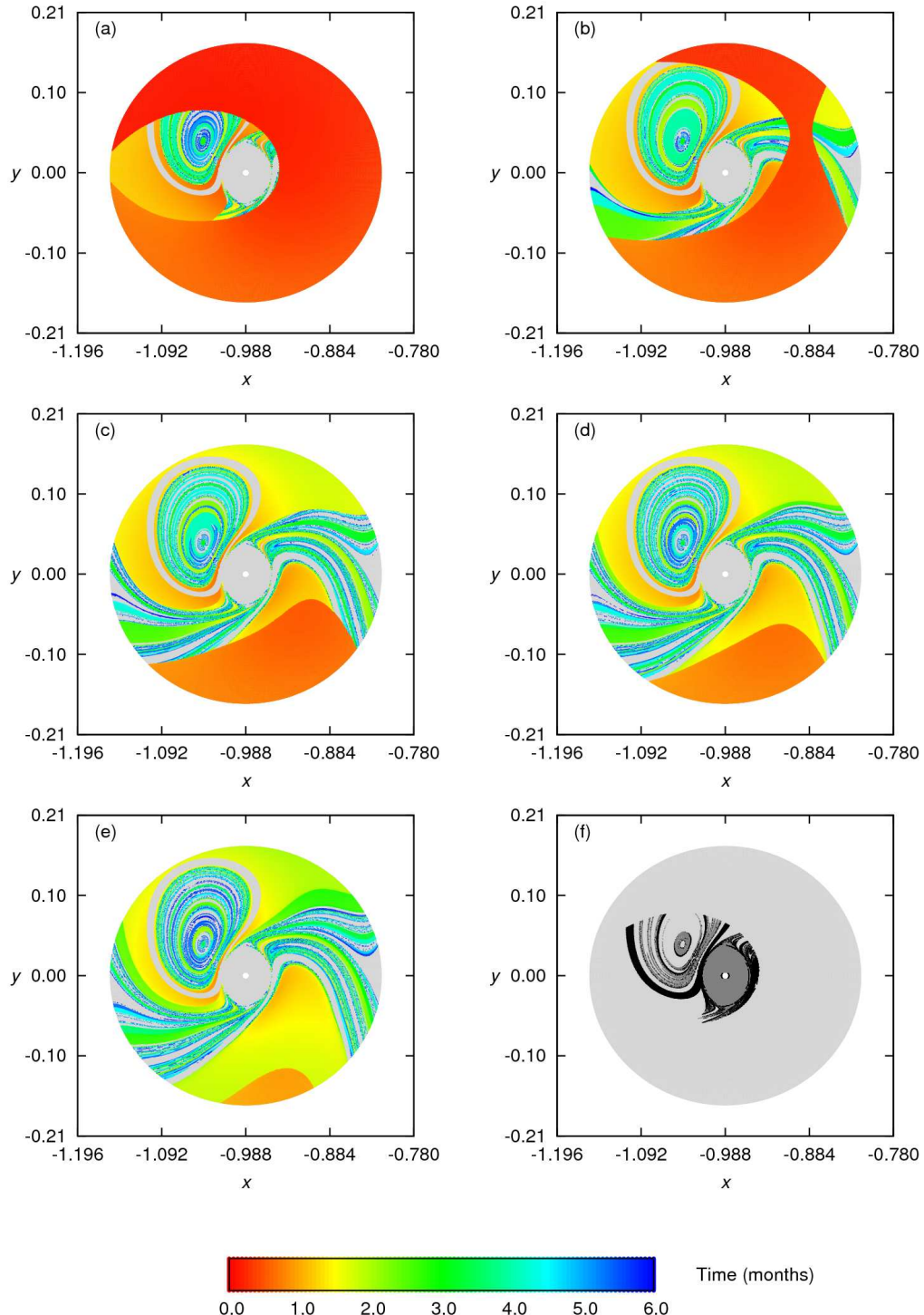


FIGURE 5.17 – Retrograde analysis regarding application in external transfers for $IC^-(0.6)$. Frames (a) to (e): Initial conditions which generate trajectories that cross each Σ_i section, $i = 1,2,3,4,5$. In the plots, the colors represent the time of flight until each criterion is fulfilled. Frame (f): Collision (black) or none of the established criteria are satisfied (dark grey). In all frames the light grey points represent the complementary set of initial conditions.

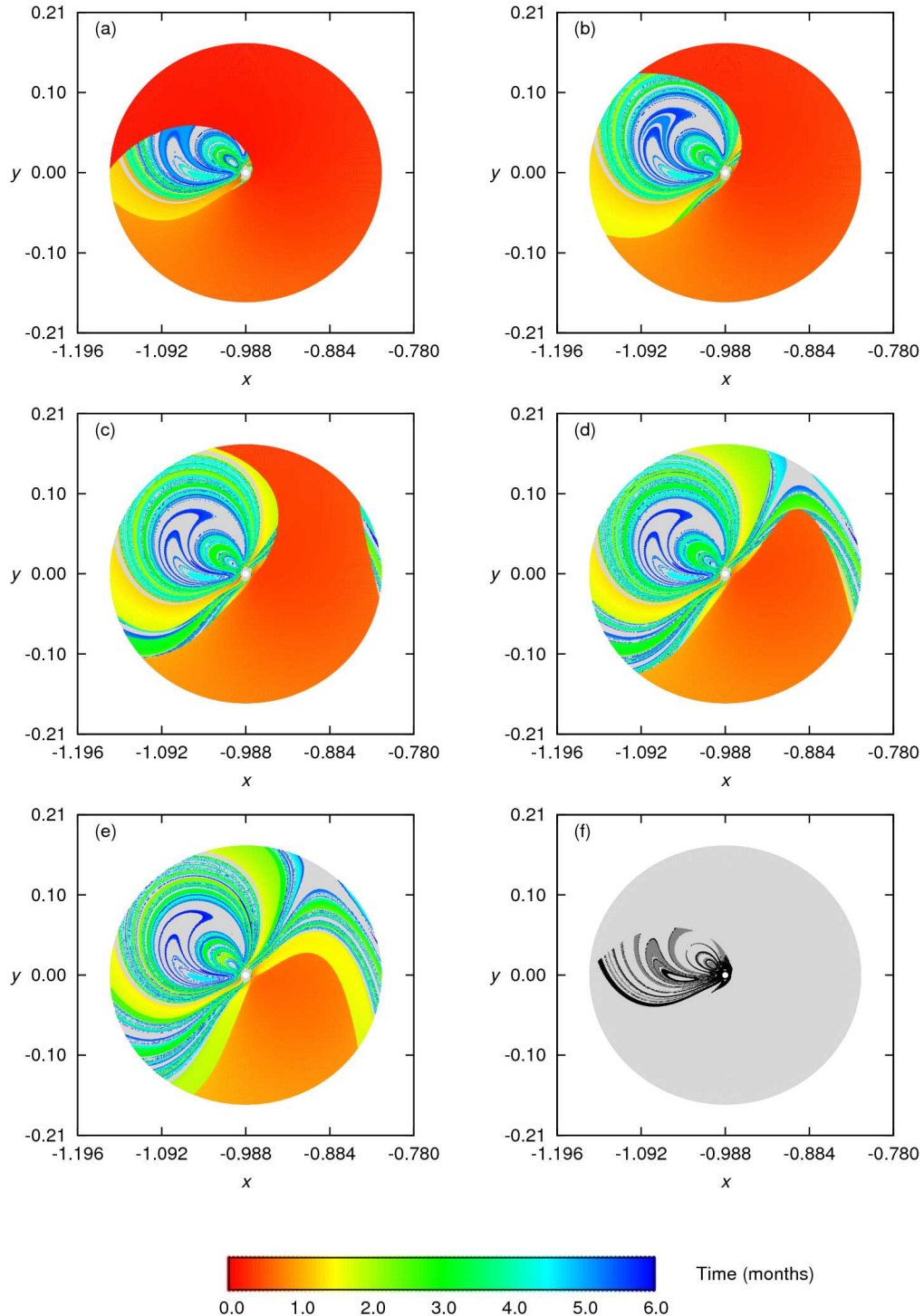


FIGURE 5.18 – Retrograde analysis regarding application in external transfers for $IC^-(0.9)$. Frames (a) to (e): Initial conditions which generate trajectories that cross each Σ_i section, $i = 1,2,3,4,5$. In the plots, the colors represent the time of flight until each criterion is fulfilled. Frame (f): Collision (black) or none of the established criteria are satisfied (dark grey). In all frames the light grey points represent the complementary set of initial conditions.

	Σ_1 %	Σ_2 %	Σ_3 %	Σ_4 %	Σ_5 %	Collision %	None %
$IC^+(0.6)$	59.61	59.53	59.46	59.40	59.28	13.59	26.78
$IC^+(0.9)$	72.26	72.17	72.10	72.04	71.92	14.13	13.59
$IC^-(0.6)$	71.45	63.67	53.57	50.80	49.43	5.85	20.72
$IC^-(0.9)$	86.88	79.81	76.05	70.70	66.53	4.28	5.08

TABLE 5.4 – Retrograde analysis for application in external transfers. The values pertain to the percentage of initial conditions that behave according to each criteria relative to the total number of initial conditions in each $IC^\pm(e)$ set.

velocity, these subsets are large for Σ_1 , and diminish considerably for the subsequent sections. The sharp boundaries between subsets of small and long flight time are defined due to the r_1 threshold which delimits the external region of the patching procedure. Both in the cases of positive and negative initial velocities, collisional orbits are restricted to the regions of initial conditions that generate trajectories with longer flight time.

As seen in Table 5.4 for the sets $IC^\pm(0.6)$ and $IC^\pm(0.9)$, the employability of the Σ_i sections diminishes as ϕ departs from 180° to 270° for fixed e , regarding the amount of orbits that cross each section. Also, the sets of orbits which collide with the Moon and the set of the trajectories that do not fulfill any of the criteria in Δt_{max} are more expressive in the case of positive initial velocity.

As for the time of flight, the best trajectories take only a few days to reach Σ_1 , but this time increases considerably in the case of Σ_5 , especially in the case of initial conditions with negative initial velocity, as seen in Table 5.5. Also, the minimum time it takes for the trajectories to cross a Σ_i section decreases as e increases. In all cases, the mean flight time is much longer than the minimum values.

As expected, for external transfers based on a patched three-body approach, the generated sets provide candidate initial conditions for several configurations of the initial Sun-Earth-Moon system setup. It is important to tune the initial spatial configuration

	Σ_1	Σ_2	Σ_3	Σ_4	Σ_5
Minimum flight time (days)					
$IC^+(0.6)$	5.95	8.51	10.39	12.05	15.04
$IC^+(0.9)$	4.55	7.91	9.96	11.69	14.67
$IC^-(0.6)$	3.48	7.05	14.10	17.70	24.02
$IC^-(0.9)$	3.11	6.50	9.42	11.91	15.75
Mean flight time (days)					
$IC^+(0.6)$	36.49	38.85	40.69	42.35	45.27
$IC^+(0.9)$	32.11	34.88	36.86	38.60	41.71
$IC^-(0.6)$	19.22	40.12	52.19	56.89	63.48
$IC^-(0.9)$	20.68	31.31	38.62	47.65	53.28

TABLE 5.5 – Time performance of trajectories generated by initial conditions in $IC^\pm(e)$ that cross each Σ_i , $i = 1, 2, 3, 4, 5$ section for application in external transfers.

of the EM-system with respect to the SE-system correctly in order to decrease the flight time and increase the number of candidate solutions. For a given initial configuration, high eccentricities usually provide more candidates and the shortest flight time intervals.

Since this analysis does not distinguish between trajectories that are stable and unstable according to Definition 4, the applicability of the candidate solutions as ballistic capture trajectories is conditioned to the prograde classification procedure. For all the unstable ones, the applicability is restricted to their stabilization at the initial conditions by means of impulsive maneuvers.

5.4 Investigation of the Stable Set in the Lunar SOI

The next analyses deal with the characterization of the stable sets in the lunar SOI, given that they refer to ballistically captured states according to Definition 3. Initially we will focus on the stable sets obtained through implementation A (Sections 5.4.1 and 5.4.2), then we continue with the stable sets obtained through implementation B (Sections 5.4.3 and 5.4.4). We will denote the stable sets by $\mathcal{S}^\pm(e)$, where \pm refers to initial conditions

	Implementation A		Implementation B	
	N	% of IC	N	% of IC
$\mathcal{S}^+(0.0)$	252,139	60.00	241,342	57.43
$\mathcal{S}^+(0.6)$	95,966	22.83	76,943	18.31
$\mathcal{S}^+(0.9)$	32,822	7.81	18,358	4.36
$\mathcal{S}^+(0.95)$	23,505	5.59	14,205	3.38
$\mathcal{S}^-(0.0)$	417,847	99.43	417,847	99.43
$\mathcal{S}^-(0.6)$	190,429	45.31	185,826	44.22
$\mathcal{S}^-(0.9)$	53,123	12.64	47,655	11.34
$\mathcal{S}^-(0.95)$	39,257	9.34	38,198	9.09

TABLE 5.6 – Number (N) of stable initial conditions in the lunar SOI with positive and negative initial velocities for implementations A and B. The second and the fourth columns refer to the percentage with respect to the corresponding full sets $IC^\pm(e)$.

with positive and negative initial velocity.

The number of initial conditions that belong to the stable sets is presented in Table 5.6 for the cases of $e = 0.0, 0.6, 0.9$, and 0.95 , both for implementation A and for implementation B. The percentage with respect to the corresponding full set of initial conditions is also presented.

5.4.1 Retrograde Analyses of the Stable Set

Application in direct inner transfers:

The results of the retrograde analysis for application in direct inner transfers of the sets $\mathcal{S}^\pm(e)$ obtained through implementation A for $e = 0.0, 0.6, 0.9$, and 0.95 , are presented in Table 5.7. The relative quantities of stable initial conditions candidate for inner transfers are even smaller than the relative quantities of the complete set for all eccentricity values.

In the case of $\mathcal{S}^+(e)$, the relative amount of points that satisfy criteria (i) and (ii) tend to increase as e increases, although the absolute number of potentially applicable points remains very small for all eccentricities. The minimum flight time, Δt_{min} , to enter sphere B_2 diminishes slightly as e increases.

	B_1 %	B_2 %	Collision %	None %	Δt_{min} (days)	Δt_{mean} (days)
$\mathcal{S}^+(0.0)$	2.50	0.07 (2.85)	5.74	91.74	87.9	104.2
$\mathcal{S}^+(0.6)$	4.69	0.34 (7.32)	13.08	82.22	86.3	109.2
$\mathcal{S}^+(0.9)$	13.30	1.07 (8.10)	30.32	56.36	85.1	104.8
$\mathcal{S}^+(0.95)$	16.67	1.34 (8.08)	12.47	70.84	69.3	101.8
$\mathcal{S}^-(0.0)$	1.81	0.16 (9.17)	5.01	93.17	80.3	129.4
$\mathcal{S}^-(0.6)$	7.58	1.07 (14.21)	14.16	78.24	51.9	106.3
$\mathcal{S}^-(0.9)$	5.59	0.44 (8.04)	21.62	72.78	57.4	139.3
$\mathcal{S}^-(0.95)$	5.12	0.70 (13.77)	9.48	85.39	84.9	134.1

TABLE 5.7 – Retrograde analysis of stable initial conditions obtained through implementation A for application in direct inner transfers. In the first four columns, the values pertain to the percentage of initial conditions that behave according to each criteria relative to the total number of initial conditions in the sets $\mathcal{S}^\pm(e)$. The numbers in parenthesis refer to the percentage of trajectories that enter B_2 relative to the total number of trajectories that enter B_1 . The fifth and sixth columns display, respectively, the minimum and the mean flight time (in days) to enter sphere B_2 .

For $\mathcal{S}^-(e)$, the behavior of the solutions is more diverse. For high eccentricity, the relative amount of possible applicable solutions with negative initial velocity is smaller than in the case of positive initial velocity, although it tends to increase with e for values above 0.9. The minimum intervals of time to fulfill criterion (ii) oscillate considerably.

Comparing with the results presented in Table 5.2, the results for the stable set are even more restrictive than for the corresponding complete sets of initial conditions. As for the flight time, the results remain nearly the same.

Although, the quantity of possible applicable solutions is very restricted in all cases considered, the $\mathcal{S}^-(e)$ sets appear to be slightly more favorable than the $\mathcal{S}^+(e)$ sets for low eccentricity, while the opposite is true when e is very high, typically over 0.9.

In Figures 5.19 and 5.20, we identify the spatial distribution of the few candidates for direct inner transfers. Also, the colors show that the time intervals until B_2 is reached are very long. Again, for low eccentricity values the trajectories that reach B_2 start at inadequate altitudes for typical final selenocentric orbits due to the stable core of quasiperiodic

	Σ_1 %	Σ_2 %	Σ_3 %	Σ_4 %	Σ_5 %	Collision %	None %
$\mathcal{S}^+(0.0)$	12.54	12.51	12.49	12.48	12.47	5.89	81.55
$\mathcal{S}^+(0.6)$	23.51	23.49	23.47	23.45	23.44	13.50	62.97
$\mathcal{S}^+(0.9)$	58.00	57.91	57.82	57.77	57.67	30.89	11.09
$\mathcal{S}^+(0.95)$	76.89	76.72	76.67	76.58	76.47	12.82	10.20
$\mathcal{S}^-(0.0)$	21.01	14.30	12.87	12.48	12.17	1.23	77.55
$\mathcal{S}^-(0.6)$	44.82	42.40	36.87	34.55	33.58	8.31	43.46
$\mathcal{S}^-(0.9)$	67.14	65.32	63.13	63.50	62.75	15.56	9.94
$\mathcal{S}^-(0.95)$	82.57	83.52	82.25	81.64	79.65	4.53	3.44

TABLE 5.8 – Retrograde analysis of stable initial conditions obtained through implementation A for application in external transfers. The values pertain to the percentage of initial conditions that behave according to each criteria relative to the total number of initial conditions in the sets $\mathcal{S}^\pm(e)$.

orbits around the primary. As the eccentricity increases, candidate trajectories appear at lower altitudes. The amount of trajectories that reach B_2 is always very small.

Application in external transfers based on a patched three-body approach:

For transfers based on a patched three-body approach, the results of the retrograde analysis of the stable subsets obtained through implementation A are displayed in Tables 5.8 and 5.9. For each Σ_i section, as e increases, the performance of candidate trajectories improves, both regarding the amount of orbits that cross the sections and the time of flight of such trajectories. For fixed e , the employability of the Σ_i sections diminishes slightly as ϕ departs from 180° to 270° and, usually, the stable sets with negative initial velocity are more favorable than the stable sets with positive initial velocity.

The results in Tables 5.8 and 5.9 can be compared with the ones in Tables 5.4 and 5.5. Contrary to what is expected, the percentage of stable candidate trajectories with respect to each $\mathcal{S}^\pm(e)$ set is considerably smaller than the percentage of candidate trajectories with respect to each $IC^\pm(e)$ set. That is, contrary to what is expected, the stable behavior produced by the stability classification of Definition 4 is often not related to transfer

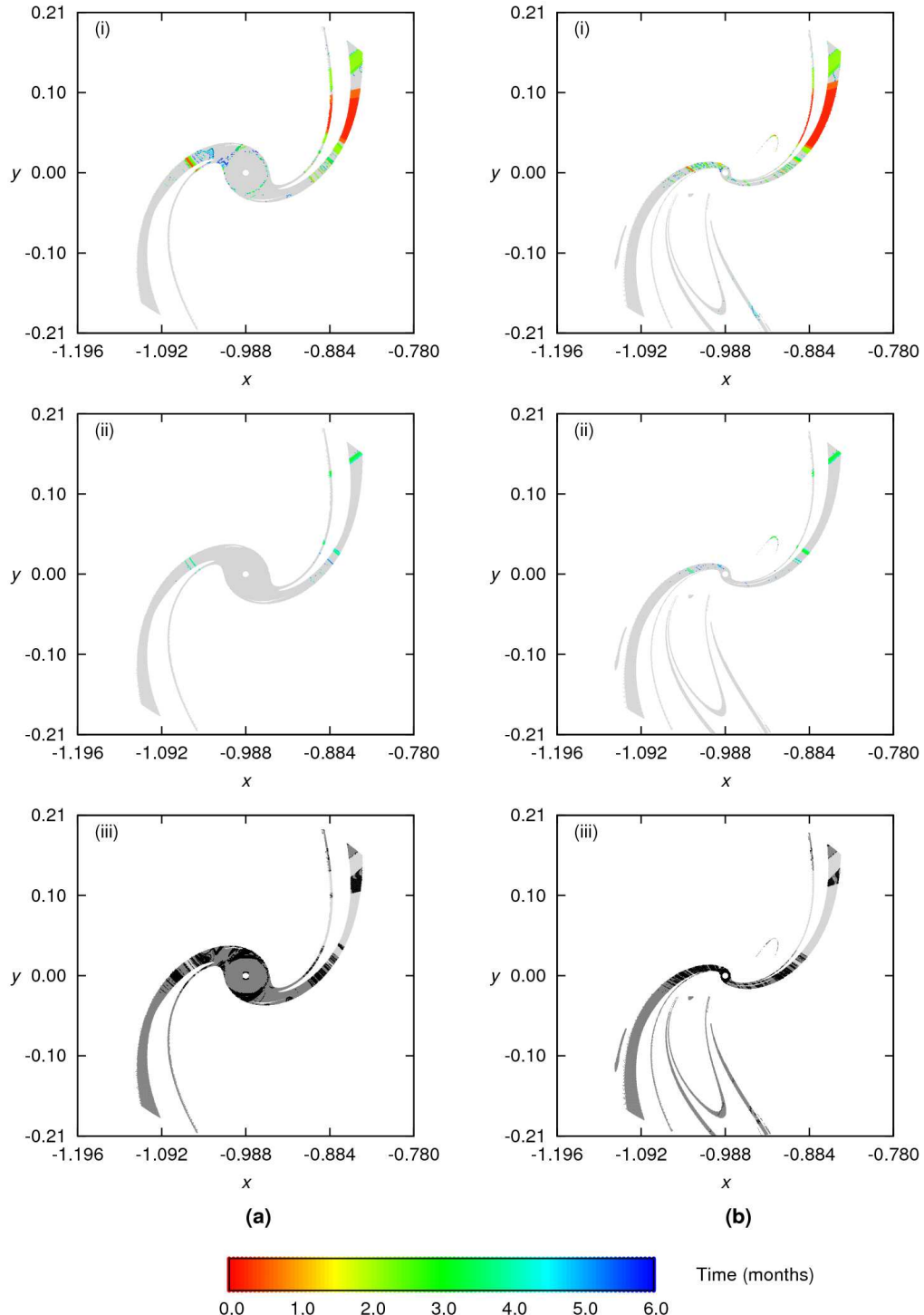


FIGURE 5.19 – Retrograde analysis regarding application in direct inner transfers for (a) $\mathcal{S}^+(0.6)$ and (b) $\mathcal{S}^+(0.9)$ obtained through implementation A: (i) Trajectories that reach B_1 ; (ii) Trajectories that reach B_2 . In the plots, the colors represent the time of flight until each criterion is fulfilled. (iii) Collisional orbits (black) and trajectories which do not satisfy any of the established criteria (dark grey). In all frames the light grey points represent the complementary set of initial conditions.

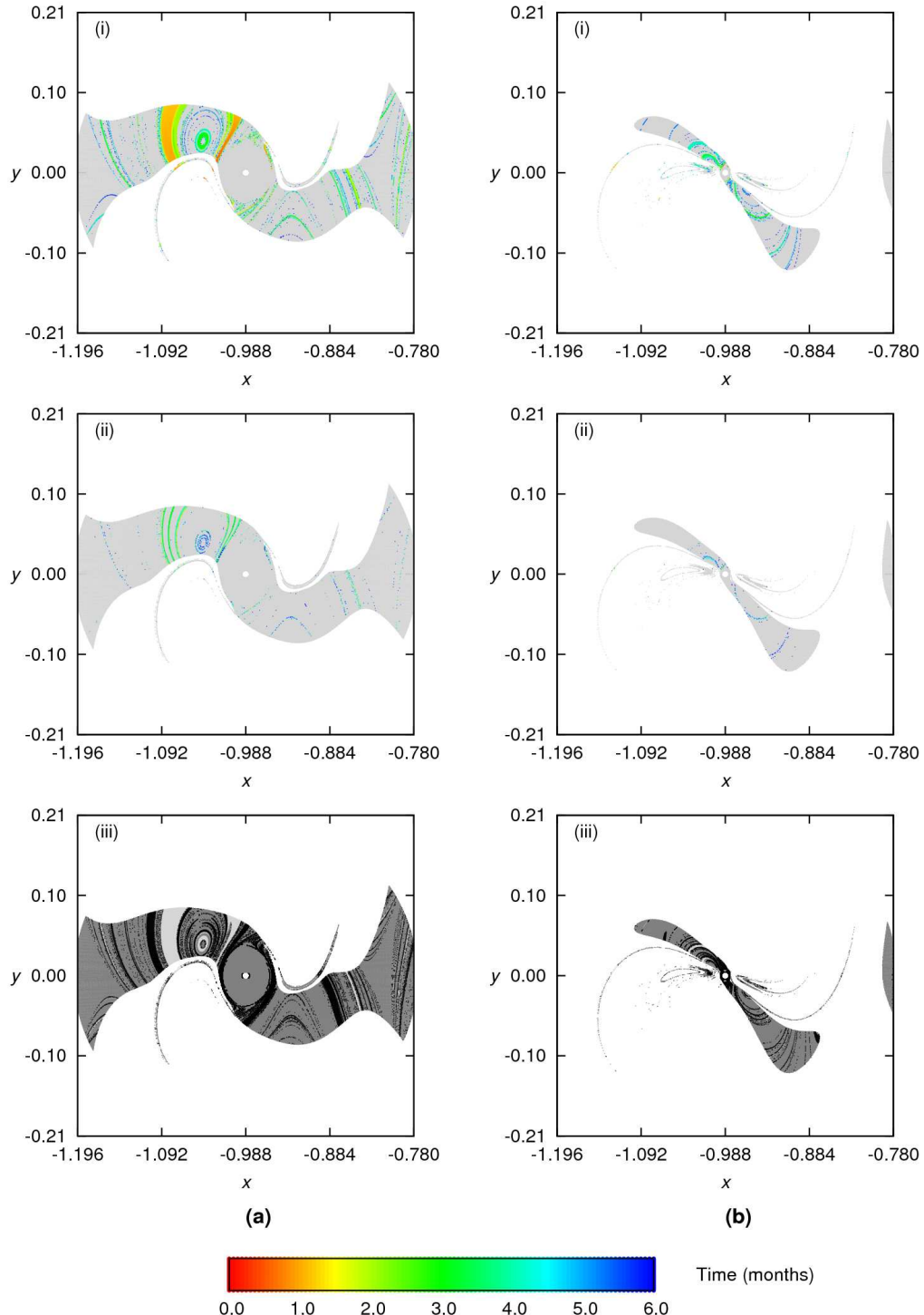


FIGURE 5.20 – Retrograde analysis regarding application in direct inner transfers for (a) $\mathcal{S}^-(0.6)$ and (b) $\mathcal{S}^-(0.9)$ obtained by implementation A: (i) Trajectories that reach B_1 ; (ii) Trajectories that reach B_2 . In the plots, the colors represent the time of flight until each criterion is fulfilled. (iii) Collisional orbits (black) and trajectories which do not satisfy any of the established criteria (dark grey). In all frames the light grey points represent the complementary set of initial conditions.

	Σ_1	Σ_2	Σ_3	Σ_4	Σ_5
Minimum flight time (days)					
$\mathcal{S}^+(0.0)$	7.35	9.73	11.58	13.25	16.26
$\mathcal{S}^+(0.6)$	6.06	8.51	10.40	12.07	15.07
$\mathcal{S}^+(0.9)$	4.63	7.92	10.03	11.69	14.68
$\mathcal{S}^+(0.95)$	3.75	7.50	9.62	11.44	14.62
$\mathcal{S}^-(0.0)$	4.52	16.73	20.68	23.04	27.59
$\mathcal{S}^-(0.6)$	3.48	9.99	14.10	17.70	24.28
$\mathcal{S}^-(0.9)$	3.23	7.71	9.93	11.98	15.76
$\mathcal{S}^-(0.95)$	3.16	7.56	9.65	11.53	15.02
Mean flight time (days)					
$\mathcal{S}^+(0.0)$	34.09	36.51	38.33	40.07	43.24
$\mathcal{S}^+(0.6)$	38.55	41.02	42.98	44.69	47.87
$\mathcal{S}^+(0.9)$	24.40	27.05	28.94	30.68	33.79
$\mathcal{S}^+(0.95)$	25.07	28.16	30.19	31.92	35.11
$\mathcal{S}^-(0.0)$	38.55	70.36	78.06	80.70	85.05
$\mathcal{S}^-(0.6)$	31.71	45.85	54.42	57.94	61.97
$\mathcal{S}^-(0.9)$	32.68	39.16	36.32	38.52	40.00
$\mathcal{S}^-(0.95)$	25.13	34.36	31.60	32.94	35.14

TABLE 5.9 – Time performance for application in external transfers of initial conditions in $\mathcal{S}^\pm(e)$ that cross each Σ_i , $i = 1, 2, 3, 4, 5$ section.

trajectories. This means that the chances of obtaining transfer trajectories is greater if the full sets of initial conditions are considered instead of the stable sets.

For illustration, the results of the retrograde analysis of the sets $\mathcal{S}^+(0.6)$ and $\mathcal{S}^+(0.9)$ for application in external transfers are displayed in Figures 5.21 and 5.22, respectively, while Figures 5.23 and 5.24 show the results for the sets $\mathcal{S}^-(0.6)$ and $\mathcal{S}^-(0.9)$. As seen for $e = 0.6$, a stable core of quasiperiodic trajectories that is unsuited for transfers prevails for low eccentricity values. Thus, the spatial distribution of the applicable solutions justifies the necessity of high eccentricity values in order to obtain feasible transfer orbits.

The stable sets $\mathcal{S}^\pm(e)$ are obtained by associating an analytical criterion to a geometrical criterion, namely, the measurement of h_K and the requirement of return to $l(\theta)$, but no information about the past history of the sets of initial conditions is included in the classification procedure. The results of the retrograde analyses reveal that this algorithmic construction is not sufficient to guarantee a region in phase space where all prescribed stable initial conditions generate trajectories that correspond to feasible ballistic capture transfers based on the patched three-body approach.

5.4.2 Prograde Analyses of the Stable Set

We proceed with two direct time analyses meant to question the classification criteria of the WSB algorithmic construction.

The first direct analysis consists in the classification of $\mathcal{S}^\pm(e)$ obtained through implementation A according to permanence within the lunar SOI during a full cycle, that is, from $t = t_0$ to $t = t_f$, where t_f is the time instant at which the particle returns to $l(\theta)$. The qualitative result of this investigation is illustrated in Figure 5.25 for the stable sets of initial conditions with three different eccentricities in the cases of positive and negative initial velocities. The purpose of this analysis is to identify orbits that correspond to

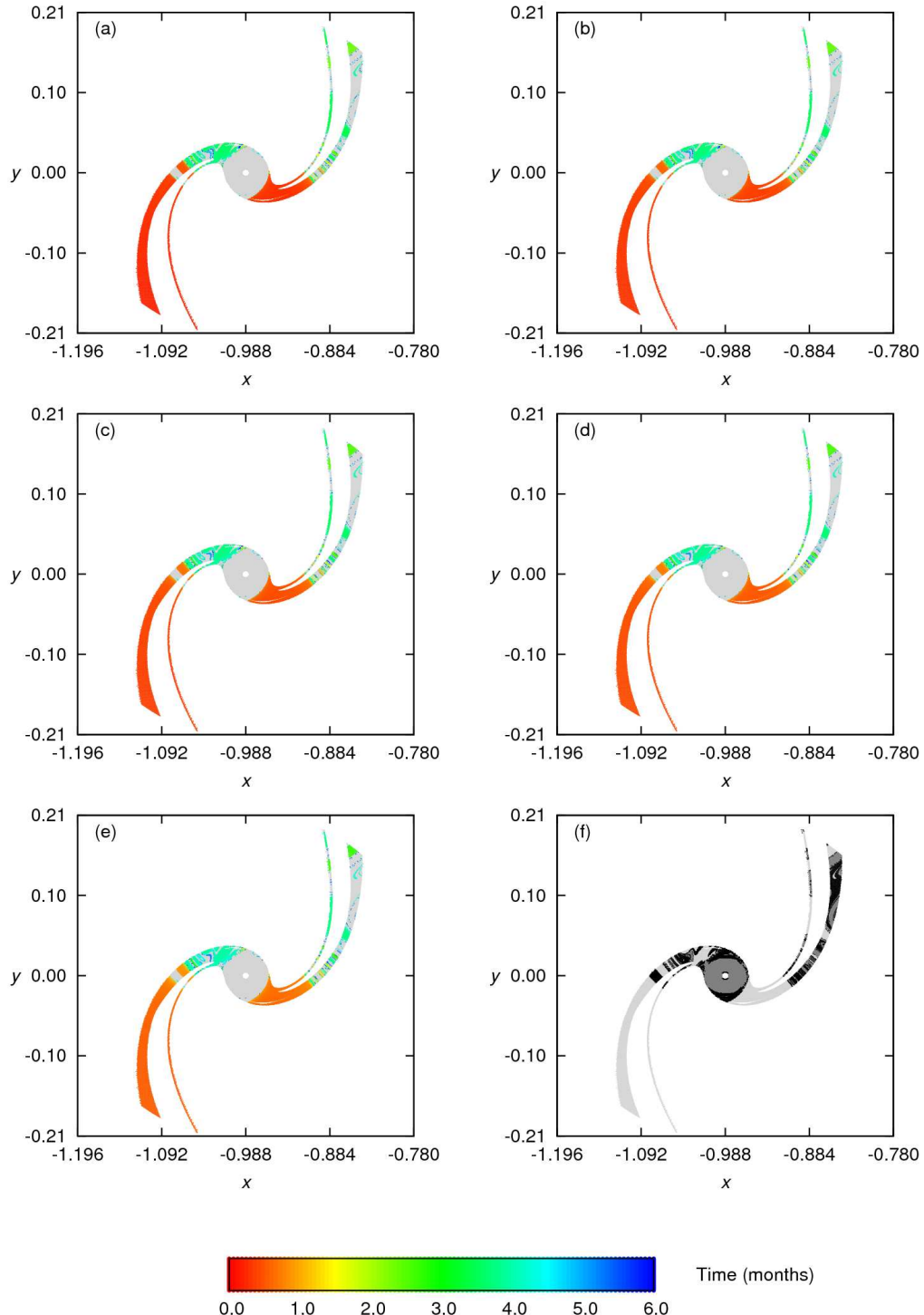


FIGURE 5.21 – Retrograde analysis regarding application in external transfers for $\mathcal{S}^+(0.6)$ obtained through implementation A. Frames (a) to (e): Initial conditions which generate trajectories that cross each Σ_i section, $i = 1, 2, 3, 4, 5$. In the plots, the colors represent the time of flight until each criterion is fulfilled. Frame (f): Collision (black) or none of the established criteria are satisfied (dark grey). In all frames the light grey points represent the complementary set of initial conditions.

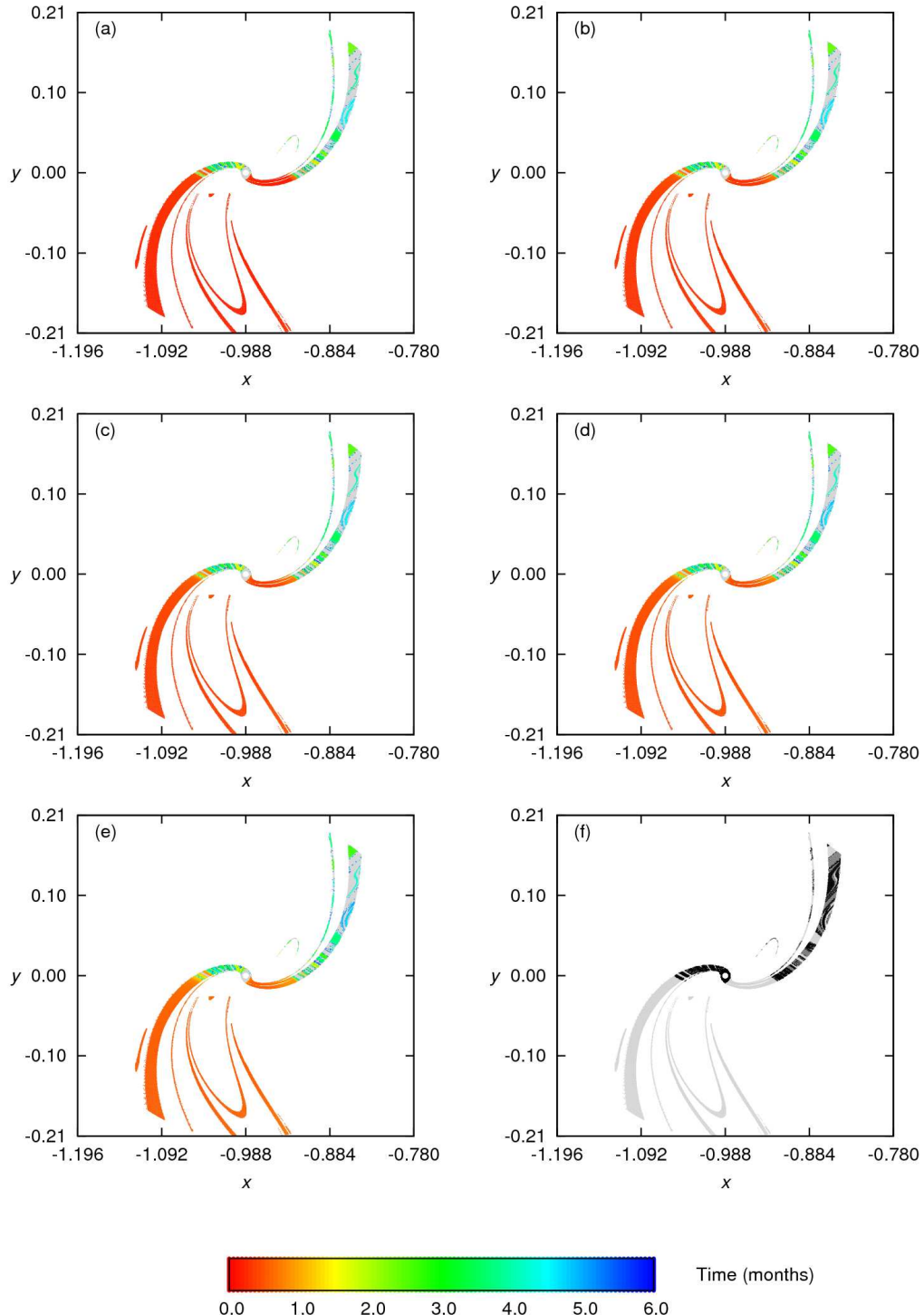


FIGURE 5.22 – Retrograde analysis regarding application in external transfers for $\mathcal{S}^+(0.9)$ obtained through implementation A. Frames (a) to (e): Initial conditions which generate trajectories that cross each Σ_i section, $i = 1, 2, 3, 4, 5$. In the plots, the colors represent the time of flight until each criterion is fulfilled. Frame (f): Collision (black) or none of the established criteria are satisfied (dark grey). In all frames the light grey points represent the complementary set of initial conditions.

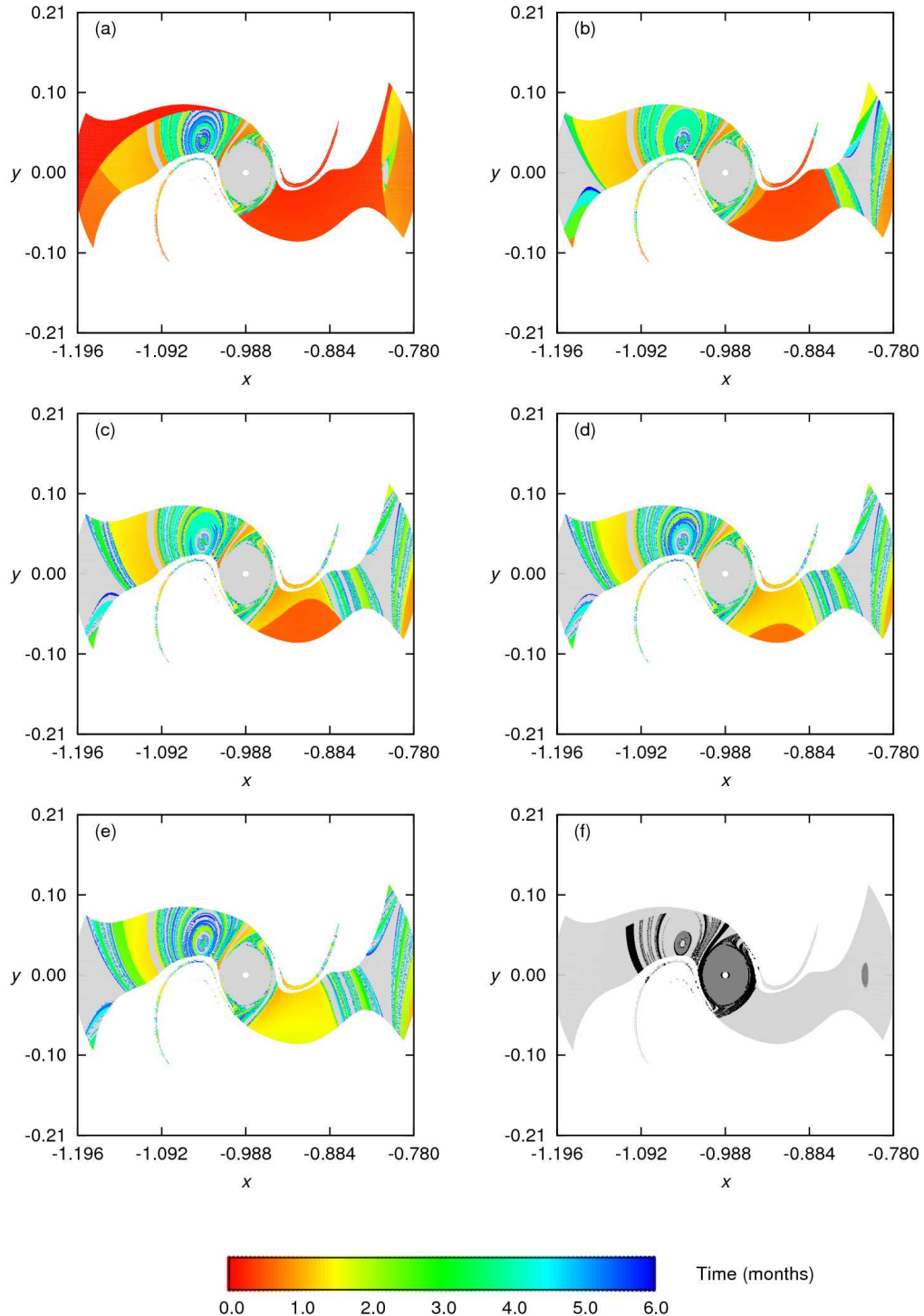


FIGURE 5.23 – Retrograde analysis regarding application in external transfers for $\mathcal{S}^-(0.6)$ obtained through implementation A. Frames (a) to (e): Initial conditions which generate trajectories that cross each Σ_i section, $i = 1, 2, 3, 4, 5$. In the plots, the colors represent the time of flight until each criterion is fulfilled. Frame (f): Collision (black) or none of the established criteria are satisfied (dark grey). In all frames the light grey points represent the complementary set of initial conditions.

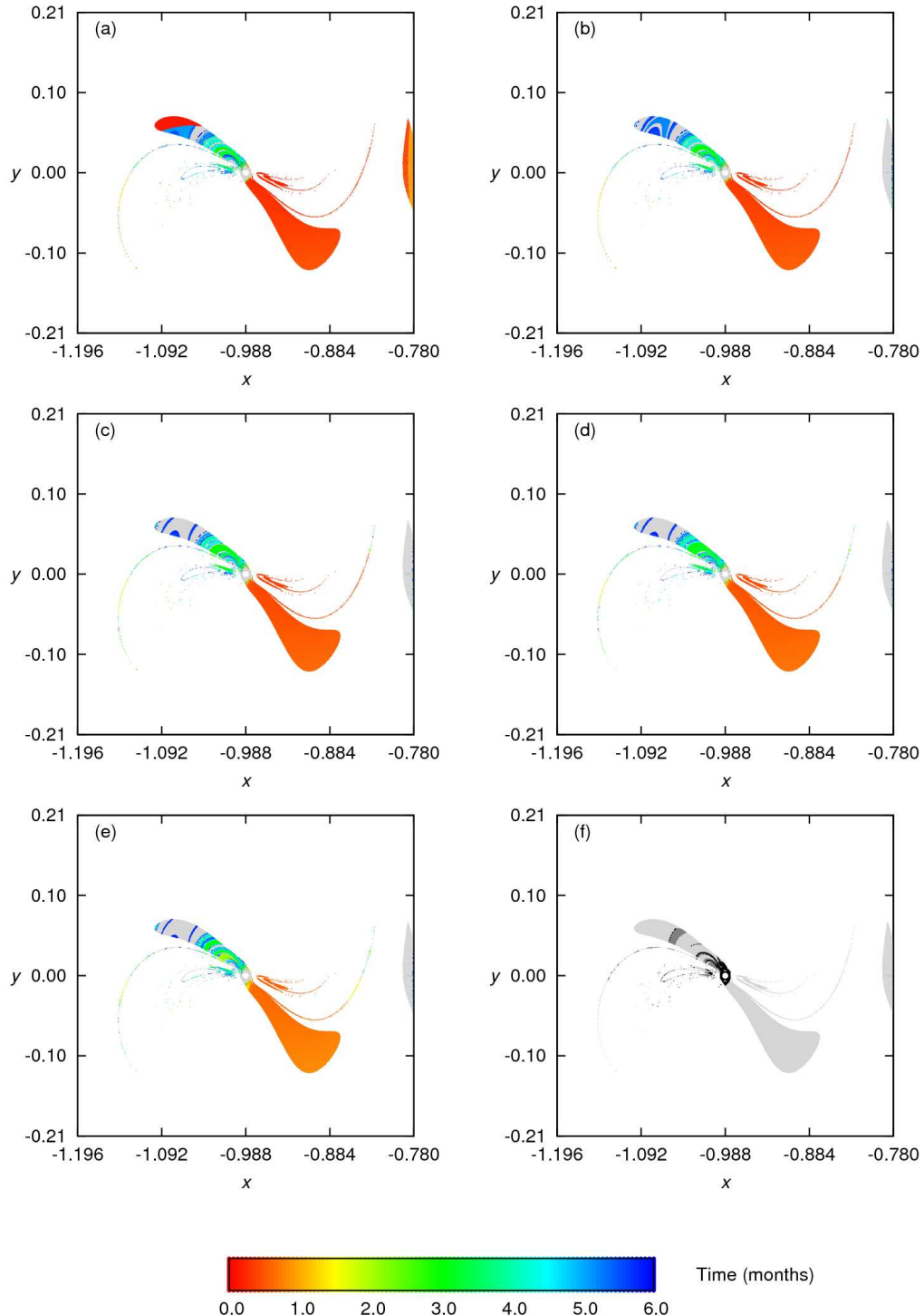


FIGURE 5.24 – Retrograde analysis regarding application in external transfers for $\mathcal{S}^-(0.9)$ obtained through implementation A. Frames (a) to (e): Initial conditions which generate trajectories that cross each Σ_i section, $i = 1, 2, 3, 4, 5$. In the plots, the colors represent the time of flight until each criterion is fulfilled. Frame (f): Collision (black) or none of the established criteria are satisfied (dark grey). In all frames the light grey points represent the complementary set of initial conditions.

temporary capture states.

As expected from the classification according to the Jacobi constant, the remnant subset prevails in the stable core region for all the considered cases, but a significant part of this core region is useless for feasible transfers under natural dynamics since it is contained in the first Hill region case ($C > C_1$).

For positive initial velocity and $e = 0.0$, the remnant subset comprises 98.23% of the stable set with $r_2 < r_H$. This value decreases to 83.72%, 27.11%, and 1.30%, when the eccentricity is 0.6, 0.9, and 0.95, respectively. For negative initial velocity, we find 78.29%, 42.86%, 17.46%, and 1.05% when $e = 0.0, 0.6, 0.9$, and 0.95.

These numbers show that the amount of trajectories for which the gravitational effect of P_1 cannot be treated as a perturbation increases as the e increases. Moreover, many of these trajectories wander far away from P_2 before P_3 returns to $l(\theta)$ with $h_K < 0$. This kind of nonlinear behavior will be illustrated in the Section 5.4.4.

The second analysis focuses on the final state after a full cycle. We observe the location of the final state after a complete cycle with respect to the lunar SOI. The aim of this analysis is to verify the adequacy of the stability criterion based on the Kepler energy computation when the trajectory returns to $l(\theta)$.

An adequate coordinate transformation gives the inertial P_2 -centered coordinates $(\tilde{x}, \tilde{y}, \dot{\tilde{x}}, \dot{\tilde{y}})$ as a function of the barycentric synodical coordinates (x, y, \dot{x}, \dot{y}) :

$$\begin{aligned}\tilde{x} &= (x + 1 - \mu) \cos t - y \sin t, \\ \tilde{y} &= (x + 1 - \mu) \sin t + y \cos t, \\ \dot{\tilde{x}} &= (\dot{x} - y) \cos t - (x + 1 - \mu + \dot{y}) \sin t, \\ \dot{\tilde{y}} &= (\dot{x} - y) \sin t + (x + 1 - \mu + \dot{y}) \cos t.\end{aligned}\tag{5.1}$$

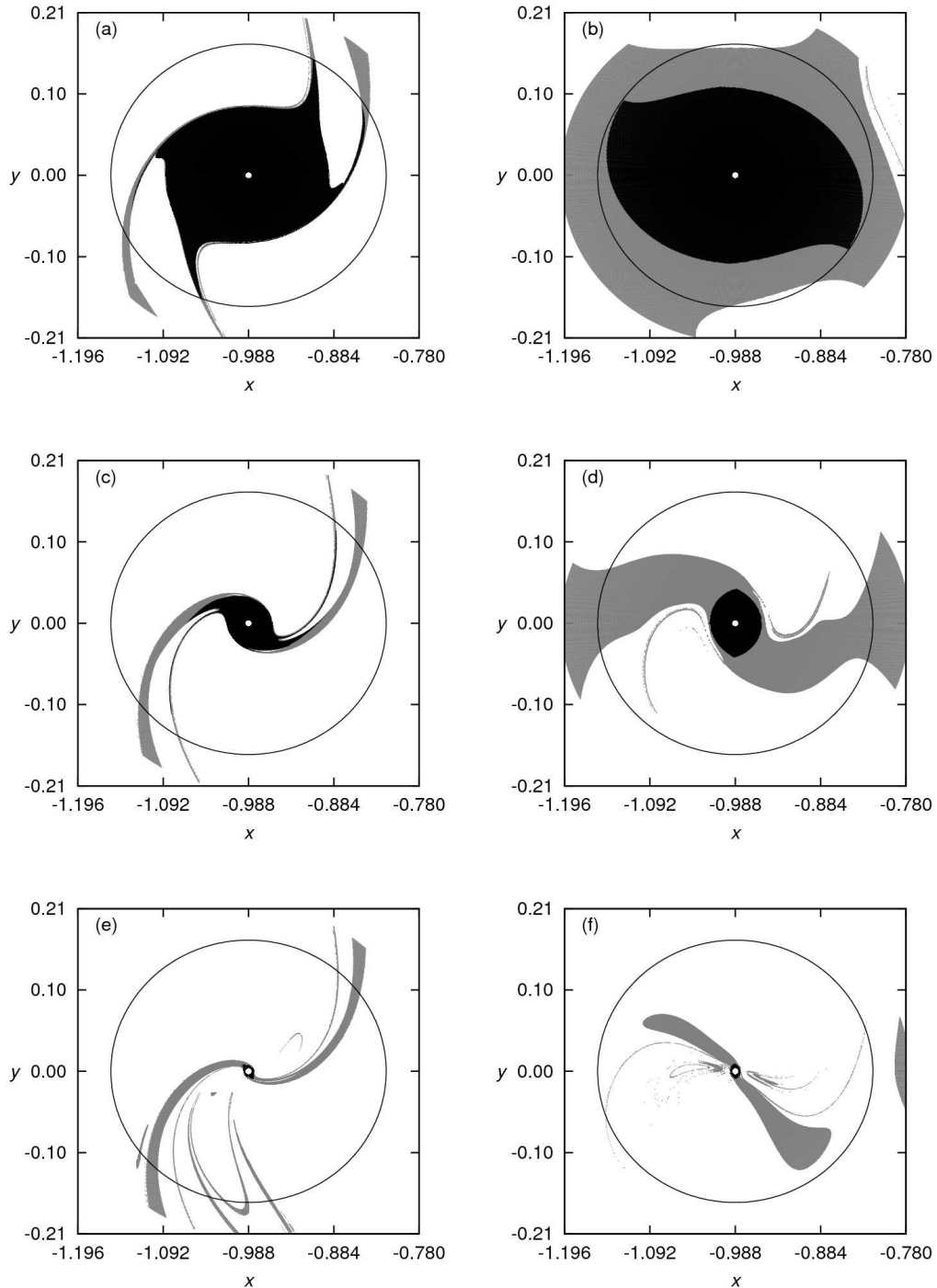


FIGURE 5.25 – Classification according to the permanence within the Moon’s sphere of influence during a full cycle of the initial conditions stable sets with positive and negative initial velocities obtained through implementation A: (a) $\mathcal{S}^+(0.0)$, (b) $\mathcal{S}^-(0.0)$, (c) $\mathcal{S}^+(0.6)$, (d) $\mathcal{S}^-(0.6)$, (e) $\mathcal{S}^+(0.9)$, and (f) $\mathcal{S}^-(0.9)$. The black points correspond to the remnant subset and the grey ones to the complementary subset.

Then, by substitution of Equation 5.1 in Equation 3.1 and using $Gm_2 = \mu$, we find that a trajectory is classified as stable if P_3 returns to $l(\theta)$ at $t = t_f$ with

$$r_f((x_f + 1 - \mu + \dot{y}_f)^2 + (\dot{x}_f - y_f)^2) \leq 2\mu, \quad (5.2)$$

where $r_f = [(x_f + 1 - \mu)^2 + y_f^2]^{1/2}$ and $x_f = x(t_f)$, $y_f = y(t_f)$, $\dot{x}_f = \dot{x}(t_f)$ and $\dot{y}_f = \dot{y}(t_f)$ are the coordinates of the particle at $t = t_f$.

Figure 5.26 illustrates the results obtained for three distinct eccentricity values: $e = 0.0$, 0.6 , and 0.9 . The amount of final states inside the lunar SOI is very high for all the eccentricities and initial conditions with positive initial velocity (99.93%, 97.70%, 87.29%, and 82.43% for $e = 0.0$, 0.6 , 0.9 , and 0.95 , respectively) and it decreases considerably as e increases for the case of negative initial velocity (87.04%, 68.12%, 41.97%, and 23.84% for $e = 0.0$, 0.6 , 0.9 , and 0.95 , respectively).

The number of trajectories classified outside the lunar SOI also increases as e increases for both the cases of positive and negative initial velocity. For these trajectories, the classification procedure is questionable, given that the quantification of the Kepler energy is performed in a region of the phase where the two-body approximation is not adequate. Disconcertingly, for negative initial velocity and $e = 0.95$, the measurement of the two-body energy may be meaningless for almost 80% of the stable set.

These two prograde analyses reveal that the measurement of the Kepler energy of final state alone does not guarantee the fulfillment of qualitative aspects of the full cycle orbits that may be required or appropriate for a ballistic capture orbit. Notably, outside the Hill sphere, third body effects become significant and the trajectory may diverge substantially from the expected two-body solution approximation. Thus, by overlooking the position with respect to the lunar SOI at the instant of classification and the time history of the

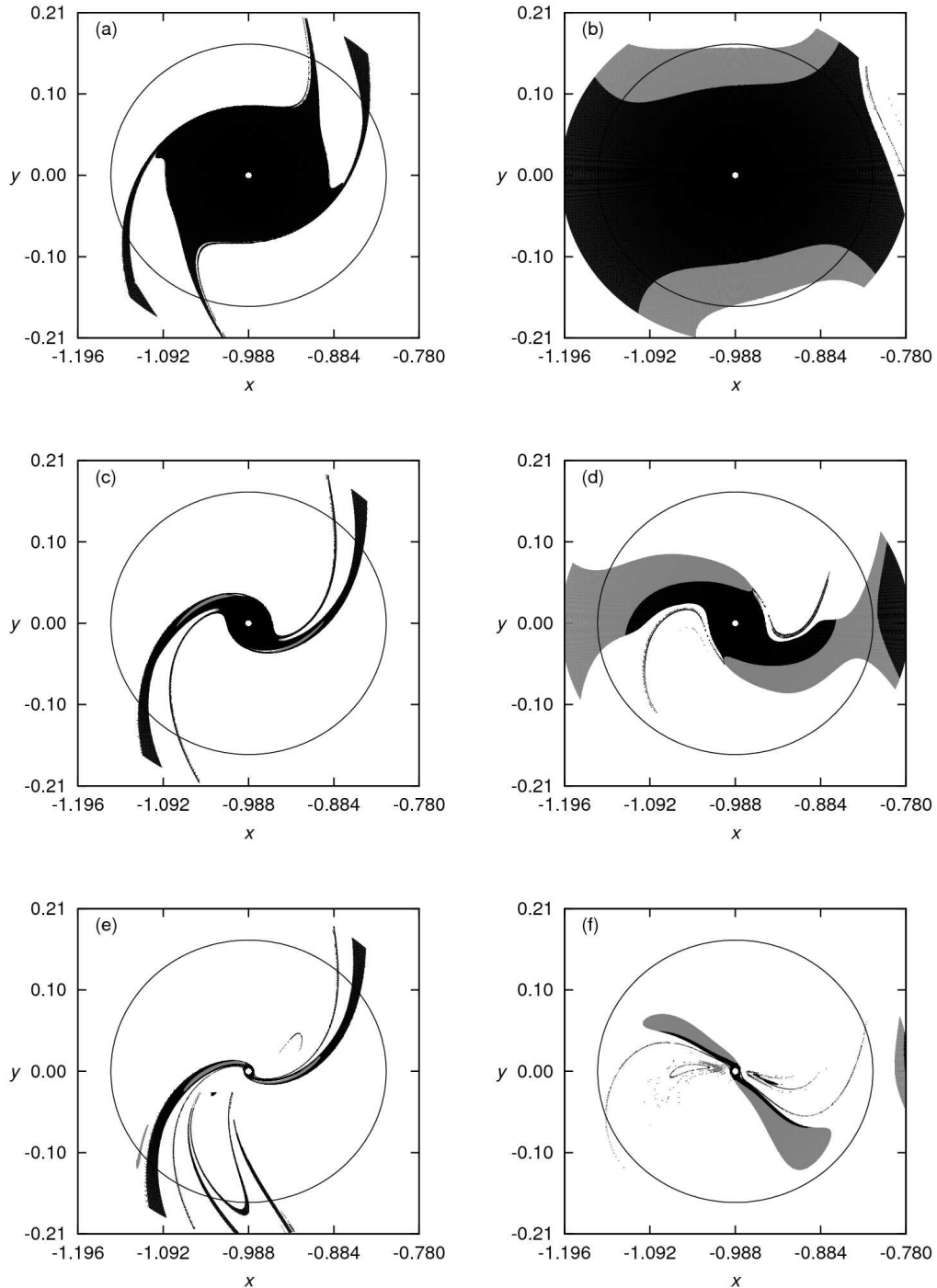


FIGURE 5.26 – Classification of the final state after a full cycle around the Moon with respect to the lunar SOI of trajectories generated by stable initial conditions obtained through implementation A: (a) $\mathcal{S}^+(0.0)$, (b) $\mathcal{S}^-(0.0)$, (c) $\mathcal{S}^+(0.6)$, (d) $\mathcal{S}^-(0.6)$, (e) $\mathcal{S}^+(0.9)$, and (f) $\mathcal{S}^-(0.9)$. The black points correspond to interior subset and the grey ones to the external final state subset.

trajectories during a full cycle, the classification procedure might be inconsistent with the highly nonlinear behavior of the trajectories. So, for practical applications, stabilization at the initial conditions is necessary for trajectories that are classified outside the lunar SOI or that spend long periods of time outside that region, that is, for these trajectories, it is not convenient perform the circularization maneuver after a full cycle around the Moon.

5.4.3 Stable Set Obtained Through Implementation B

When the algorithmic construction is performed taking collision with the primaries into account, the absolute number of initial conditions in the stable set diminishes, but the general trends of the relative results observed in the analyses of Subsections 5.4.1 and 5.4.2 remain unchanged.

The presence of the collisional orbits is restricted to the regions nearby the boundaries of the stable sets, as illustrated in Figures 5.1 and 5.2.

For fixed eccentricity, the relative decrease in the number of initial conditions is more pronounced for positive initial velocity. For $e = 0.6$, for example, the stable set with positive initial velocity diminishes 19.82%, while the stable set with negative initial velocity reduces only 2.42% with respect to the stable sets obtained through implementation A.

Both in the cases of stable initial condition with positive and negative initial velocities, the maximum relative decrease of the number of initial conditions occurs around $e = 0.9$. In that particular case, the stable sets with positive and negative initial velocities diminish, respectively, 44.07% and 10.29% with respect to the stable sets obtained when the primaries are considered to be punctual masses.

5.4.4 Diversity of Behavior in the Stable Set

The stability criteria of Definition 4 group trajectories with a wide variety of behaviors in the stable sets. That is, the construction algorithm does not rely on a fundamental classification criterion, in the sense of grouping like trajectories. This effect is caused mainly by the indiscriminate use of the two-body quantifier along with the geometric component of the definition (the return to $l(\theta)$ criterion).

Figure 5.27 illustrates the diversity of behavior of trajectories generated by stable initial conditions with positive initial velocity obtained through implementation B. In Table 5.10 we specify relevant information for these trajectories, such as the osculating ellipse eccentricity, the initial conditions, the Jacobi constant value and the flight time of the trajectory until its classification.

For $e = 0$, it is common to find quasiperiodic orbits, like the one in Figure 5.27 (a). As the eccentricity value increases, trajectories may wander far away from P_2 , as seen in Figure 5.27 (h), (j), and (m). This behavior is expected from the classification of $\mathcal{S}^+(e)$ according to permanence within the lunar SOI. In cases (h) and (j), P_3 goes to the exterior realm and to the Earth realm, respectively, and returns to $l(\theta)$ before completing a full turn (360°) around P_1 . In case (m), P_3 visits both the Earth and the exterior realms before returning to $l(\theta)$. In such cases, the trajectories present a long flight time until they return to $l(\theta)$, as shown in Table 5.10. In case (k), the trajectory winds around the L_1 Lyapunov orbit of the corresponding energy level before completing a full turn around the Moon.

The diversity of trajectories in the the stable sets with negative initial velocity is also displayed in Figure 5.28. Once again, the stable sets were obtained through implementation B and we specify some relevant information about the trajectories in Table 5.11. We

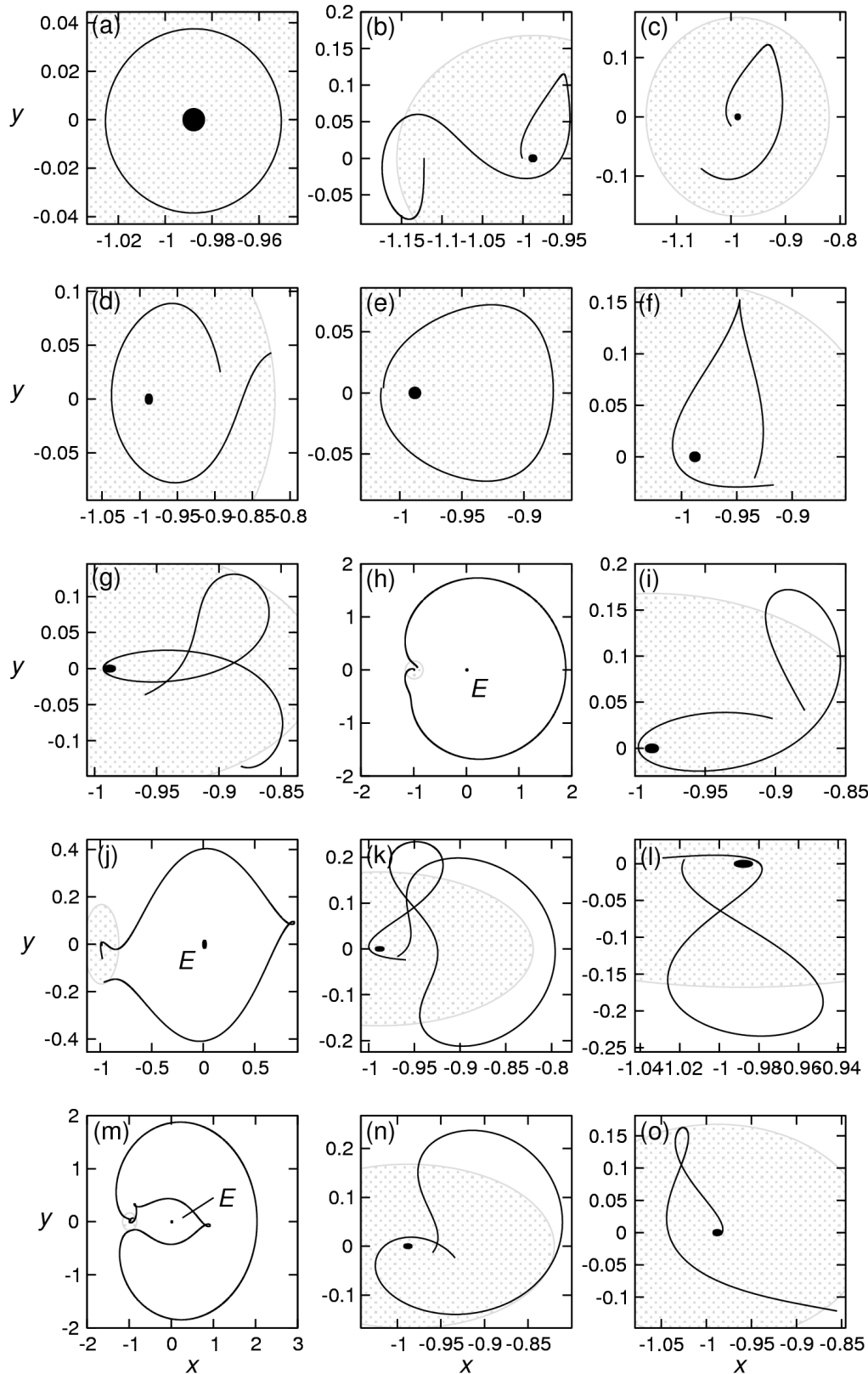


FIGURE 5.27 – Projection onto the x - y plane of trajectories generated by stable initial conditions with positive initial velocity for (a-d) $e = 0.0$, (e-g) $e = 0.6$, (h-l) $e = 0.9$, and (m-o) $e = 0.95$. The lunar SOI is depicted by the shaded region. The primaries are indicated by black points (the Earth is labeled with an E).

	e	x_0	\dot{x}_0	C	t_f	$r_f < r_H$
		y_0	\dot{y}_0			
(a)	0.0	-0.984443 0.037274	-0.530121 0.048431	3.329463 (1)	0.447499	✓
(b)	0.0	-1.122052 0.000421	-0.000523 -0.166691	3.166222 (3)	3.985934	✓
(c)	0.0	-1.054727 -0.087347	0.176527 -0.135161	3.149227 (3)	1.990005	✓
(d)	0.0	-0.892789 0.025044	-0.064525 0.244911	3.175165 (3)	2.073145	-
(e)	0.6	-1.014797 0.004268	-0.127781 -0.806781	3.189126 (2)	1.791081	✓
(f)	0.6	-0.933983 -0.020741	0.187805 0.487723	3.120305 (3)	1.570593	✓
(g)	0.6	-0.959532 -0.036269	0.476075 0.371683	3.129206 (3)	2.824464	-
(h)	0.9	-0.922916 0.043239	-0.258277 0.387856	3.070653 (3) <u>15.111677</u>		✓
(i)	0.9	-0.879100 0.041092	-0.116425 0.308111	3.101475 (3)	2.073715	✓
(j)	0.9	-0.965593 -0.159978	0.214478 0.029837	3.067683 (3) <u>6.601197</u>		✓
(k)	0.9	-0.968184 -0.016582	0.594139 0.704563	3.060013 (3)	5.543347	✓
(l)	0.9	-1.017698 0.005791	-0.160173 -0.825561	3.058177 (3)	2.069572	✓
(m)	0.95	-0.960592 0.018150	-0.453311 0.680741	3.038965 (3) <u>21.202074</u>		✓
(n)	0.95	-0.959267 -0.012475	0.336204 0.770275	3.038888 (3)	2.999202	✓
(o)	0.95	-0.984418 -0.003141	1.521063 1.661112	3.115170 (3)	2.221176	-

TABLE 5.10 – Specific information of trajectories displayed in Fig. 5.27, generated by stable initial conditions with positive initial velocity. The columns display the eccentricity, the initial conditions, the Jacobi constant value and the time to return to $l(\theta)$ in dimensionless units. In the last column we mark trajectories that are classified as stable inside the lunar SOI with a ✓. In the fourth column the numbers in parenthesis refer to the \mathcal{C}^i set of the classification according to the Jacobi constant value.

find non-transfer quasiperiodic trajectories, like the one in Figure 5.28 (a), with higher energy than in the case of positive initial velocity. As seen from Figure 5.28 (b), (d), and (j), it is quite common to find trajectories that go far away from the Moon, outside the lunar SOI, but then return to $l(\theta)$ at $r_f < r_0$, showing some resemblance with highly eccentric two-body elliptic solutions. Frames (c), (k), and (n) show solutions which return to $l(\theta)$ outside the lunar SOI. Finally, many trajectories present highly nonlinear behavior. Examples for $C > C_4$ are found in frames (f), and (l). Many initial conditions have $C < C_4 = C_5$, so trajectories may wander through phase space with no restriction, as observed in Figure 5.28 (e), (g), (i), and (o). Again the flight time for these cases is very long.

The underlined quantities in Tables 5.10 and 5.11 diverge substantially from the mean values of flight time at which typical trajectories are classified. This indicates that, by neglecting the time history between the initial condition and the final state, the classification procedure allows a broad diversity of trajectories to be assigned to the stable set, although their behaviors are not consistent with temporary capture states for practical application. Thus, the flight time can be considered an indicator of anomalous trajectory profiles in terms of capture.

Trajectories like the ones displayed in Figure 5.27 (m) and Figure 5.28 (i), for example, clearly do not present a behavior that would be desirable as a bounded capture state for practical purposes. So, unless stabilization is performed at the initial condition itself, these trajectories are not suited for application.

In addition to the wide variety of stable solutions, we find trajectory profiles that are similar to the stable ones in all the unstable subsets. So, both stable and unstable trajectories could provide feasible solutions. In view of these results, it is not clear why

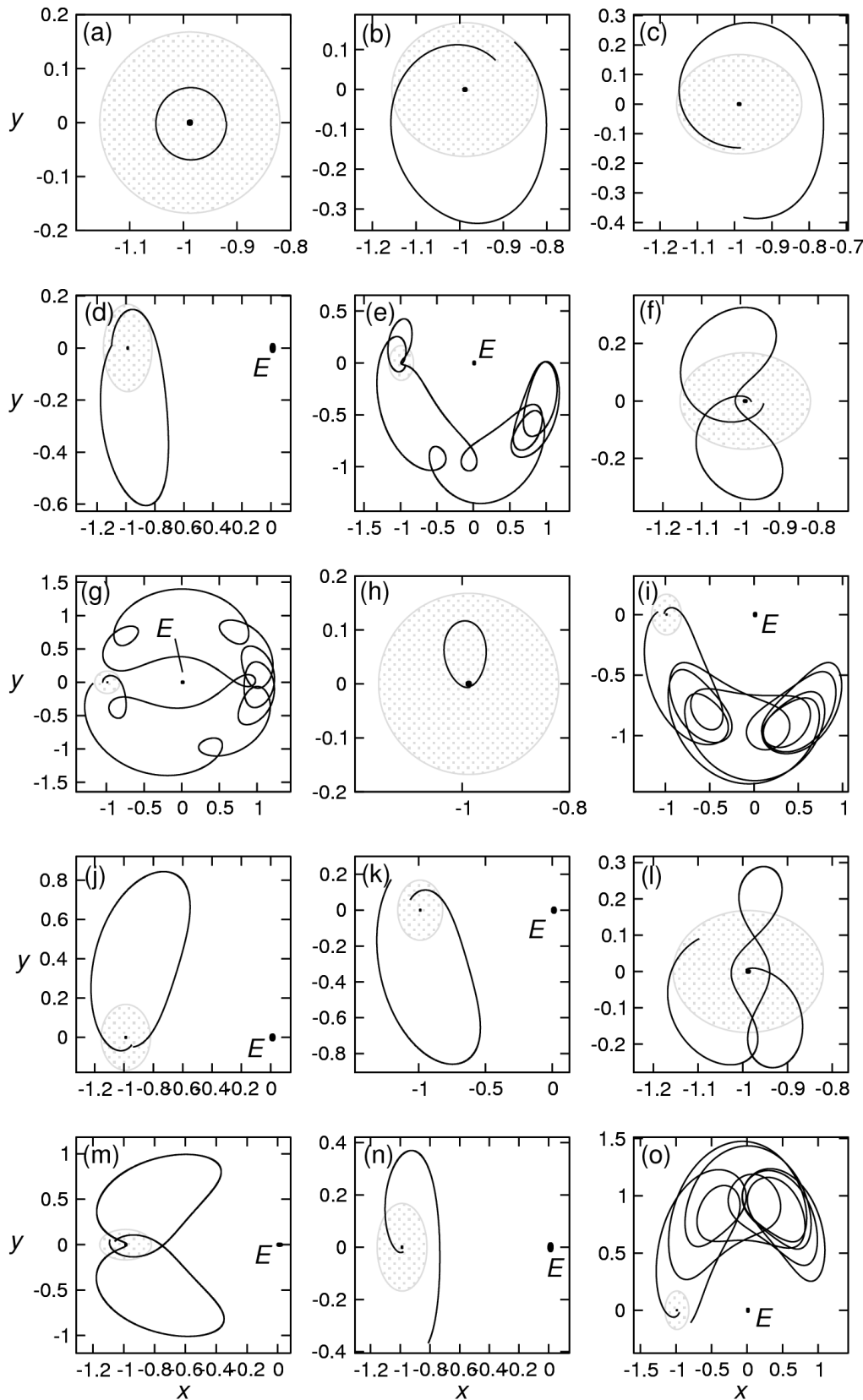


FIGURE 5.28 – Projection onto the x - y plane of trajectories generated by stable initial conditions with negative initial velocity for (a-c) $e = 0.0$, (d-g) $e = 0.6$, (h-k) $e = 0.9$, and (l-o) $e = 0.95$. The lunar SOI is depicted by the shaded region. The primaries are indicated by black points (the Earth is labeled with an E).

	e	x_0	\dot{x}_0	C	t_f	$r_f < r_H$
		y_0	\dot{y}_0			
(a)	0.0	-0.919235 0.002156	0.015371 -0.489121	3.092768 (3)	0.841677	✓
(b)	0.0	-0.874018 0.118950	0.315223 -0.301655	2.956965 (5)	3.092643	✓
(c)	0.0	-0.983217 -0.147398	-0.434299 -0.013648	2.939910 (5)	3.510028	-
(d)	0.6	-1.098784 0.011894	0.056397 0.525986	2.935747 (5)	4.514383	✓
(e)	0.6	-0.928379 -0.018910	-0.188051 -0.591379	2.978774 (5)	<u>42.207020</u>	✓
(f)	0.6	-0.940187 -0.008164	-0.115215 -0.672626	3.007373 (4)	5.937626	✓
(g)	0.6	-1.047662 -0.005464	-0.057225 0.626383	2.982770 (5)	<u>56.726007</u>	-
(h)	0.9	-0.985310 -0.005669	-1.765113 -0.790313	3.135168 (3)	0.820030	✓
(i)	0.9	-1.014359 0.006452	0.223998 0.920276	2.959201 (5)	<u>57.298392</u>	✓
(j)	0.9	-0.948200 -0.038664	-0.489438 -0.501897	2.915544 (5)	5.080018	✓
(k)	0.9	-1.062076 0.058326	0.363873 0.463065	2.890479 (5)	5.013351	-
(l)	0.95	-0.992648 0.003944	1.244070 1.513479	3.037109 (3)	7.349796	✓
(m)	0.95	-1.057133 0.037524	0.298678 0.551474	2.892575 (5)	11.442071	✓
(n)	0.95	-0.979728 -0.016843	-1.030804 -0.496979	2.953784 (5)	3.228220	-
(o)	0.95	-0.953860 -0.019105	-0.401071 -0.713533	2.920303 (5)	<u>50.913112</u>	-

TABLE 5.11 – Specific information of trajectories displayed in Fig. 5.28, generated by stable initial conditions with negative initial velocity. The columns display the eccentricity, the initial conditions, the Jacobi constant value and the time to return to $l(\theta)$ in dimensionless units. In the last column we mark trajectories that are classified as stable inside the lunar SOI with a ✓. In the fourth column the numbers in parenthesis refer to the \mathcal{C}^i set of the classification according to the Jacobi constant value.

the boundary of such a diverse set would have a separatrix feature such as the one of the parabolic Keplerian solution that separates bounded and unbounded motion in the two-body problem.

5.5 Discussion

The results presented in this Chapter constitute a dynamical characterization the WSB associated sets generated by the algorithmic definition. They allow us to draw several conclusions about the algorithmic construction and set ground for a refined investigation of the boundary itself.

The introduction of the finite radii of the primaries in implementation B shows that, due to collision, the applicability of portions of the WSB is restricted to the stabilization of trajectories at the initial conditions. In addition, the subclassification of the unstable set reveals that there exist several transition types. The nature and characteristics of such transitions will be further explored in Chapter 6.

The classification of the sets of initial conditions according to the Jacobi constant reveals that many initial conditions are not suited for actual transfer missions due to energy restrictions. Particularly, we expect typical altitudes of final selenocentric orbits to require high eccentricities ($e > 0.9$) implying high energy ($C < C_3$) and greater diversity of the nonlinear behavior of the trajectories. Moreover, the grid-dependent character of the algorithmic construction needs to be observed in the extraction of the stability boundary.

For direct inner transfers applications, we find that natural dynamics requires long periods of flight time and there are very few candidate trajectories available. Moreover, the existence of an invariant torus around the larger primary prevents the arbitrary ap-

proximation of P_3 . Other dynamical elements, such as a third degree of freedom and the solar gravitational influence, need to be included when modeling the system in order to achieve satisfactory results.

For external transfers based on a patched three-body approach, we find that portions of the associated sets provide candidate initial conditions for several initial configurations of the Sun-Earth-Moon system setup. Nonetheless, these orbits, associated with a natural capture state by the Moon, need to be investigated in terms of the complete Earth-to-Moon trajectory to verify their energy adequacy in providing low energy transfers.

The characterization of the trajectories generated by stable initial conditions brings up the question of why the boundary of such a diverse set would have a separatrix feature such as the parabolic Keplerian solution that separates bounded and unbounded motion in the two-body problem. Our analyses suggest that the use of h_K as an adequate quantifier should be restricted by the validity of the two-body approximation, given that the classification generated by the use of the return to $l(\theta)$ geometrical criterion along with the measurement of h_K is not always consistent with the highly nonlinear behavior of the trajectories.

Our analyses show that natural dynamical aspects of the PCR3BP are neglected by the algorithmic definition. Some of these are the total flight time at the classification, the relative position at the instant of classification with respect to the lunar SOI, and the past history of the trajectories, so as to distinguish transfer and no transfer solutions. As a result, the stability classification does not lead exclusively to ballistic capture solutions with adequate profiles for practical applications.

All things considered, since the classification does not result in boundary sets that act as natural separatrices of the solutions of the system regarding the characterization of

effective stable behavior, it is not clear why the stability boundary algorithmically defined should provide best candidates for potential transfer orbits. This final questioning is the focus of the next Chapter.

6 Stable-Unstable Transitions of the WSB

In this Chapter we investigate the nature of stable-unstable transitions produced by the WSB algorithmic definition (Definition 5). Our main goal is to clarify the dynamical characteristics of this stability boundary through the detection of the mechanisms which are responsible for the transitions and to verify the consistency of the constructive procedure concerning the achievement of temporary capture trajectories.

We find that the stability classification arises from two sets of mechanisms. The first set is comprised of three dynamical agents that may act individually or in association to cause the divergence of trajectories which approach them, resulting in the classification of trajectories as stable or unstable. These agents are the primary P_2 and the Lyapunov orbits around L_1 and L_2 with their stable and unstable invariant manifolds. In this case, the stable-unstable classification is evidence of the nonlinear behavior of the trajectories.

The second set of mechanisms comprises constructive aspects of the algorithmic definition itself, i.e., arbitrary requirements of the algorithmic definition which do not account for essential dynamical features to identify stable behavior, nonetheless, are part of the algorithm. In this case, the classification results from the association of two geometrical criteria and an analytical criterion, namely, the return to $l(\theta)$, the requirement of a complete turn around P_1 in the case of primary interchange, and the measurement of the Kepler energy.

Organization of the Chapter: In Section 6.1, we extract the stability boundary, emphasizing its relation with the lunar collisional set. In addition, we implement a refinement procedure, revealing the existence of both smooth and fractal-like, grid-dependent portions of the boundary set. In Section 6.2 we characterize transitions due to dynamical effects, namely, collision with the Moon and the invariant manifolds of the Lyapunov orbits, while in Section 6.3 we characterize transitions that occur because of constructive effects. Finally, in Section 6.4 we present the conclusions of this specific investigation. The results of this Chapter were recently submitted for publication [35].

6.1 Extraction of the WSB

We proceed with the extraction of the stability boundaries \mathcal{W}^e associated to the stability classification of implementation A. We focus on $e = 0.9$, given that higher eccentricity values are more adequate for practical applications as described in Chapter 5 and Refs. [32, 35], and detailed in Section 6.1.1.

As an initial approach, the boundary was built as the set of stable initial conditions which had at least one neighboring unstable point. In this extraction of the boundary we considered first neighbors both in the radial and the angular directions. This is an approximation of the actual boundary set and is conditioned to the grid employed in the discretization of the x - y plane. Moreover, isolated stable points, surrounded only by unstable initial conditions, appear due to the discrete nature of the grid. In such cases, these initial conditions are also extracted as boundary points.

In agreement with Ref. [8], it is common to have more than one r^* where stable-unstable transitions occur along a radial line.

6.1.1 Collision Along the Stability Boundary

Comparing implementations A and B, we find that the boundaries of stability originated by Definition 4 are often related to trajectories that come to a close approach to the secondary. In fact, many boundary points extracted from the stable set of implementation A, will collide with the smaller primary when implementation B is performed, as shown in Figure 6.1. Particularly, for $e = 0.9$ and positive initial velocity, 53.84% of the boundary points obtained through implementation A belong to the collisional subset \mathcal{C} generated by implementation B. In the case of negative initial velocity, 40.33% of the boundary points generate collisional orbits.

The large presence of collisional trajectories in the boundary set is justified by the fact that the close approach to the primary causes divergence of neighbor trajectories in the phase space, implying distinct nonlinear behaviors and different stability classification. Although the lunar collisional set usually spreads along the vicinity of the stable set boundary for initial conditions with both positive and negative initial velocities, we also find that there are regions where the boundary of the stable set does not coexist with the collisional set.

As seen from Figure 6.1 (a), for the set of initial conditions with positive initial velocity and $e = 0.9$, the Moon collisional set accompanies the stability boundary, restricting the applicability of the boundary set to circularization at the initial conditions. This is a typical feature for sets of initial conditions with positive initial velocity in the lunar SOI associated to other eccentricity values as suggested by comparing the associated sets generated by the stability classification with implementations A and B in Figures 5.1 and 5.2.

In the case of initial conditions with negative velocity, the Moon collisional set is

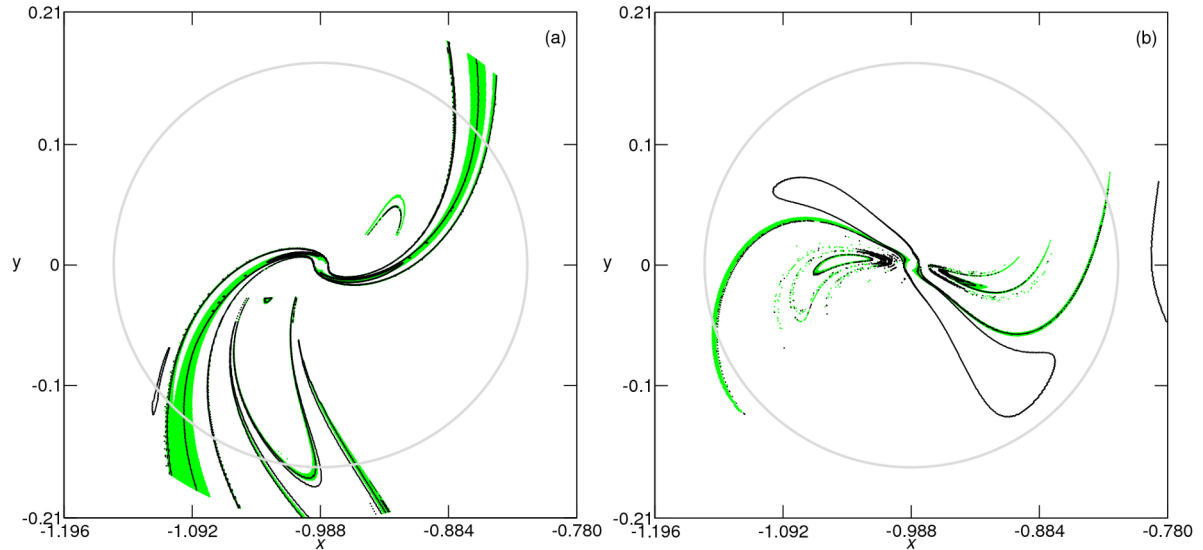


FIGURE 6.1 – Boundary of stability (black points) obtained through implementation A for $e = 0.9$ with (a) positive and (b) negative initial velocities. The grey (green online) points are the sets of initial conditions which collide with the Moon when implementation B is performed. The large grey circle delimits the lunar SOI.

often related to isolated points of the boundary. As seen from Figure 6.1 (b), for the case of $e = 0.9$, collision is associated with the thin subsets of stable points that spread horizontally along the x -axis. As seen in Figures 5.1 and 5.2, for low e , a stable core of initial conditions prevails around the Moon, so the stability boundary set is close to that primary only for medium to high eccentricity values.

6.1.2 Refined Extraction

We focus on transitions along the radial line $l(\theta)$ for fixed θ . In order to extract a finer boundary set, a refinement procedure can be performed in the radial segment between the stable point and the unstable point of a detected transition. By implementing such a procedure, we find, basically, two different situations along the weak stability boundary, namely, smooth and fractal-like grid-dependent transitions.

For smooth transitions, when a bisection procedure between a stable point and a certain type of unstable point (\mathcal{E} , $\mathcal{G}^{1,2,3}$ or \mathcal{T}) is performed, a finer stable-unstable pair

of the same type will appear. Take, for example, $\theta = \pi$ rad, $e = 0.9$ and positive initial velocity. For a radial increment Δr_2^0 (defined in Section 5.1) the first stable-unstable transition along $l(\theta)$ occurs at $r^* = 5.43184183 \times 10^{-3}$. The transition is said to be of type S-G1, since the first unstable neighbor belongs to the \mathcal{G}^1 unstable subset. If we refine the line segment defined by the last stable point and the first unstable point, only new points belonging to \mathcal{S} or \mathcal{G}^1 appear. Then, up to a resolution of $\Delta r_2 = \Delta r_2^0 \times 10^{-4}$, we find $r^* = 5.92609261 \times 10^{-3}$, which corresponds to an altitude of approximately 540 km.

Other types of smooth transitions also occur. Take, for instance, the S-E (stable-unstable due to non-negative h_K) transition type that occurs for the set of initial conditions with negative initial velocity and $e = 0.9$, for $\theta = 0.64\pi$ rad at $r^* = 2.96624609 \times 10^{-2}$, or approximately 9,664.25 km of altitude, with resolution of $\Delta r_2 = \Delta r_2^0 \times 10^{-4}$. In this particular case, the trajectories return to $l(\theta)$ inside the lunar SOI ($r_f < r_H$). Likewise, transitions of types S-E with $r_f > r_H$ and S-G2 were detected for sets of initial conditions with positive and negative initial velocities.

Typically, smooth transitions are associated with large stable regions and related both to collisional and non-collisional orbits. This kind of transition is very common in the boundary set with negative initial velocity, especially along the boomerang shaped stable region of Figure 6.1 (b).

The second situation comprises grid-dependent transitions. This case is conditioned to the grid resolution and refers to the fact that several transitions of different types are found when a refinement procedure is performed. Usually, both dynamical and constructive effects are combined to generate the fractal-like structure of the boundary.

In this case, the stability configuration along the line changes as different dynamical structures and/or constructive effects are manifested, according to the chosen grid res-

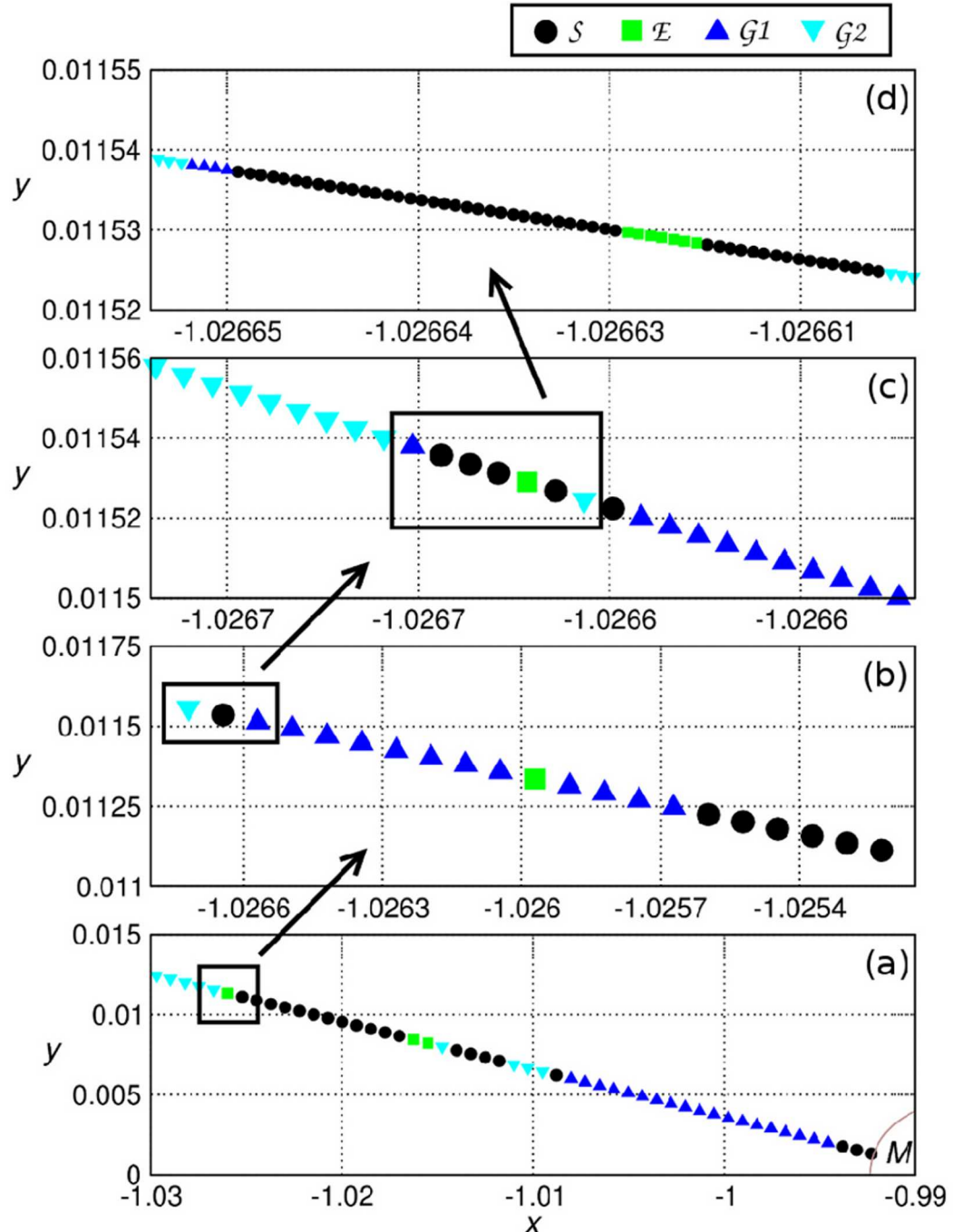


FIGURE 6.2 – Successive magnifications of stable-unstable transitions for (a) Δr_2^0 , (b) $\Delta r_2^0/10$, (c) $\Delta r_2^0/100$, and (d) $\Delta r_2^0/1000$, displaying the grid resolution issue associated with grid-dependent transitions. In this example we consider the set of initial conditions with positive initial velocity and $e = 0.9$. The black circles represent stable initial conditions. For unstable behavior we have: \mathcal{E} , green squares; \mathcal{G}^1 , blue up triangles; \mathcal{G}^2 , cyan down triangles.

Stability Configuration		
(a)	Δr_2^0	$\{\mathcal{G}^2 \mathcal{E} \mathcal{S}\}$
(b)	$\Delta r_2^0/10$	$\{[\mathcal{G}^2 \mathcal{S} \mathcal{G}^1] \mathcal{E} \mathcal{G}^1 \mathcal{S}\}$
(c)	$\Delta r_2^0/100$	$\{\mathcal{G}^2 [\mathcal{G}^1 \mathcal{S} \mathcal{E} \mathcal{S} \mathcal{G}^2] \mathcal{S} \mathcal{G}^1\} \mathcal{E} \mathcal{G}^1 \mathcal{S}$
(d)	$\Delta r_2^0/1000$	$\{\mathcal{G}^2 \mathcal{G}^1 \mathcal{S} \mathcal{E} \mathcal{S} \mathcal{G}^2\} \mathcal{S} \mathcal{G}^1 \mathcal{E} \mathcal{G}^1 \mathcal{E} \mathcal{G}^1 \mathcal{S}$

TABLE 6.1 – Stability configuration of initial conditions with positive initial velocity and $e = 0.9$ on the radial segment with $\theta = 0.64\pi$ rad for four different radial steps. Each row of the table from (b) to (d) presents all the types of solutions found within the considered resolution in the segment line defined by the S-E-G1 solutions of row (a). The [] delimit the subset of solutions chosen to be magnified in the successive frame of Fig. 6.2, while the {} contain all the types of solutions presented in each frame of Fig. 6.2.

olution, i.e., Δr_2 . When a finer spatial scale is required to resolve the transitions, this grid dependent characteristic of the algorithmic stability boundary results in practical uncertainty in establishing the final state of the trajectories.

Take, for example, the case of initial conditions with positive initial velocity, $e = 0.9$ and $\theta = 0.909\pi$ rad. For Δr_2^0 , we detect a S-E transition at $r_2 = 3.89906347 \times 10^{-2}$. The next unstable neighbor of the isolated \mathcal{E} point is an initial condition that belongs to the unstable subset \mathcal{G}^2 . While Figure 6.2 displays successive magnifications of specific transitions that appear between the original \mathcal{S} and the \mathcal{G}^2 points, Table 6.1 shows the stability configuration on the line segment for the three radial steps considered besides Δr_2^0 . The three original solutions are shown in the box of Figure 6.2 (a). In frame (b) the segment line between the previous S-E-G2 states is refined, revealing the existence of other types of solutions in the interval that determine three stable-unstable transitions with only two WSB points. Frame (c) of Figure 6.2 displays the magnification of two of these transitions (G1-S-G2 shown inside the box in frame (b)). New solutions appear defining six stable-unstable transitions, namely, two S-E, two S-G2, and two S-G1 with the presence of four boundary points. Finally, in frame (d), we chose to refine the sequence G2-S-E-S-G1 (shown in the box of frame (c)). In this refinement only points of the same

type appear, resulting in the same transition sequence but with four WSB points instead of three boundary points found in the box of frame (c).

6.2 Transitions Due to Dynamical Effects

6.2.1 Collision and Close Approach to the Moon

The force acting on P_3 , as well as the particle's velocity, increases as P_3 approaches the vicinity of one of the primaries, going to infinity as the distance between the bodies goes to zero. Considering the punctual mass idealization of the PCR3BP, collision with the primaries occurs when r_1 or r_2 is zero. So, the equations of motion present non-essential singularities which can be eliminated through regularization.

We find that a close approach to P_2 can produce a stable-unstable transition due to the divergence of the velocities of two close orbits as they approach the singularity. Particularly, there are cases in which the orbit at the boundary collides with the center of mass of P_2 ; hence, there is an effective dynamical separatrix between the classified trajectories. The determination of a refined boundary point in this case depends on the numerical precision allowed in our computations.

As an example, Figure 6.3 displays the collisional transition at $r^* = 0.01425078$, $\theta = 1.753\pi$ rad for $\Delta r_2^0 \times 10^{-1}$ in the set of initial conditions with $e = 0.9$ and negative initial velocity. The minimum distance from P_3 to P_2 occurs for the detected stable trajectory and is of the order of 10^{-5} dimensionless units. The Jacobi constant value of this stable trajectory is $C^s = 3.01263963$. In this particular example, the transition is of type S-E. Although the projection onto the \dot{x} - \dot{y} plane displays diverse velocity profiles during the close encounter with the moon, the time series of the Kepler energy do not indicate substantial differences between the stable and the unstable trajectories up to $t = 15$

dimensionless time units. Thus, the adequacy of the two-body quantifier is questionable, as might be expected given that the interaction of P_2 and P_3 cannot be approximated by a two-body subsystem outside the lunar SOI. The classification of the unstable orbit is due to the late return of the trajectory to $l(\theta)$ outside the lunar SOI after a full turn around the Moon, before completing 360° around the Earth, while the stable trajectory is classified at a previous time instant, near the Moon, after a full turn around $l(\theta)$.

As capture trajectories, the orbit at the boundary and its stable neighbor are useless, unless circularization is performed at the initial conditions, given that they collide with the finite radius of the Moon before returning to $l(\theta)$ in implementation B.

In addition, we find that the divergence caused by the collisional mechanism also produces transitions of types S-G1 and S-G2.

6.2.2 Invariant Manifolds

The stable-unstable transition can be determined by the proximity of trajectories to the stable manifold of a Lyapunov orbit Γ_k , $k = 1, 2$ around the collinear equilibria L_k . In this case, for the corresponding energy levels, the stable orbit is a non-transit solution exterior to the stable tube W_k^s of Γ_k , while the unstable orbit is a transit solution inside W_k^s .

Even if both orbits are exterior to W_k^s , the proximity to Γ_k can cause divergence of these trajectories in the phase space. This fact combined with other mechanisms can lead to a transition.

Although the Jacobi constant C is not kept fixed along $l(\theta)$, by fixing θ and refining the radial step between a given stable initial condition p^s , with Jacobi constant C^s , and its first unstable neighbor p^u , with Jacobi constant C^u , we have that $|C^s - C^u| \rightarrow 0$ (or $C^{s,u} \rightarrow C^*$) as $\Delta r_2 \rightarrow 0$. So, for this type of transition, we can infer that the orbit

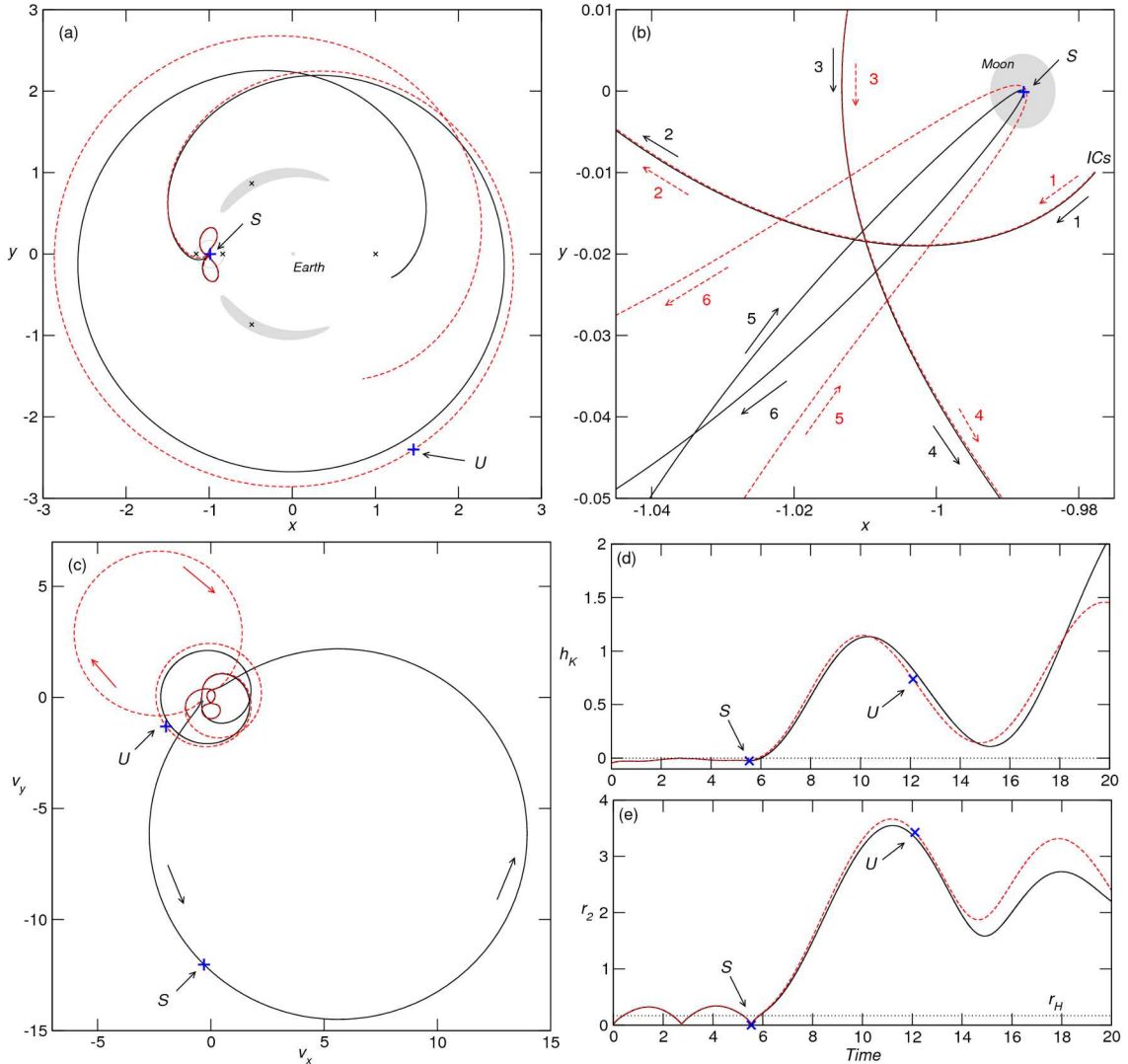


FIGURE 6.3 – (a) Projection onto the x - y plane of the stable (black solid curve) and the unstable (red dashed curve) trajectories of the S-E collisional transition at $r^* = 0.01425078$, $\theta = 1.753\pi$ rad for $\Delta r_2 = \Delta r_2^0 \times 10^{-1}$ in the set of initial conditions with negative initial velocity and $e = 0.9$, integrated during 20 dimensionless units of time. The forbidden region for C^s is shown in grey, the lunar SOI is delimited by the grey curve and the equilibrium points are shown as x. (b) Magnification of (a) in a region near the Moon (grey ball). ICs labels the initial conditions and the numbered arrows indicate the sense of the motion along the stable (black solid) and the unstable (red dashed) trajectories. (c) Projection onto the x - y plane of the stable (black solid curve) and the unstable (red dashed curve) trajectories. The arrows indicate the sense of the motion along the trajectories. (d) The Kepler energy of P_3 w.r.t P_2 as a function of the time in dimensionless units. (e) The distance from P_3 to P_2 as a function of the time in dimensionless units. In all frames, the blue x or + labeled as S (U) indicates the point at which the trajectory returns to $l(\theta)$ and is classified as stable (unstable).

asymptotic to $\Gamma_k(C^*)$ lies at the stability boundary. We call ΔT^s the interval of time after which the trajectory generated by p^s returns to $l(\theta)$ with $h_K < 0$. As Δr_2 diminishes, the successive initial conditions p^s generate trajectories that approach the orbit asymptotic to $\Gamma_k(C^*)$ and, as a result, ΔT^s increases.

In Figure 6.4 (a) we present the x - y projection of a S-G1 transition at $r_2^* = 0.00656586$, $\theta = 1.299\pi$ rad, determined by the proximity of the stable manifold of $\Gamma_1(C^*)$, $C^* \approx 3.17323193$, $|C^s - C^u| \approx 10^{-8}$, for the set of initial conditions with positive initial velocity, $e = 0.9$, and $\Delta r_2 = 2.60148651 \times 10^{-9}$. For the sake of visualization, the Poincaré cuts of the neighboring stable and unstable trajectories are shown in Figure 6.4 (b) for Δr_2^0 , such that $C^s = 3.17432874$ and $C^u = 3.17227383$. The Poincaré cuts of the stable manifolds $W_1^s(C^s)$ and $W_1^s(C^u)$ associated to $\Gamma_1(C^s)$ and $\Gamma_1(C^u)$, respectively, are also shown. For Δr_2^0 , we find that $\Delta T^s = 2.139$, while ΔT^s increases to 6.172 for $\Delta r_2 = 2.60148651 \times 10^{-9}$. This type of transition implies that the stable capture orbits approach the Lyapunov orbit around L_1 or L_2 , which means that P_3 is taken to the limits of the lunar SOI before completing a full turn around the Moon. The distance from the Moon along with the increase of ΔT^s are not ideal characteristics for ballistic capture states for practical purposes.

Usually, in the case of transitions associated to divergence due to the invariant manifolds of Γ_k , the unstable initial conditions belong, as expected, to \mathcal{G}^1 or \mathcal{G}^2 . However, we also find cases at which the unstable initial condition belongs to subset \mathcal{E} . This occurs when the trajectory returns to $l(\theta)$ at $t = t_f$ after passing through the neck region around L_k but before completing a full turn around the Earth. So, the trajectory is classified as unstable if

$$r_f((x_f + 1 - \mu + \dot{y}_f)^2 + (\dot{x}_f - y_f)^2) > 2\mu, \quad (6.1)$$

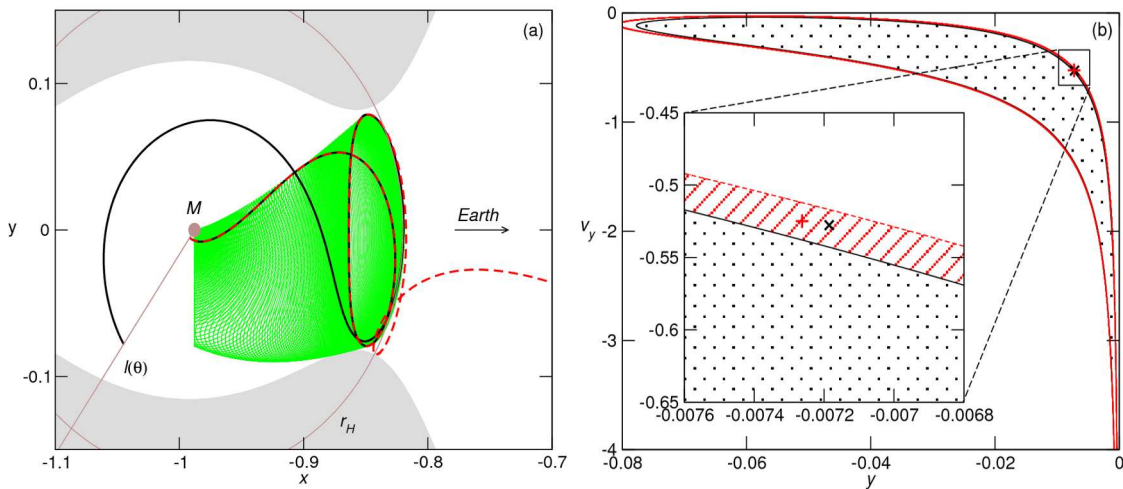


FIGURE 6.4 – (a) Projection onto the x - y plane of the stable (black solid curve) and the unstable (red dashed curve) trajectories of the S-G1 transition determined by the left branch of the stable manifold (green) of $\Gamma_1(C^*)$, $C^* \approx 3.17323193$, for $\Delta r_2 = 2.60148651 \times 10^{-9}$ at $r_2^* = 0.00656586$, $\theta = 1.299\pi$ rad, in the set of initial conditions with $e = 0.9$ and positive initial velocity. The forbidden region is shown in grey and the lunar SOI is delimited by the curve labeled with r_H . (b) Poincaré section $x = -1 + \mu, \dot{x} > 0$ of the stable manifolds of $\Gamma_1(C^s = 3.17432874)$ (black solid curve) and $\Gamma_1(C^u = 3.17227383)$ (red dashed curve). For the sake of visualization, the radial increment is Δr_2^0 . The Poincaré cut of the non-transit stable orbit (black x) located outside the cut of $W_1^s(C^s)$ (black dotted area) and the cut of the transit unstable orbit (red +) interior to the cut of $W_1^s(C^u)$ (red dashed area) are also shown.

where $r_f = [(x_f + 1 - \mu)^2 + y_f^2]^{1/2}$ and $(x_f, y_f, \dot{x}_f, \dot{y}_f)$ is the state of P_3 at t_f .

If Equation 6.1 is not satisfied, the trajectory is classified as stable. This produces a meaningless classification, in the sense that a capture behavior is assigned to a transit trajectory that wanders through the exterior or the Earth realms before returning to $l(\theta)$.

As a result, the association of the geometrical criterion (return to $l(\theta)$) with the measurement of the Kepler energy, may mask or even suppress the dynamical effects that cause the divergence of trajectories, rendering a questionable classification.

6.3 Transitions Due to Constructive Effects of the Algorithm

6.3.1 Geometrical Criteria

An example of a constructive effect of the algorithm determining a transition is the situation at which the return to $l(\theta)$ criterion implies that the classification of similar trajectories is performed at different characteristic times.

In Figure 6.5, we have a transition defined for $\Delta r_2^0 \times 10^{-1}$, at $r^* = 0.03890635$, $\theta = 0.931\pi$ rad in the set of initial conditions with positive initial velocity, and $e = 0.9$. In this case an initial condition generates a trajectory that returns to $l(\theta)$ with $h_K < 0$, so it is classified as stable. On the other hand, its first outer radial neighbor, generates a trajectory, that, although it does not differ considerably from the stable one, is almost tangent to the $l(\theta)$ line and continues up until it completes a full turn around the Earth, thus being classified as unstable due to primary interchange through L_2 . In this case, the classification procedure determines a transition of type S-G2, although the involved neighbor trajectories present very similar long-term behaviors.

Another such example is given in Figure 6.6, where, again, the orbit at the boundary is tangent to $l(\theta)$. Now, the first outer neighboring initial condition is classified as unstable

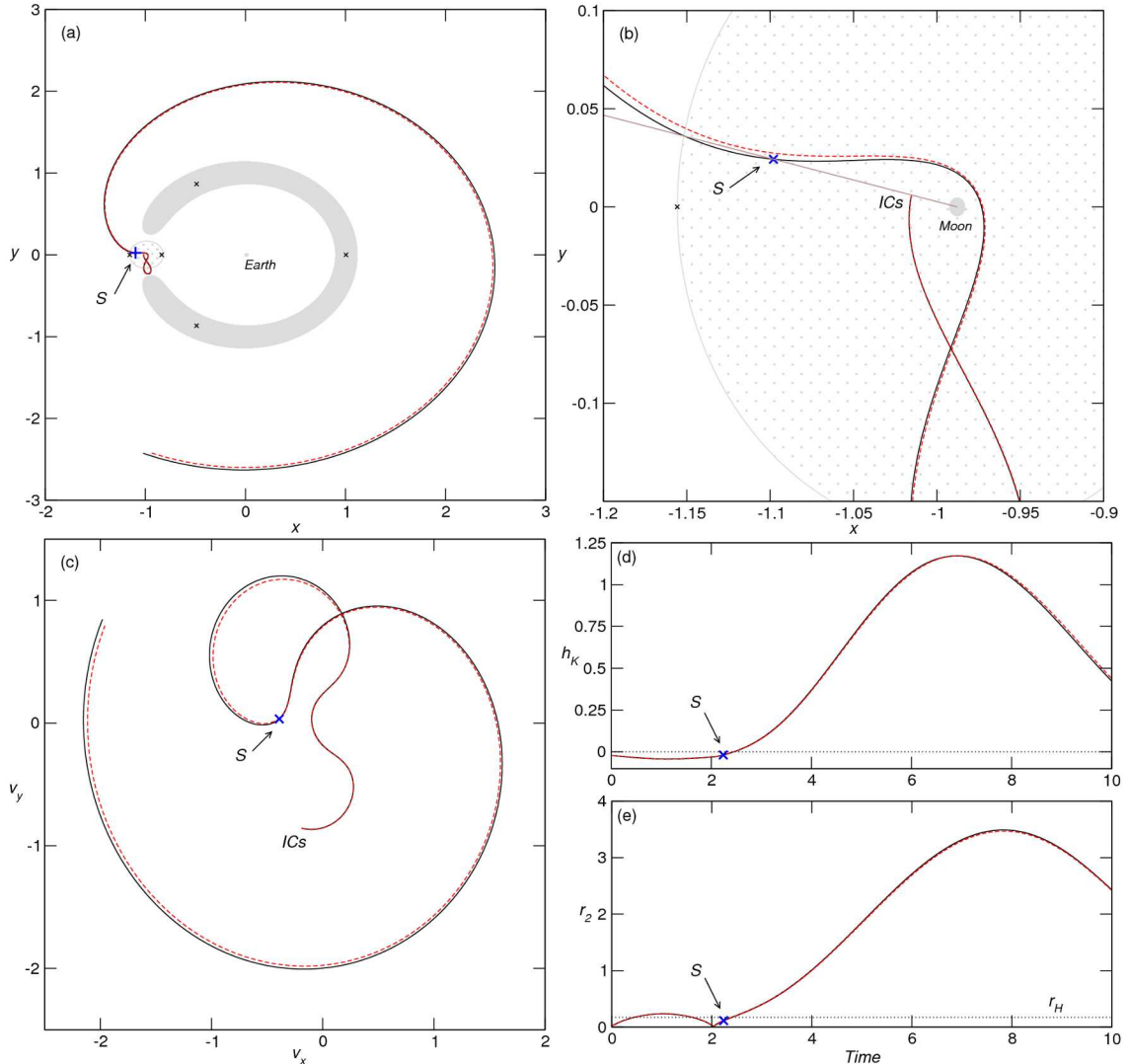


FIGURE 6.5 – (a) Projection onto the x - y plane of a radial S-G2 transition for $\Delta r_2^0 \times 10^{-1}$, at $r^* = 0.03890635$, $\theta = 0.931\pi$ rad, in the set with positive initial velocity with $e = 0.9$. The stable trajectory (black solid curve) returns to the $l(\theta)$ segment, while its unstable neighbor (red dashed curve) is only almost tangent to the line. The trajectories were integrated for 10 dimensionless time units, the forbidden region is shown in grey, and the equilibria are marked with x. (b) Magnification of (a) in a region near the Moon (grey ball). The $l(\theta)$ segment is indicated by the brown straight line, the grey dotted area depicts the lunar SOI, and the initial conditions are indicated by ICs. (c) Projection onto the v_x - v_y plane of the stable (black solid curve) and the unstable (red dashed curve) trajectories. (d) The Kepler energy of P_3 w.r.t P_2 as a function of the time in dimensionless units. (e) The distance from P_3 to P_2 as a function of the time in dimensionless units. In all frames, the blue x or + labeled as S indicates the point at which the trajectory returns to $l(\theta)$ and is classified as stable.

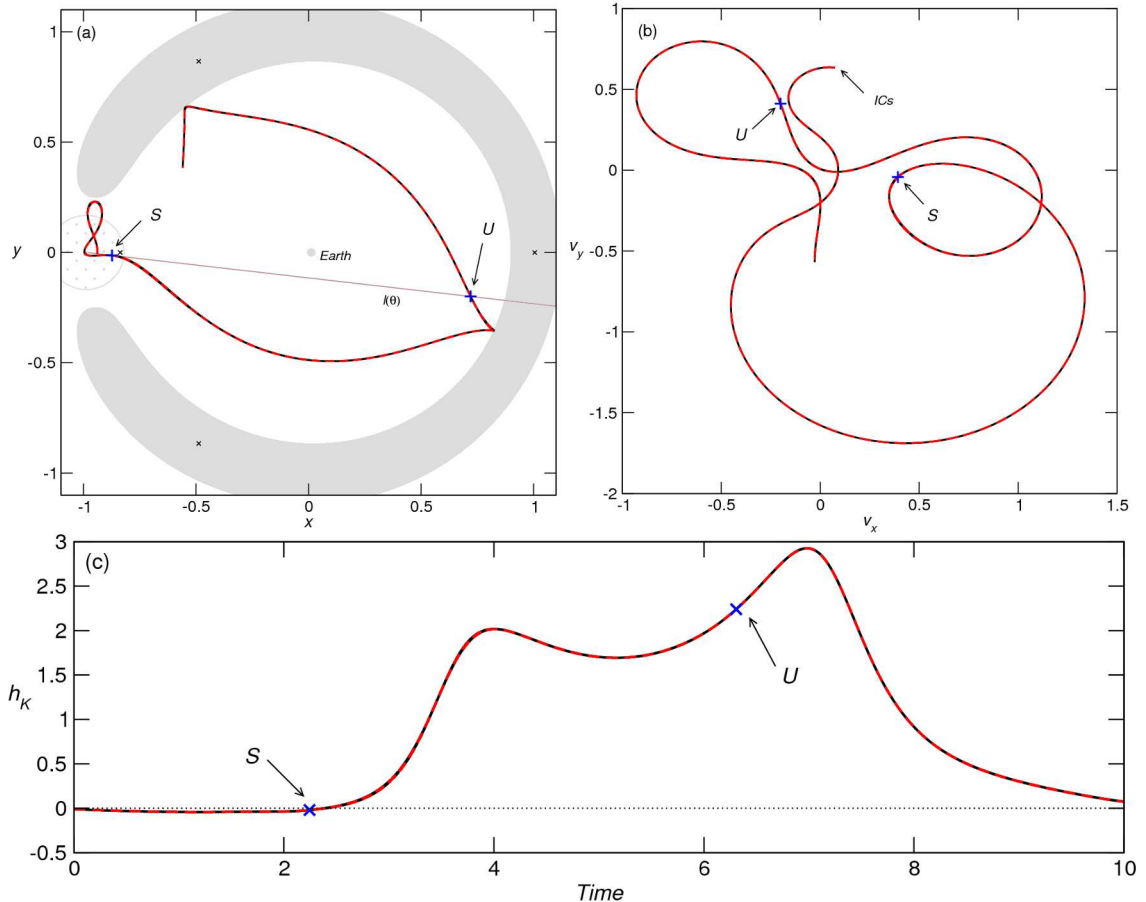


FIGURE 6.6 – (a) Projection onto the x - y plane of the S-E transition due to tangency at $r^* = 0.04879526$, $\theta = 1.963\pi$ rad, for $\Delta r_2^0 \times 10^{-3}$, in the set of initial conditions with positive initial velocity and $e = 0.9$. The stable (unstable) trajectory is shown as a black solid (red dashed) curve. (b) Projection onto the \dot{x} - y plane of the stable (black solid) and the unstable (red dashed) trajectories. (c) h_K of P_3 w.r.t P_2 as a function of the dimensionless time. The blue x or + labeled as S (U) indicates where the trajectory is classified as stable (unstable).

due to non-negative Kepler energy, so the transition is of type S-E. In this case, the return to $l(\theta)$ occurs outside the lunar SOI, so the measurement of h_K is questionable, given that the two-body approximation is not valid in this region.

This constructive artifact separates trajectories with indistinguishable dynamical behaviors. In order to confirm that the trajectories remain together in phase space for a long interval of time after the stable classification, we plot the \dot{x} - y projection of the trajectories at the S-E transition (Fig. 6.6 (b)). The indistinguishable time history of the Kepler energy is also shown (Fig. 6.6 (c)).

In these two examples, the stable solutions escape through the neck regions around L_1 or L_2 soon after they are classified. They share this transit behavior with their unstable neighbors. Although in these two examples, the stable classification is performed inside the lunar SOI, there are cases in which the trajectories may wander far beyond the lunar SOI before returning to $l(\theta)$. Thus, neglecting the spatial extension of the trajectories may imply in undesirable profiles for stable solutions as shown in Figures 5.27 and 5.28.

Moreover, in the case of primary interchange solutions, the requirement of a complete turn around the Earth can also affect the classification in a questionable way. If the trajectory eventually returns to $l(\theta)$ before fulfilling this criterion, and Equation (6.1) is not satisfied, the initial condition is erroneously classified as stable. Take, for example, the G2-S transition (T1) followed by a S-G2 transition (T2) for Δr_0 , with $\theta = 0.196\pi$ rad in the set of initial conditions with positive initial velocity and $e = 0.9$, shown in Figure 6.7. All the trajectories leave the Moon realm through the neck region around L_2 and visit the exterior realm before returning to the vicinity of the Moon. In transition T1, the unstable orbit completes 360° around the Earth just before returning to $l(\theta)$. On the other hand, its outer radial neighbor, although presenting a remarkably similar behavior, returns to $l(\theta)$ just before completing a full turn around the Earth and the measurement of h_K accounts for the misleading stable characterization of this orbit. The next transition, T2, is due to collision with the center of mass of P_2 , similar to the case illustrated by Figure 6.3.

In the transitions observed in Figure 6.7, the large distance from the trajectories to P_2 is neglected by the algorithm. On the other hand, the fulfillment of the complete turn around P_1 or P_2 , which is a determinant criterion of the algorithm, does not differentiate relevant distinct dynamical behaviors. Additionally, these geometrical criteria do not guarantee temporary capture states, as is evident in this example.

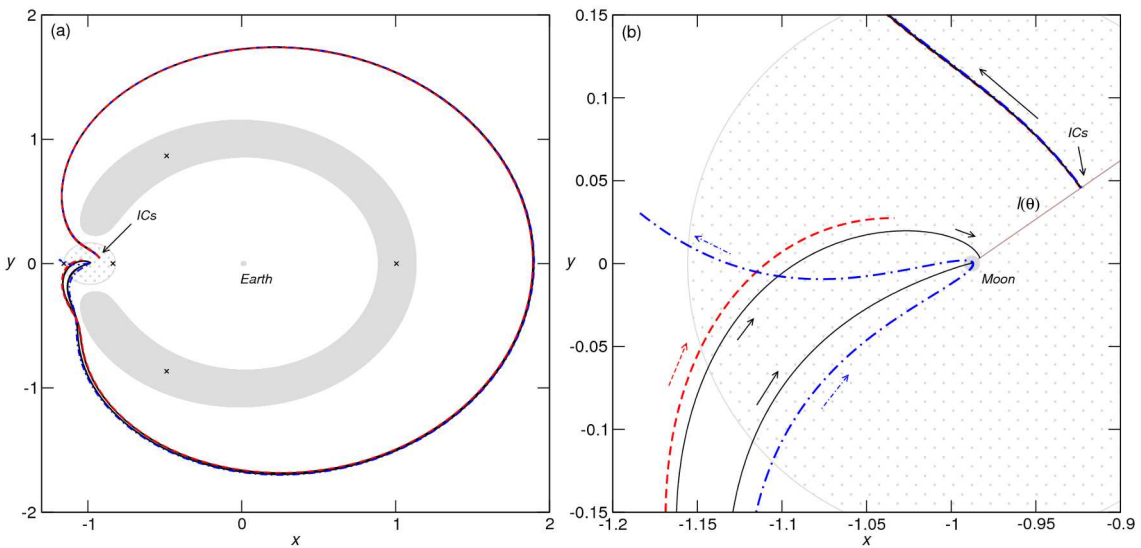


FIGURE 6.7 – **(a)** Projection onto the x - y plane of trajectories representing two subsequent transitions T1 and T2 for Δr_0 in the set of initial conditions with positive initial velocity with $e = 0.9$ and $\theta = 0.196\pi$. Transition T1 is of type G2-S, while transition T2 is of type S-G2. **(b)** Magnification of **(a)** in a region near the Moon (grey ball), the $l(\theta)$ segment is indicated by the brown straight line, and the initial conditions are indicated by ICs . In both frames, the stable trajectories are shown as black solid curves, while the unstable trajectory of transition T1 is shown as a red dashed curve and the unstable trajectory of transition T2 is shown as a blue dot-dashed curve. The grey dotted area depicts the lunar SOI. For each trajectory the time of integration corresponds to the time at which the classification is performed.

6.3.2 Measurements of the Kepler Energy

As already mentioned, the Kepler energy is not always consistent as a capture indicator for a solution of the PCR3BP. In Figure 6.8 we show a S-E transition at $r^* = 0.02962539$, $\theta = 0.64\pi$ rad, for $\Delta r_2^0 \times 10^{-3}$ in the set of initial conditions with negative initial velocity and $e = 0.9$. In this case, the measurement of h_K does not distinguish either dynamical behavior or capture state, i.e., the classification procedure erroneously separates indistinguishable dynamical behaviors and the trajectory said to be stable is not consistent with qualitative aspects of the full cycle orbits that may be required or appropriate for a ballistic capture orbit in practical applications.

These inconsistencies arise because h_K is measured outside the lunar SOI where the two-body approximation is not valid.

Moreover, there are situations for which even the measurement of h_K inside the lunar SOI does not guarantee that the trajectory behavior is consistent with a temporary capture state for practical applications. In this case, once again, the association of the geometrical criterion (return to $l(\theta)$ after a full turn around the Moon) with the energy threshold defined by $h_K = 0$ implies that similar dynamical behaviors are meaninglessly separated as stable and unstable. As an example, consider the S-E transition at $r^* = 0.02858194$, $\theta = 1.941\pi$ rad, for $\Delta r_2^0 \times 10^{-3}$ in the set of initial conditions with negative initial velocity and $e = 0.9$, shown in Figure 6.9.

Here, the inconsistency arises because the time history between the initial condition and the final state is neglected. The long flight time of the trajectories and the time history of the distance from P_3 to P_2 should be considered as indicators of anomalous trajectory profiles in terms of capture.

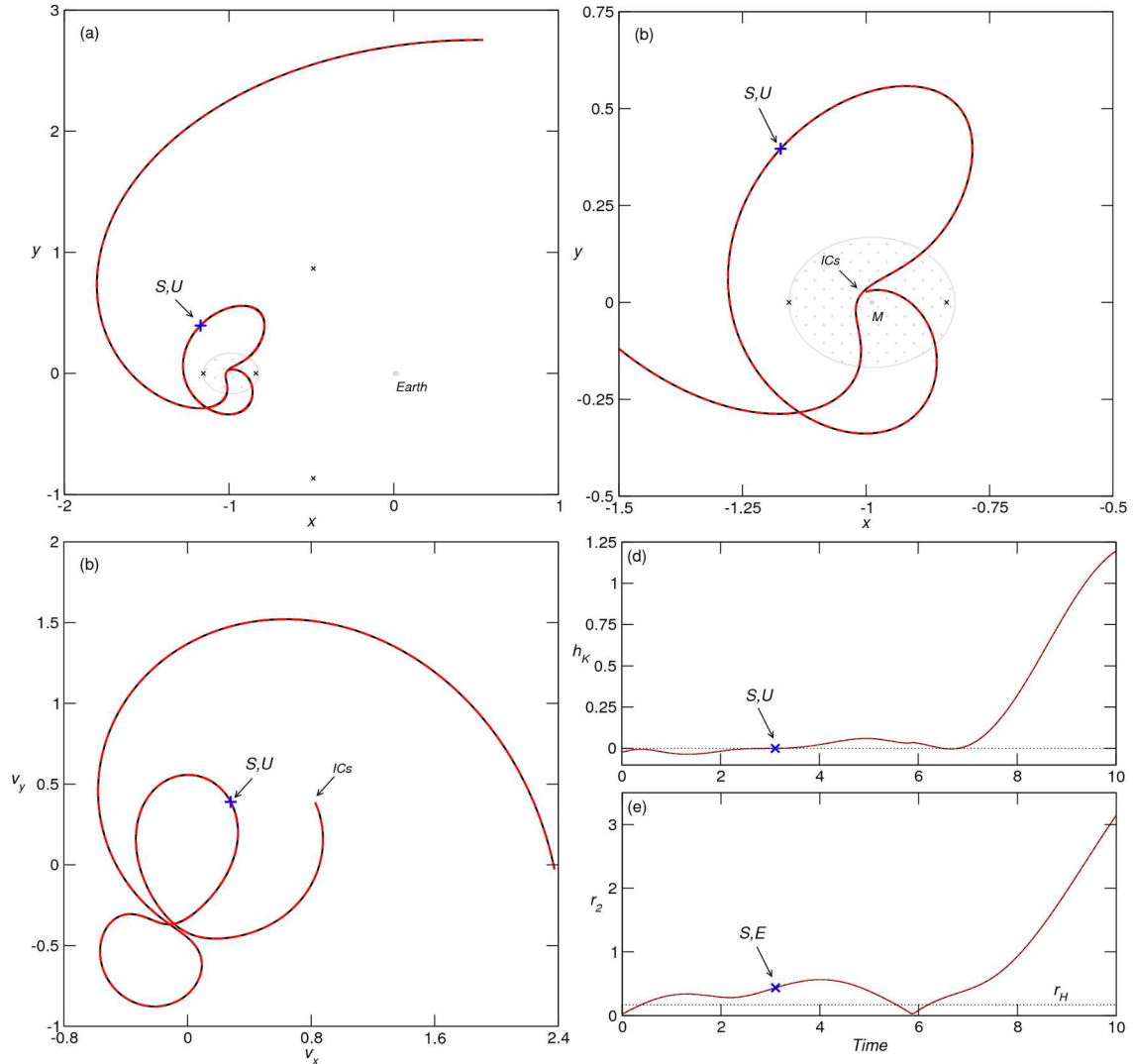


FIGURE 6.8 – (a) Projection onto the x - y plane of the S-E transition at $r^* = 0.02962539$, $\theta = 0.64\pi$ rad, for $\Delta r_2^0 \times 10^{-3}$ in the set of initial conditions with negative initial velocity and $e = 0.9$. The stable (unstable) trajectory is shown as a black solid (red dashed) curve. (b) Magnification of (a) in a region near the Moon (grey ball). The grey dotted area depicts the lunar SOI and the initial conditions are indicated by ICs . (c) Projection onto the x - v plane of the stable (black solid) and the unstable (red dashed) trajectories. (d) h_K of P_3 w.r.t P_2 as a function of the dimensionless time. (e) The distance from P_3 to P_2 as a function of the time in dimensionless units. In all frames, the blue x or + labeled as S (U) indicates the point at which the trajectory returns to $l(\theta)$ and is classified as stable (unstable).

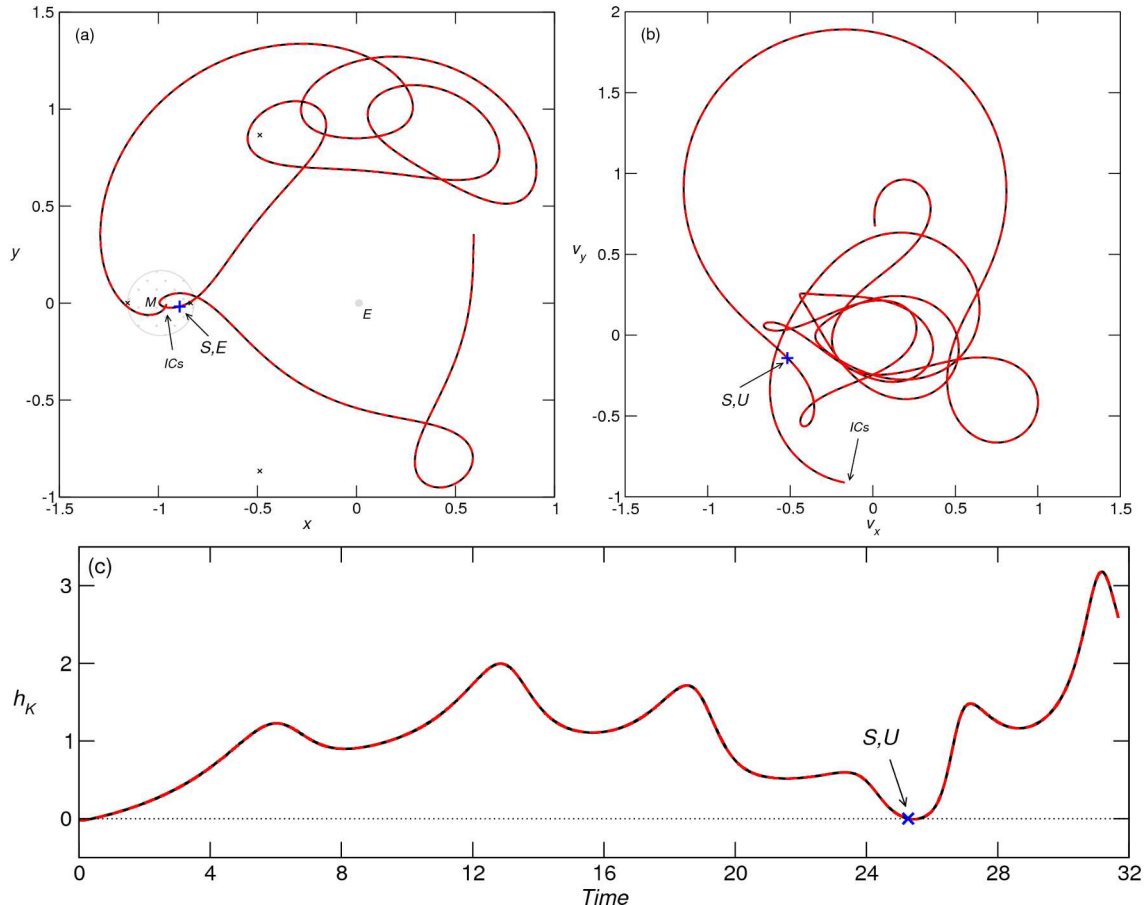


FIGURE 6.9 – (a) Projection onto the x - y plane of the S-E transition at $r^* = 0.02858194$, $\theta = 1.941\pi$ rad, for $\Delta r_2^0 \times 10^{-3}$ in the set of initial conditions with negative initial velocity and $e = 0.9$. The stable (unstable) trajectory is shown as a black solid (red dashed) curve. (b) Projection onto the \dot{x} - \dot{y} plane of the stable (black solid) and the unstable (red dashed) trajectories. (c) h_K of P_3 w.r.t P_2 as a function of the dimensionless time. The blue x or + labeled as S (U) indicates where the trajectory is classified as stable (unstable).

6.4 Discussion

The investigation presented in this Chapter constitutes a detailed characterization of the stable-unstable transitions produced by the WSB algorithmic definition. The observed features allow us to make some comments about the consistency of the construction procedure and the practical applicability of boundary solutions in low-energy transfers with temporary ballistic capture at arrival.

The existence of several types of transitions is an important characteristic of the algorithmic WSB. Also, the presence of collisional trajectories in the boundary set implies that the applicability of large portions of the WSB is restricted to the stabilization of trajectories at the initial conditions due to the occurrence of collision with the primary.

The implemented refinement procedure reveals the existence of smooth and fractal-like grid-dependent transitions. We find that the mechanisms determining the stable-unstable classification can be of dynamical or constructive nature. In the first case, the classification is an evidence of the nonlinear behavior of the trajectories. In the second case, the classification often does not result in boundary solutions that act as natural separatrices of the solutions of the system regarding the characterization of effective stable behavior. Thus, the boundary is not always compatible with the expected separatrix feature presented by the parabolic Keplerian solution that separates bounded and unbounded motion in the two-body problem.

The results suggest that the use of the return to $l(\theta)$ geometrical criterion along with the measurement of h_K is not always consistent over the full sets of initial conditions due to the highly nonlinear behavior of the trajectories. Moreover, the classification procedure does not exclusively extract ballistic capture solutions with adequate profiles for practical applications. Thus, the use of h_K as an adequate quantifier should be restricted

by the validity of the two-body approximation. Furthermore, some natural dynamical elements of the PCR3BP, such as the total flight time at the classification, the relative position at the instant of classification with respect to the lunar SOI, and the complete history of the trajectories, should be included in the procedure in order to determine effective stability boundaries and regions in phase space where temporary capture occurs for practical applications.

Given that the WSB algorithmic construction relays solely on the prograde ($t > 0$) classification of specific sets of initial conditions around the Moon generated as a function of the osculating ellipse eccentricity for positive and negative initial velocities, it does not guarantee transfer solutions. Thus, the inclusion of a retrograde ($t < 0$) analysis is necessary in order to determine effective capture orbits of the complete Earth-to-Moon trajectory. Also, different choices of the initial condition sets could be considered. A natural possibility is to generate initial conditions in an energy shell, keeping the Jacobi constant fixed instead of the eccentricity of the osculating ellipse.

The characterization of the types of transition along the boundary suggests that the constructive procedure should be revised in order to solely extract solutions that act as natural separatrices of the system solutions regarding the characterization of effective stable behavior.

7 Conclusion

In this thesis, we presented an extensive investigation of the WSB concept in low-energy Earth-to-Moon mission design.

Initially, by employing the *patched three-body approach* to approximate the Sun-Earth-Moon-spacecraft system, we examined and characterized the construction of Earth-to-Moon trajectories, identifying the relevant dynamical ingredients for feasible transfer orbits. Also, we found quasiperiodic orbits that provide fast connection between Earth parking orbits and the patching region where the invariant manifolds of the EM-system and of the SE-system intersect each other. Still, further investigation regarding the energy feasibility of such trajectories is needed.

Then, in order to study temporary capture processes by the Moon, we focused on the final portion of transfer trajectories. We performed a dynamical characterization of the associated sets generated by two implementations of the WSB algorithmic definition in the lunar sphere of influence. In the first implementation, we considered the Moon as a punctual mass, while in the second the finite mean radius of the Moon was taken into account, revealing the relation between the stability boundary and the lunar collisional set. The WSB associated sets were analysed according to relevant criteria established on three-body problem elements in order to clarify their possible applicability in external and internal transfers and to verify the consistency of the algorithmic construction procedure. Special attention was given to the stable set both regarding its applicability and the

characterization of the dynamical diversity of stable trajectories. We verified that the algorithmic classification procedure does not result in boundary sets that act as natural separatrices of the solutions of the system regarding the characterization of effective stable behavior. Also, it does not solely identifies ballistic capture solutions with adequate profiles for practical applications.

Finally, we extracted the boundary of stability, revealing the existence of several sub-cases of stable-unstable transitions. We investigated the fractal-like structure of the boundary set and characterized transitions associated to dynamical effects and transitions that appear due to constructive aspects of the algorithm.

Our analyses show that the current algorithmic definition of the WSB presents several vulnerable points and needs revision in order to include some natural dynamical elements of the PCR3BP, such as the total flight time at the classification, the relative position at the instant of classification with respect to the lunar SOI, and the complete history of the trajectories. Also, a retrograde ($t < 0$) analysis should be added in order to determine effective capture orbits of the complete Earth-to-Moon trajectory. In addition, different choices of the initial condition sets could be considered.

The first natural extension of our investigation consists of employing the characterization procedures developed to verify the consistency of the algorithmic WSB exclusively in an annular region around the Moon associated to low lunar orbits, that is, with altitudes of approximately 100 km. This verification is important because it is expected that in this region, the gravitational effects due to the Moon are more determining than the influence of the Earth.

Another perspective for future work is the investigation of adequate conditions to determine effective stable regions around the Moon which are related to low-energy tem-

porary capture in higher dimensional mathematical models, such as the spatial version of the CR3BP or four-body models. In particular, in the case of the spatial version of the CR3BP, the central manifold associated to each collinear Lagrangian point and its stable and unstable invariant manifolds constitute a richer invariant set than the corresponding dynamical structures of the planar version. Thus, the definition of such effective stable regions represents a significant mathematical and practical challenge.

Bibliography

- [1] BELBRUNO, E. Lunar capture orbits, a method of constructing earth moon trajectories and the lunar GAS mission. In: 19TH AIAA/DGLR/JSASS INTERNATIONAL ELECTRIC PROPULSION CONFERENCE. *Proceedings...* Colorado, 1987. p. AIAA 87-1054.
- [2] BELBRUNO, E.; MILLER, J. *A Ballistic Lunar Capture Trajectory for the Japanese Spacecraft Hiten*. Jet Propulsion Laboratory, Pasadena, 1990. Report No. 312/90.4-1731-EAB.
- [3] BELBRUNO, E.; MILLER, J. Sun-perturbed Earth-to-Moon transfers with ballistic capture. *Journal of Guidance, Control and Dynamics*, v. 16, p. 770–775, 1993.
- [4] KOON, W. et al. Shoot the Moon. In: AAS/AIAA SPACE FLIGHT MECHANICS MEETING. *Proceedings...* Florida, 2000. p. AAS 00-166.
- [5] KOON, W. et al. Low energy transfer to the Moon. *Celestial Mechanics and Dynamical Astronomy*, v. 81, p. 63–73, 2001.
- [6] CIRCI, C.; TEOFILATTO, P. On the dynamics of weak stability boundary lunar transfers. *Celestial Mechanics and Dynamical Astronomy*, v. 79, p. 41–72, 2001.
- [7] BELBRUNO, E. *Capture Dynamics and Chaotic Motions in Celestial Mechanics*. Princeton: Princeton University Press, 2004.

- [8] GARCÍA, F.; GÓMEZ, G. A note on weak stability boundary. *Celestial Mechanics and Dynamical Astronomy*, v. 97, p. 87–100, 2007.
- [9] BELBRUNO, E.; TOPPUTO, F.; GIDEA, M. Resonance transitions associated to weak capture in the restricted three-body problem. *Advances in Space Research*, v. 42, p. 1330–1351, 2008.
- [10] TOPPUTO, F.; BELBRUNO, E. Computation of weak stability boundaries: Sun-Jupiter system. *Celestial Mechanics and Dynamical Astronomy*, v. 105, p. 3–17, 2009.
- [11] ROMAGNOLI, D.; CIRCI, C. Earth-moon weak stability boundaries in the restricted three and four body problem. *Celestial Mechanics and Dynamical Astronomy*, v. 103, p. 79–103, 2009.
- [12] SZEBEHELY, V. *Theory of Orbits*. 1st. ed. New York: Academic Press, 1967.
- [13] KOON, W. et al. *Dynamical Systems, The Three-Body Problem, And Space Mission Design*. New York: Springer-Verlag, 2006.
- [14] PRUSSING, J.; CONWAY, B. *Orbital Mechanics*. 1st. ed. New York: Oxford University Press, 1993.
- [15] PARKER, T.; CHUA, L. *Practical Numerical Algorithms for Chaotic Systems*. New York: Springer-Verlag, 1989.
- [16] JAMES, J. M. *Celestial Mechanics: Notes and Work*. 2007. Available at: <http://www.math.utexas.edu/users/jjames/celestMech>. Last access: January, 2011.
- [17] MIELE, A. Theorem of image trajectories in the earth-moon space. *Acta Astronautica*, v. 6, p. 225–232, 1960.

- [18] MOSER, J. On the generalisation of a theorem of A. Liapunoff. *Communications on Pure and Applied Mathematics*, v. 11, p. 257–271, 1958.
- [19] CONLEY, C. Low energy transit orbits in the restricted three-body problem. *SIAM Journal of Applied Mathematics*, v. 16, p. 732–746, 1968.
- [20] CONLEY, C. On the ultimate behavior of orbits with respect to an unstable critical point. *Journal of Differential Equations*, p. 136–158, 1969.
- [21] SIEGEL, C.; MOSER, J. *Lectures on Celestial Mechanics*. 1st. ed. New York: Springer-Verlag, 1971.
- [22] BATE, R.; MUELLER, D.; WHITE, J. *Fundamentals of Astrodynamics*. 1st. ed. New York: Dover Publications, 1971.
- [23] MARSDEN, J.; ROSS, S. New methods in celestial mechanics and mission design. *Bulletin (New Series) of the American Mathematical Society*, v. 43, p. 43–73, 2005.
- [24] BROWN, C. *Spacecraft Mission Design*. 2nd. ed. Reston, VA: AIAA, 1998.
- [25] SILVA, P. S.; TERRA, M. Dynamical properties of the weak stability boundary and associated sets. *Journal of Physics: Conference Series*, v. 246, p. 012007, 2010.
- [26] ROY, A. *Orbital Motion*. 4th. ed. Bristol: Institute of Physics Publishing, 2005.
- [27] MARINHO, C. *Dinâmicas de Captura e Escape nos Problemas de Três e Quatro Corpos*. Tese (Doutorado em Ciências) - Instituto Tecnológico de Aeronáutica, São José dos Campos. 2009.
- [28] YAGASAKI, K. Computation of low energy earth-to-moon transfers with moderate flight time. *Physica D*, v. 197, p. 313–331, 2004.

- [29] YAGASAKI, K. Sun-perturbed earth-to-moon transfers with low energy and moderate flight time. *Celestial Mechanics and Dynamical Astronomy*, v. 90, p. 197–212, 2004.
- [30] MIELE, A.; MANCUSO, S. Optimal trajectories for earth-moon-earth flight. *Acta Astronautica*, v. 49, p. 59–71, 2001.
- [31] PERGOLA, P. et al. Earth-Mars halo to halo low thrust manifold transfers. *Celestial Mechanics and Dynamical Astronomy*, v. 105, p. 19–32, 2009.
- [32] SILVA, P. S.; TERRA, M. Analysis of the weak stability boundary, associated sets and algorithmic construction in the lunar SOI. *Celestial Mechanics and Dynamical Astronomy*. Submitted.
- [33] YAZDI, K.; MESSERSCHMID, E. Analysis of parking orbits and transfer trajectories for mission design of cis-lunar space station. *Acta Astronautica*, v. 55, p. 759–771, 2004.
- [34] MCGEHEE, R. *Some homoclinic orbits for the restricted three-body problem*. Thesis (Ph.D. in Philosophy) - University of Wisconsin, Madison. 1969.
- [35] SILVA, P. S.; TERRA, M. Stable-unstable transitions of the algorithmic weak stability boundary. *Chaos*. Submitted.
- [36] BATTIN, R. *An Introduction to the Mathematics and Methods of Astrodynamics*. Reston, VA: AIAA, 1987.
- [37] BROUCKE, R. Regularization of the plane restricted three-body problem. *Icarus*, v. 4, p. 8–18, 1965.
- [38] PRADO, A. *Trajetórias Espaciais e Manobras Assistidas por Gravidade*. São José dos Campos, SP: INPE, 2001.

Appendix A - Constants

Gravitacional constant	G	6.668×10^{-11}	Nm^2kg^{-2}
Sun-Earth mean distance	r_{01}	1.495978×10^8	km
Earth-Moon mean distance	r_{12}	3.844×10^5	km
Sun-Earth angular velocity	ω_E	1.99095×10^{-7}	rad/s
Earth-Moon angular velocity	ω_M	2.66170×10^{-6}	rad/s
Sun radius	r_S	6.9599×10^5	km
Sun mass	m_0	1.989×10^{30}	kg
Earth equatorial radius	r_E	6.37812×10^3	km
Earth mass	m_1	5.974×10^{24}	kg
Moon mean radius	r_M	1.738×10^3	km
Moon mass	m_2	7.3485×10^{22}	kg

Earth-Moon system ($\mu_{\oplus} = 0.0121506683$)

	x	y	C
Earth, P_1	0.0121506683	0.0	-
Moon, P_2	-0.9878493317	0.0	-
L_1	-0.8369147188	0, 0	3.2003449098321
L_2	-1.1556824834	0, 0	3.1841641431764
L_3	1.0050626802	0, 0	3.0241502628815
L_4	-0.4878493317	0.8660254037	3.0
L_5	-0.4878493317	-0.8660254037	3.0

*In the Earth-Moon normalized synodic reference frame.

Sun-Earth system ($\mu_{\odot} = 3.03591 \times 10^{-6}$)

	X	Y	C
Sun, P_0	3.03591×10^{-6}	0.0	-
Earth, P_1	-0.9999969640	0.0	-
L_1	-0.9899909371	0.0	3.0009000935260
L_2	-1.0100701875	0.0	3.0008960456047
L_3	1.0000012649	0.0	3.0000060718105
L_4	-0.4999969641	0.866025403784439	3.0
L_5	-0.4999969641	-0.866025403784439	3.0

*In the Sun-Earth normalized synodic reference frame.

Appendix B - The Sphere of Influence

For practical purposes, it is convenient to define a region around a celestial body P in which the gravitational interaction of that primary with a spacecraft V can be approximated by a two-body problem, considering the gravitational effects of other massive bodies as perturbations. This region is called the Sphere of Influence (SOI) [14, 26, 36].

In order to define the SOI and determine its radius, we consider the method developed by Laplace in the 18th century. First we write the equations of motion for P and V , including the gravitational effects of all n bodies of the complete $(n + 2)$ -body system.

$$\ddot{\mathbf{R}}_P = \frac{Gm_V}{r_{PV}^3} \mathbf{r}_{PV} + G \sum_{j=1}^n \frac{m_j}{r_{Pj}^3} \mathbf{r}_{Pj}, \quad (1)$$

$$\ddot{\mathbf{R}}_V = \frac{Gm_P}{r_{VP}^3} \mathbf{r}_{VP} + G \sum_{j=1}^n \frac{m_j}{r_{Vj}^3} \mathbf{r}_{Vj}, \quad (2)$$

where G is the gravitational constant, and m_P and m_V are the masses of P and V , respectively.

Using $\mathbf{r} = \mathbf{r}_{PV} = -\mathbf{r}_{VP}$ and subtracting Equation (2) from Equation (1), we obtain the relative equation of motion of the two-body problem $P-V$

$$\ddot{\mathbf{r}} + \frac{G(m_P + m_V)}{r^3} \mathbf{r} = -G \sum_{j=1}^n m_j \left(\frac{\mathbf{q}_j}{q_j^3} + \frac{\mathbf{d}_j}{d_j^3} \right), \quad (3)$$

where $\mathbf{q}_j = -\mathbf{r}_{Vj}$ and $\mathbf{d}_j = -\mathbf{r}_{Pj}$ according to Figure B.1.

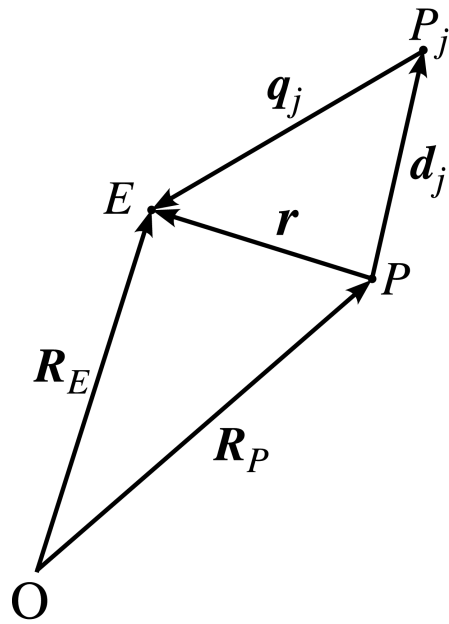


FIGURE B.1 – Disturbed motion.

The right-hand side of Equation (3) is the disturbing function accounting for the *third body effects*, i.e., the gravitational effects of the n bodies on the dynamics of the P - V system.

It is possible to determine which central body dominates over the dynamics of V . This is done by rewriting the equations of motion for each P - V two-body subsystem of the full $(n + 2)$ -body system, and comparing the ratio between the perturbing acceleration due to a third body and the gravitational attraction of each central body P .

As an example, consider the case of the Earth-Moon-Spacecraft system (P_1 - P_2 - P_3) with masses m_1 , m_2 , and m_3 , respectively, where $m_2 \ll m_1$ and m_3 is negligible compared with m_1 and m_2 . Rewriting Equation (3) for the P_1 - P_3 subsystem, we have

$$\ddot{\mathbf{r}}_{13} + \frac{G(m_1 + m_3)}{r_{13}^3} \mathbf{r}_{13} = -Gm_2 \left(\frac{\mathbf{r}_{23}}{r_{23}^3} + \frac{\mathbf{r}_{12}}{r_{12}^3} \right), \quad (4)$$

or,

$$\ddot{\mathbf{r}}_{13} - \mathbf{A}_1 = \mathbf{P}_2, \quad (5)$$

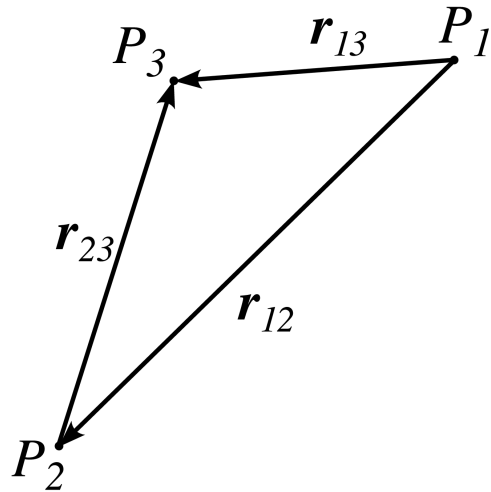


FIGURE B.2 – Relative position vectors of \$P_1\$, \$P_2\$, and \$P_3\$.

where \mathbf{A}_1 is the gravitational acceleration due to \$P_1\$ and \mathbf{P}_2 is the perturbing effect due to \$P_2\$. The relative position vectors of \$P_i\$, \$i = 1, 2, 3\$, are shown in Figure B.2.

Analogously, for the \$P_2\$-\$P_3\$ subsystem, we obtain

$$\ddot{\mathbf{r}}_{23} + \frac{G(m_2 + m_3)}{r_{23}^3} \mathbf{r}_{23} = -Gm_1 \left(\frac{\mathbf{r}_{13}}{r_{13}^3} + \frac{\mathbf{r}_{12}}{r_{12}^3} \right), \quad (6)$$

or, rewriting for the gravitational acceleration due to \$P_2\$, \mathbf{A}_2 , and for the perturbing effect \mathbf{P}_1 ,

$$\ddot{\mathbf{r}}_{23} - \mathbf{A}_2 = \mathbf{P}_1. \quad (7)$$

As seen in Equations (6) and (7), when \$P_3\$ is very close to \$P_2\$, \$|\mathbf{P}_1|\$ is equal to the difference between two nearly equal vectors, thus, even though \$m_1 \ll m_2 + m_3\$, the perturbing effect due to \$P_1\$ is very small compared with \$|\mathbf{A}_2|\$.

The ratio \$|\mathbf{P}_2|/|\mathbf{A}_1|\$ quantifies the perturbation due to the Moon on the geocentric orbit of the spacecraft in the \$P_1\$-\$P_3\$ subsystem, while \$|\mathbf{P}_1|/|\mathbf{A}_2|\$ quantifies the perturbation due to the Earth on the selenocentric orbit of the spacecraft in the \$P_2\$-\$P_3\$ subsystem. The

	SOI radius (km)	SOI radius (body radius)
Earth	9.24×10^5	145
Moon	6.619×10^4	38

TABLE B.1 – Radii of the sphere of influences of the Earth (SOI_1) and of the Moon (SOI_2).

sphere of influence is defined as the surface along which the magnitudes of the accelerations satisfy

$$\frac{|\mathbf{P}_2|}{|\mathbf{A}_1|} = \frac{|\mathbf{P}_1|}{|\mathbf{A}_2|}. \quad (8)$$

Inside the SOI of P_2 , the left side of Equation (8) is greater than the right side, while the opposite is true outside the SOI.

Given that $r_{23} \ll r_{13}$ and $r_{23} \ll r_{12}$ inside the SOI of P_2 , the surface defined by Equation (8) is approximately spherical [36] and its radius around P_2 is given by

$$r_{S2} = \left(\frac{m_2}{m_1} \right)^{2/5} r_{12}. \quad (9)$$

The same procedure can be applied to the Sun-Earth-Spacecraft system ($P_0-P_1-P_3$), with masses m_0 , m_1 , and m_3 , respectively, obtaining

$$r_{S1} = \left(\frac{m_1}{m_0} \right)^{2/5} r_{01}. \quad (10)$$

We will refer to the sphere of influences of the Earth and the Moon as SOI_1 and SOI_2 , respectively. Table B.1 displays the values of the radii of SOI_1 and SOI_2 , r_{S1} and r_{S2} . The physical constants m_0 , m_1 , m_3 , r_{01} , and r_{12} , used in the calculations are given in Appendix A.

In the context of preliminary space mission projects, the approximation of the motion

of the spacecraft by a succession of conic solutions, i.e., *the patched conic method*, consists in assuming that V escapes from the gravitational influence of P when it leaves the sphere of influence of that primary.

A more refined criterion leads to the definition of two spheres of influence for each primary [26]. Considering the P_1 - P_2 - P_3 system, for example, if the perturbation of P_2 on the motion of P_3 is neglected when it is less than a fraction ϵ_2 of $|\mathbf{A}_1|$,

$$|\mathbf{P}_2| = \epsilon_2 |\mathbf{A}_1|, \quad (11)$$

we can define an exterior sphere of influence SOI_2^e around the Moon, with radius $r_{S2}^e > r_{S2}$.

On the other hand, considering

$$|\mathbf{P}_1| = \epsilon_1 |\mathbf{A}_2|, \quad (12)$$

we obtain an interior sphere of influence SOI_2^i around the Moon, with radius $r_{S2}^i < r_{S2}$, where the perturbation due to P_1 is ϵ_1 times smaller than $|\mathbf{A}_2|$. Setting $\epsilon_1 = \epsilon_2 = \epsilon = 0.1$, we have $r_{S2}^i \approx 3.8 \times 10^4$ km and $r_{S2}^e \approx 1.154 \times 10^5$ km, or, approximately, $22r_M$ and $66r_M$, respectively.

Also, considering the P_0 - P_1 - P_3 system, we obtain an exterior sphere of influence SOI_1^e around the Earth, with radius $r_{S1}^e > r_{S1}$ and an interior sphere of influence SOI_1^i around the Earth, with radius $r_{S1}^i < r_{S1}$. Setting $\epsilon = 0.01$, we have $r_{S1}^i \approx 4 \times 10^4$ km and $r_{S1}^e \approx 2.66 \times 10^6$ km, or, approximately, $6r_E$ and $417r_E$, respectively.

Appendix C - Regularization Theory

The force acting on P_3 , as well as the particle's velocity, increases as P_3 approaches the vicinity of one of the primaries, going to infinity as the distance between these two bodies goes to zero. Thus, the equations of motion of the PCR3BP (Equation (2.20)) present singularities when $r_1 \rightarrow 0$ or $r_2 \rightarrow 0$, that is, when P_3 collides with P_1 or P_2 . These binary collisions are non-essential singularities that can be eliminated through regularization.

Following the terminology introduced by Birkhoff in 1915, two types of regularization methods can be introduced for the PCR3BP. The first type is called *local regularization* and refers to the introduction of transformations that regularize the equations of motion only at one of the two singularities. The second type is called *global regularization* and eliminates both singularities simultaneously.

In this work we employed the global regularization technique introduced by Lemaître in 1955. The regularized equations of motion were used when the system needed to be integrated in a region with radius equal to 10^{-2} dimensionless units around any primary.

Let $q = (x - \mu + \frac{1}{2}) + iy$ denote the position of P_3 in the rotating frame with origin at the midpoint between P_1 and P_2 , and let $w = u + iv$ denote the position of P_3 in the regularized reference frame. The regularization of the equations of motions is obtained through the introduction of the coordinate transformation given by

$$q = f(w) = \frac{1}{4} \left(w^2 + \frac{1}{w^2} \right), \quad (13)$$

and the time transformation given by

$$|f'(w)|^2 = \frac{|w^4 - 1|^2}{4|w|^6} = \frac{dt}{d\tau}, \quad (14)$$

where τ corresponds to the new independent variable and $f' = \frac{df}{dw}$.

The second order equation of motion can be written as

$$\frac{d^2w}{d\tau^2} + 2i|f'(w)|^2 \frac{dw}{d\tau} = \nabla_w \Omega^*, \quad (15)$$

where,

$$\nabla_w \Omega^* = \frac{\partial \Omega^*}{\partial u} + i \frac{\partial \Omega^*}{\partial v}, \quad (16)$$

with

$$\Omega^* = \left(\Omega - \frac{C}{2} \right) |f'(w)|^2, \quad (17)$$

where Ω is given by Equation (2.24) and C is the Jacobi constant.

Introducing $\bar{u} = \frac{du}{d\tau}$ and $\bar{v} = \frac{dv}{d\tau}$, we can rewrite Equation (15) as a system of four first order differential equations:

$$\frac{du}{d\tau} = \bar{u}, \quad \frac{d\bar{u}}{d\tau} - 2\bar{v}|f'(w)|^2 = \frac{\partial \Omega^*}{\partial u}, \quad (18)$$

$$\frac{dv}{d\tau} = \bar{v}, \quad \frac{d\bar{v}}{d\tau} + 2\bar{u}|f'(w)|^2 = \frac{\partial \Omega^*}{\partial v}.$$

For a detailed description of several regularization techniques, we refer the reader to Refs. [12] and [37] and a numerical implementation of Lemaître's method is found in Ref. [38].

Appendix D - Lyapunov-Moser Theorem

Let $H(x, y)$ be an analytic real function in a neighborhood of the origin, and let

$$\begin{aligned}\dot{x}_k &= H_{y_k}(x, y), & k = 1, \dots, n, \\ y_k &= -H_{x_k}(x, y),\end{aligned}\tag{19}$$

be the Hamiltonian system with n degrees of freedom, with an equilibrium solution $(x_k = 0, y_k = 0)$ at the origin. Let $\alpha_1, \dots, \alpha_n, -\alpha_1, \dots, -\alpha_n$ be the eigenvalues of the associate Jacobian matrix.

We state the following result due to J. Moser [18].

Theorem 1 (Lyapunov-Moser). *If the eigenvalues $\alpha_1, \dots, \alpha_n, -\alpha_1, \dots, -\alpha_n$ are $2n$ different complex numbers, α_1, α_2 independent over the reals and $\alpha_k \neq n_1\alpha_1 + n_2\alpha_2$, for all integers n_1, n_2 and $k \geq 3$, then, there exists a four parameter family of solutions of Equation (19) of the form*

$$\begin{aligned}x_k &= \phi_k(\xi, \eta, \gamma, \bar{\gamma}), \\ y_k &= \psi_k(\xi, \eta, \gamma, \bar{\gamma}),\end{aligned}\tag{20}$$

with

$$\begin{aligned}\xi &= \xi^\circ \exp[ta_1(\nu_1^\circ, \nu_2^\circ)], & \eta &= \eta^\circ \exp[ta_2(\nu_1^\circ, \nu_2^\circ)], \\ \gamma &= \gamma^\circ \exp[-ta_1(\nu_1^\circ, \nu_2^\circ)], & \bar{\gamma} &= \bar{\gamma}^\circ \exp[-ta_2(\nu_1^\circ, \nu_2^\circ)],\end{aligned}\tag{21}$$

where $a_1(\nu_1^\circ, \nu_2^\circ) = \alpha_1 + \dots$, and $a_2(\nu_1^\circ, \nu_2^\circ) = \alpha_2 + \dots$, are convergent power series in ν_1°, ν_2° , with $\nu_1^\circ = \xi^\circ \gamma^\circ$ and $\nu_2^\circ = \eta^\circ \bar{\gamma}^\circ$. The series ϕ_k, ψ_k converge in a neighborhood of the

origin and the rank of the matrices

$$\begin{bmatrix} \phi_{k\xi} & \phi_{k\gamma} \\ \psi_{k\xi} & \psi_{k\gamma} \end{bmatrix} e \begin{bmatrix} \phi_{k\eta} & \phi_{k\bar{\gamma}} \\ \psi_{k\eta} & \psi_{k\bar{\gamma}} \end{bmatrix} \quad (22)$$

is four. The solutions (Equation (21)) of the system depend on the four complex parameters ξ° , η° , γ° , and $\bar{\gamma}^\circ$. If in addition α_1 , α_2 , $-\alpha_1$, $-\alpha_2$ contain their complex conjugates, the solutions can be chosen to be real, depending on four real parameters.

This theorem is a generalization of a classical theorem by Lyapunov for Hamiltonian systems. J. Moser proves this result and studies the conditions under which the convergence of the series can be guaranteed [18]. Conley verified that, under the required conditions, Theorem 1 guarantees the existence of a family of unstable periodic orbits around each collinear equilibrium point of the PCR3PB and ensures that the qualitative results of the linearized system are valid for the full nonlinear system [19, 20].

When $n = 2$, as it is the case of the PCR3BP, this result describes all solutions of the system.

FOLHA DE REGISTRO DO DOCUMENTO			
1. CLASSIFICAÇÃO/TIPO TD	2. DATA 14 de fevereiro de 2011	3. REGISTRO N° DCTA/ITA/TD-001/2011	4. N° DE PÁGINAS 183
5. TÍTULO E SUBTÍTULO: The Algorithmic Weak Stability Boundary in Earth-to-Moon Mission Design: Dynamical Aspects and Applicability			
6. AUTOR(ES): Priscilla Andressa de Sousa Silva			
7. INSTITUIÇÃO(ÓES)/ÓRGÃO(S) INTERNO(S)/DIVISÃO(ÓES): Instituto Tecnológico de Aeronáutica – ITA			
8. PALAVRAS-CHAVE SUGERIDAS PELO AUTOR: Astronáutica; Fronteiras de Estabilidade Fraca; Sistemas Hamiltonianos			
9. PALAVRAS-CHAVE RESULTANTES DE INDEXAÇÃO: Mecânica celeste; Órbitas de transferência; Funções hamiltonianas; Problema de três corpos; Sistemas Terra-Lua; Missões espaciais; Astronomia; Astronáutica			
10. APRESENTAÇÃO: ITA, São José dos Campos. Curso de Doutorado. Programa de Pós-Graduação em Engenharia Aeronáutica e Mecânica. Área de Sistemas Aeroespaciais e Mecatrônica. Orientador: Maisa de Oliveira Terra. Defesa em 10/02/2011. Publicada em 2011.		X Nacional	Internacional
11. RESUMO: <p>This thesis consists of an extensive study of the Weak Stability Boundary (WSB) concept in low-energy Earth-to-Moon mission design within the mathematical structure provided by the Planar Circular Restricted Three-Body Problem (PCR3BP). By employing the patched three-body approach to approximate the Sun-Earth-Moon-spacecraft system, we examine and characterize the construction of Earth-to-Moon transfer orbits. Then, we focus on the final portion of the transfer trajectories, investigating the WSB algorithmic definition proposed by E. Belbruno. We perform a dynamical characterization of the WSB associated sets generated in the lunar sphere of influence by two implementations of this algorithmic definition, namely, considering the Moon as a punctual mass and as a body with finite radius. In addition, the associated sets are analysed according to relevant criteria established on three-body problem elements in order to clarify their possible applicability in external and internal transfers and to verify the consistency of the algorithmic construction procedure. Finally, we extract the boundary of stability and investigate the structure of the boundary set by characterizing specific stable-unstable transitions. This study identifies various vulnerable aspects of the algorithmic definition concerning the adequate detection of stability regions for ballistic lunar capture, and indicates required corrections to the algorithmic construction.</p>			
12. GRAU DE SIGILO: <input checked="" type="checkbox"/> OSTENSIVO <input type="checkbox"/> RESERVADO <input type="checkbox"/> CONFIDENCIAL <input type="checkbox"/> SECRETO			